OLIGONUCLEOTIDE GUANOSINE CONJUGATED TO GALLIUM NITRIDE NANO-STRUCTURES FOR PHOTONICS

Jianyou Li

Dissertation Prepared for the Degree of

DOCTOR OF PHILOSOPHY

UNIVERSITY OF NORTH TEXAS

August 2008

APPROVED:

Arup Neogi, Major Professor
Chris Littler, Committee Member and Chair of Department of Physics
Zhibing Hu, Committee Member
Arkadii Krokhin, Committee Member
William D. Deering, Program Coordinator
Sandra L. Terrell, Dean of the Robert B. Toulouse School of Graduate Studies

Li, Jianyou, Oligonucleotide guanosine conjugated to gallium nitride nano-structures for photonics. Doctor of Philosophy (Physics), August 2008, 107 pp., 3 tables, 40 illustrations, references, 122 titles.

In this work, I studied the hybrid system based on self-assembled guanosine crystal (SAGC) conjugated to wide-bandgap semiconductor gallium nitride (GaN). Guanosine is one of the four bases of DNA and has the lowest oxidation energy, which favors carrier transport. It also has large dipole moment. Guanosine molecules self-assemble to ribbon-like structure in confined space. GaN surface can have positive or negative polarity depending on whether the surface is Ga- or N-terminated. I studied SAGC in confined space between two electrodes. The current-voltage characteristics can be explained very well with the theory of metal-semiconductor-metal (MSM) structure. I-V curves also show strong rectification effect, which can be explained by the intrinsic polarization along the axis of ribbon-like structure of SAGC. GaN substrate property influences the properties of SAGC. So SAGC has semiconductor properties within the confined space up to 458nm. When the gap distance gets up to 484nm, the structure with guanosine shows resistance characteristics. The photocurrent measurements show that the bandgap of SAGC is about 3.3-3.4eV and affected by substrate properties. The MSM structure based on SAGC can be used as photodetector in UV region.

Then I show that the periodic structure based on GaN and SAGC can have photonic bandgaps. The bandgap size and the band edges can be tuned by tuning lattice parameters. Light propagation and emission can be tuned by photonic crystals. So the hybrid photonic crystal can be potentially used to detect guanosine molecules. If guanosine molecules are used as functional linker to other biomolecules which usually absorb or emit light in blue to UV region, the hybrid photonic crystal can also be used to tune the coupling of light source to guanosine molecules, then to other biomolecules.

ACKNOWLEDGEMENTS

In the past several years, many people contributed to the work of my dissertation. I would like to recognize the contributions that I received.

First of all, I wish to thank my advisor, Prof. Arup Neogi for introducing me to the field of nano-photonics. His enthusiasm, insight, and intelligence have inspired me. He also helped me with great patience in doing experiments and preparing presentations. I learned a lot from him, like how to solve research problems from very beginning and schedule work time more efficiently.

I also want to thank my committee members, Profs. Chris Littler, Zhibing Hu, and Arkadii Krokhin, for their help with the preparation of my dissertation. They gave me many good suggestions to organize and correct my dissertation.

I want to thank Prof. Hadis Morkoç, Drs. Ümit Özgür, and S. J. Cho at the Department of Electrical Engineering, Virginia Commonwealth University for providing GaN samples and the fabrication of electrodes. Dr. Ability Sarkar in Michigan Molecular Institute helped me on synthesis of deoxyguanosine molecules. Harsheetal Liddar in our group helped me to do atomic force microscopy measurements of the surfaces of GaN and deoxyguanosine films.

Finally, I would like to thank my parents, my wife and others in my family. Without their strong support and encouragements, I wouldn't pass all the bad times I had.

TABLE OF CONTENTS

Page

LIST OF TABLES

Page

LIST OF FIGURES

Page

CHAPTER 1

INTRODUCTION

1.1. Background

Semiconductor devices can hold more transistors and have improved efficiency if transistors can be made smaller. In 1965, Gordon E. Moore predicted that the density of transistor of a circuitry based on silicon doubles about every 18 monthes[1]. That was called Moore's law. The device integration density on silicon chips increases steadily for about four decades by following Moore's law. The leading semiconductor companies can manufacture devices with feature size less than 100nm. A modern microprocessor can have more than 500 million transistors. Electronic integrated circuits are inherently single-channel connected device arrays within a two-dimensional printed circuit board[2]. By further shrinking transistor size, it is facing technical, physical and economical limits. These limits will be reached in a few years[3]. At the same time, insulator is getting thinner and finally current leakage will cause short circuit[4]. Manufacture cost increases drastically with further size reduction.

Those limitations and application requirements inspired extensive research aimed at developing new materials, device concepts, and fabrication approaches that may enable the integrated devices to overcome the limitations of the conventional microelectronic technology. Researchers in semiconductor industry and academy are looking for alternative materials to overcome these limits. Hybrid organic-inorganic system is one of alternative solutions. Hybrid organic-inorganic materials can be integrated into one nanoscale composite[5] and harness the properties of both organic and inorganic materials. Organic materials are structural flexible and can have high efficient luminescence and large degree of polarizability because organic molecules generally interact weakly by hydrogen bond and van der Waals force. The manufacture cost of the devices based on organic materials can be low because

they can be massive produced. The electronic properties of the materials can also be tuned. Inorganic material molecules typically interact strongly by covalent and ionic bond. So inorganic materials can have high electrical mobility, a wide range of bandgaps and dielectric constants, and substantial mechanical and thermal stability[6]. By intelligent design, the hybrid system can have properties that either component does not exhibit or even have more significant properties than that of either component[7]. During past years, diode and transistor based on carbon-nanotube, DNA, and other materials[8, 9, 10, 11, 12] have already been fabricated.

Like the trend in electronic technology, the shrinking of optical devices and systems to nanoscale is essential for photonic technology. Compared with electronic circuits, photonic circuits are multiple wavelength channels that information can flow simultaneously and don't have crosstalk or heat dissipations problems[2]. The integrated circuits of photonic devices can have lower cost, smaller size, lower power dissipation[13], improved performance, higher yield throughput. So there is a tendency to replace "slower" electronic devices with "faster" photonic devices. The integration of photonic devices requires novel approaches of controlling, routing, and processing optical signals[14].

Conventional photonic devices like light emitting diode (LED), laser diode (LD) or photonic crystals (PC), generally based on Si, GaAs or InP, are working only in infrared (IR) region. Those semiconductors can not work in the regions from visible to ultraviolet (UV) because the bandgaps of Si, GaAs and InP are 1.12eV, 1.43eV and 1.29eV respectively. They absorb light in those regions. Wide-bandgap semiconductors are essential to make devices working in visible to UV regions. Wide-bandgap semiconductors are generally compound materials, like III(indium, gallium, or aluminium)-nitride (InN, GaN and AlN), silicon carbide (SiC), zinc oxide (ZnO). III-nitride semiconductors are direct bandgap. Because the bandgaps of InN, GaN and AlN are 0.65eV, 3.43eV and 6.05eV at room temperature[15], respectively, the bandgaps of III-nitride compounds can cover the whole range from infrared to ultraviolet.

1.2. Photodetector

A variety applications in military, scientific and security drive the development of ultraviolet (UV) photodetector that is sensitive to UV but blind to visible light[16, 17, 18, 19]. Because silicon is narrow bandgap semiconductor and silicon photodetectors absorb near-infrared to ultraviolet light, the detector background is high[17]. Band filters are required to block visible light background[20]. While wide bandgap semiconductors don't absorb visible light and are sensitive to UV, the photodetectors based on wide bandgap semiconductors are sensitive only to UV. The design of photodetector can be simplified because the filters are not used[17]. Gallium nitride (GaN), one of the widely used direct, wide-bandgap semiconductors, can be used for UV photodetector[20, 16, 17, 18, 21].

1.3. Photonic Crystals

Photonic crystals (PC) or photonic band gaps (PBG) are periodical structures with alternatives dielectric materials in one-, two-, or three-dimension. It was first proposed almost simultaneously by E. Yablonovitch[22] and S. John[23], respectively, in 1987. In last two decades, PCs are widely studied and used as waveguides[24, 25], fibers[26, 27, 28, 29], and microcavities[30] to control light propagation and emission. The periodicity of the structure is usually in the order of light wavelength in the material that the photonic crystal is made of. Photonic band gap is open under certain circumstances, like suitable lattice structure, parameters and refractive index contrast of the composed materials. That is certain electromagnetic wave modes don't exist in the bandgap within photonic crystals. So photonic crystals influence spontaneous emission rate and light wave propagation. Bandgap can open in all direction with three-dimensional structures. But it is very difficult to fabricates[31, 32] photonic crystals in three-dimension. Photonic crystal slabs, as shown in Fig. 1.1 are two-dimensional structures with finite thickness. It uses totally internal reflection to confine light inside the slab[33]. This structure are widely used because it is much easier to fabricate. Bandgap will be very small if slab thickness is too small because guided mode is very close to light cone and very weakly confined. If the slab is too thick, bandgap is also small because

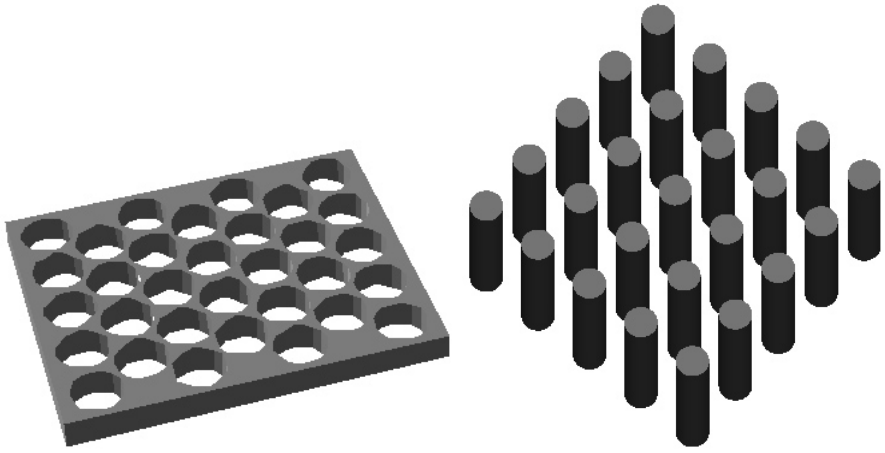

(a) (b)

FIGURE 1.1. Photonic crystal slab (a)Triangular lattice of holes in dielectric slab. (b) Square lattice of rods in air.

higher-order mode in vertical direction can be easily added. There is an optimum slab thickness so that photonic crystal slab has the largest bandgap for certain lattice parameters[33]. Because of imperfect confinement along direction perpendicular to slab surface, the performance of optical devices based on PC slabs is not as good as that of photonic crystal with real three-dimensional confinement. So PC slabs are quasi three-dimensional. A variety of passive and active optical components can be fabricated and integrated into one chip by introducing defects into PC slabs.

1.4. Basic Properties of Used Materials

1.4.1. *III-Nitride*

III-nitrides are direct wide-bandgap III-V semiconductors. They have low dielectric constants, high thermal conductivity, and resistant to chemical etching[34]. So the devices based on III-nitrides can be used in harsh conditions. Because the bond strengths are very high, the melting points are also high. It probably is the same reason that thread dislocations are prohibited to move and the reliability of devices based on such semiconductors is superior than the devices based on II-VI and other III-V semiconductors[35]. They have both

wurtzite and zinc-blende lattice structures. The wurtzite lattice structure is thermodynamically stable[36, 37] and more commonly used. The electronic properties of two crystalline structure are related, but different[34]. Because there is no native substrates for III-nitrides, they have large lattice mismatch to substrates. Although sapphire substrate has large lattice mismatch, it is widely used because high quality GaN has already been grown on it. In Table 1.1, lattice constants of nitrides and sapphires are listed. Because the lattice mis-

TABLE 1.1. Lattice constants of III-nitrides and sapphire

	AlN	GaN	InN	Sapphire
a	3.111Å	3.189Å	3.544Å	4.758Å
c	4.980Å	5.182Å	5.718Å	12.991Å

match between GaN and sapphire substrate is about 16% when GaN is grown along c(0001) direction, the density of threading dislocation can reach up to 10^{10}cm^{-2}[38].

The bandgap of InGaN alloy covers from red to UV region of spectrum because the bandgaps of InN and GaN are 0.65eV and 3.43eV at room temperature, respectively. The alloy is thought to be direct in entire alloy range[35]. The direct bandgap materials can have high quantum efficiency and be potentially used for light emitters and photodetectors. InGaN is used as active layer in quantum well structures. Although InGaN quantum wells are widely used for LED and laser diode(LD), the emission mechanisms are still not totally explained because of large lattice mismatch and polarization of wurtzite lattice structure. The large lattice mismatch can cause phase separation and form thread dislocation that may act as non-radiative centers. The strong polarization has quantum confined Stark effect (QCSE) that reduces oscillator strength, red-shift emission energy of quantum wells, or blue-shift emission energy with increasing excitation intensity[15].

1.4.2. *Self-Assembled Guanosine Supramolecule*

DNA carries the genetic code of organisms and has a fundamental role in biological processes. It has four bases: guanosine (G), cytosine (C), adenine (A), and thymine (T).

The base guanosine can only pair with cytosine by three hydrogen bonds. The base adenine can only pair with thymine by two hydrogen bonds. The properties of self-assembly and self-recognition and the ability to synthesize to any sequence make DNA potentially used in molecular electronics and nanotechnology[39, 40, 41]. DNA can be used as template or element of nano-circuits.

The four bases are aromatic compounds with planar, unsaturated, benzene-ring structure. The atomic p_z orbitals of the bases which are perpendicular to the base plane can form delocalized π bonds and π^* anti-bonds[40]. The energy difference of the two bonds is 3.75eV[42]. If the bases are brought together and their interaction is strong enough, the energy levels broaden. Finally, the energy band gap can be formed with reduced energy. Based on the above considerations, Eley and Spivey suggested that the stacked DNA bases can be conductive[43]. There are several factors that complicate the conductive behavior of DNA. First, unlike conventional crystals, DNA helical structures are not periodic. Second, non-negligible forces on stacked DNA bases by surrounding water molecules and counterions must also be considered. Finally, DNA bases have much large vibration compared with conventional crystal atoms. Experimental conductive results of DNA cover from insulator[8, 44, 45, 46], semiconductor[47], ohmic[48, 49, 50, 51, 52], even superconductor[53] depending on experimental condition, DNA sequences, length of the sequence, DNA molecular character, microstructure used, interfacial character, and preparation protocol. By modifying base radicals and doping, conductivity of DNA can be tuned[40].

There are two theoretical approaches to study DNA conductivity, model calculation and *ab initio* calculation with Hartree-Fock method, density function theory (DFT), and quantum molecular dynamics methods. Because experimental results of conductivity are not conclusive, the degrees of freedom and the energy scales are difficult to be determined in model calculation. Single charge transfer is a developed model with several different mechanisms proposed. The mechanism can be one or a combination of superexchange[54], incoherent hopping[55, 56, 57] or band-like transport[58] depending on DNA sequence and

donor-bridge-acceptor energetics. In *ab initio* calculation, the number of unit cells is restricted by computation capacity of computers.

DNA structure can be changed by the presence of water molecules because DNA bases have hydrophobic base. DNA has stable B form if one nucleotide has more than 13 water molecules[59] and A form if there are 5-10 water molecules around one nucleotide. B form has stronger atomic p_z overlapping between neighboring bases. The electronic coupling in A form is almost zero because of the competition between σ and π coupling of p_z orbitals[40]. Mechanical stretching can cause other form of DNA structures. Meanwhile, the dipole moment of water molecules is also changed by the presence of charged DNA[60].

Among DNA bases, guanosine has the lowest oxidation energy, which favors charge transfer[61]. Guanosine and cytosine have the largest polarity among the bases[62]. The strong intrinsic dipole moment of guanosine is up to 7 Debye[62, 63], so self-assembled guanosine crystals (SAGCs) also have strong polarity. As shown in Fig. 1.2, the unique

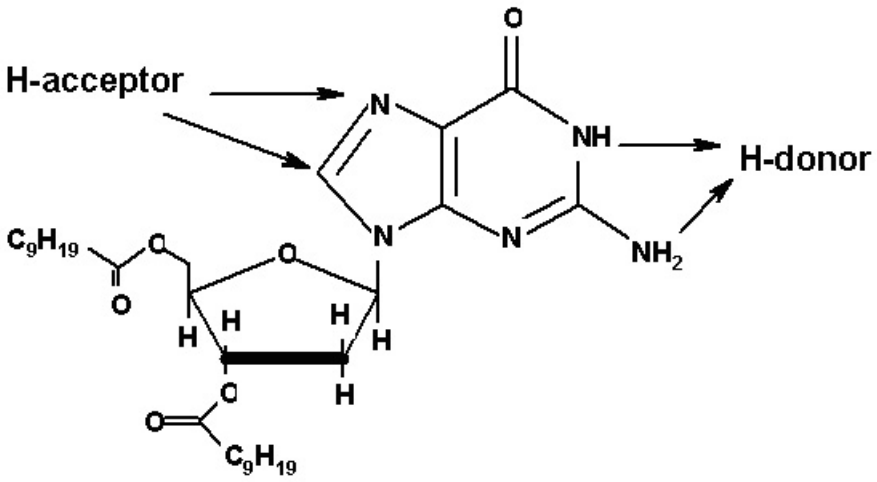

FIGURE 1.2. Guanosine base structure.

sequence groups of guanosine work as donor or acceptor of hydrogen bonds[64]. Those groups play an important role in self-assembling and self-recognition processes. Rinaldi et al. modified guanosine molecules and tested different solvents to tune the conduction of

the self-assembled structures[65]. The modification of guanosine molecules adjusts the potential difference between molecules and contacts. The solvents can change the length of self-assembled supramolecules so that the length is in the order of resolution of modern lithography technology. The modified guanosine derivatives self-assemble into ribbon-like structure (as shown in Fig. 1.3) on silicon substrate if its concentration in chloroform ($CHCl_3$) is 3.3×10^{-2}M. They found that SAGC behaves like diode by current-voltage characterization if the distance between electrodes is less than 100nm[65]. The bandgap of SAGC is about 3.4eV by photocurrent measurements[65].

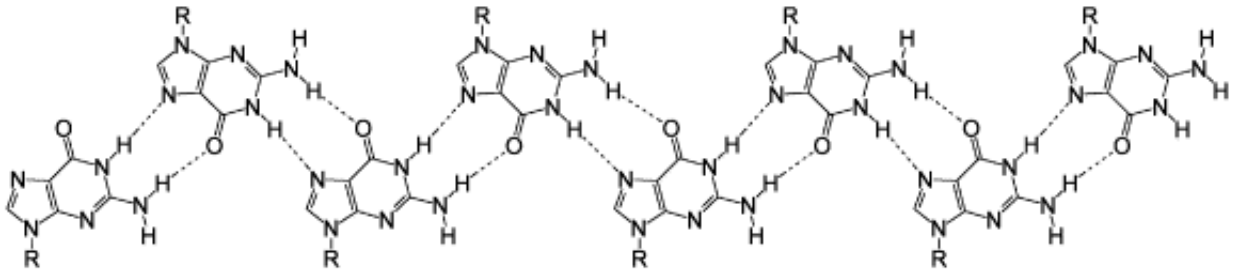

FIGURE 1.3. Self-assembled ribbon-like structure of deoxyguanosine derivatives on solid state surface. Reprinted with permission from R. Cingolani, et al., *Phys. E*, 13, 1229, (2002). ©2002 Elsevier Science B.V.

1.5. Overview of the Dissertation

In this work, we concentrate on the optical and electrical properties of hybrid nanostructures based on wide-bandgap semiconductor gallium nitride. There are four parts in this work. In the first part, the current-voltage characteristic of metal-semiconductor-metal structure is discussed. The second part is about current-voltage characteristics of self-assembled guanosine structure (SAGC) in nano-electrodes. The third part is the photocurrent measurement of SAGC in nano-structure. The last part is about the GaN/SAGC hybrid photonic crystal.

CHAPTER 2

CURRENT-VOLTAGE CHARACTERISTIC OF METAL-SEMICONDUCTOR-METAL STRUCTURE

2.1. Schottky Contacts

Metal-semiconductor contacts can behave like Schottky contact or ohmic contact. At ideal condition, ohmic contacts have no energy barrier between metal and semiconductor. But the energy barrier is not zero for Schottky contacts. Fig. 1(a) shows the band diagram of metal and n-type semiconductor before they get contacted. In the figure, E_{vac} is the energy level of vacuum. E_{Fm} is the Fermi level of the metal. q is the magnitude of electron charge. $q\Phi_m$ is the work function of the metal that is the potential difference between Fermi level and vacuum energy level. E_c, E_v, and E_{Fs} are conduction band edge, valence band edge and Fermi energy of the semiconductor, respectively. $q\chi_s$ is the electron affinity of the semiconductor that is the energy difference between conduction band edge and vacuum energy level. $q\Phi_n$ is the energy difference between Fermi level and conduction band edge in the semiconductor. When the two materials get closed and form intimate and abrupt contact, negative charges accumulate at metal side and positive charges with equal amount also accumulate at semiconductor side because of Fermi levels alignment in the two materials. Then, valence band and conduction band bend and potential barrier forms between metal and semiconductor, as shown in Fig. 1(b). If the semiconductor is p-type, the bands bend downward instead of upward for n-type semiconductor. In the figure, Φ_b is the potential barrier height that electrons must overcome to move from metal to semiconductor. The barrier height is given by

$$\Phi_b = \Phi_m - \chi_s \tag{1}$$

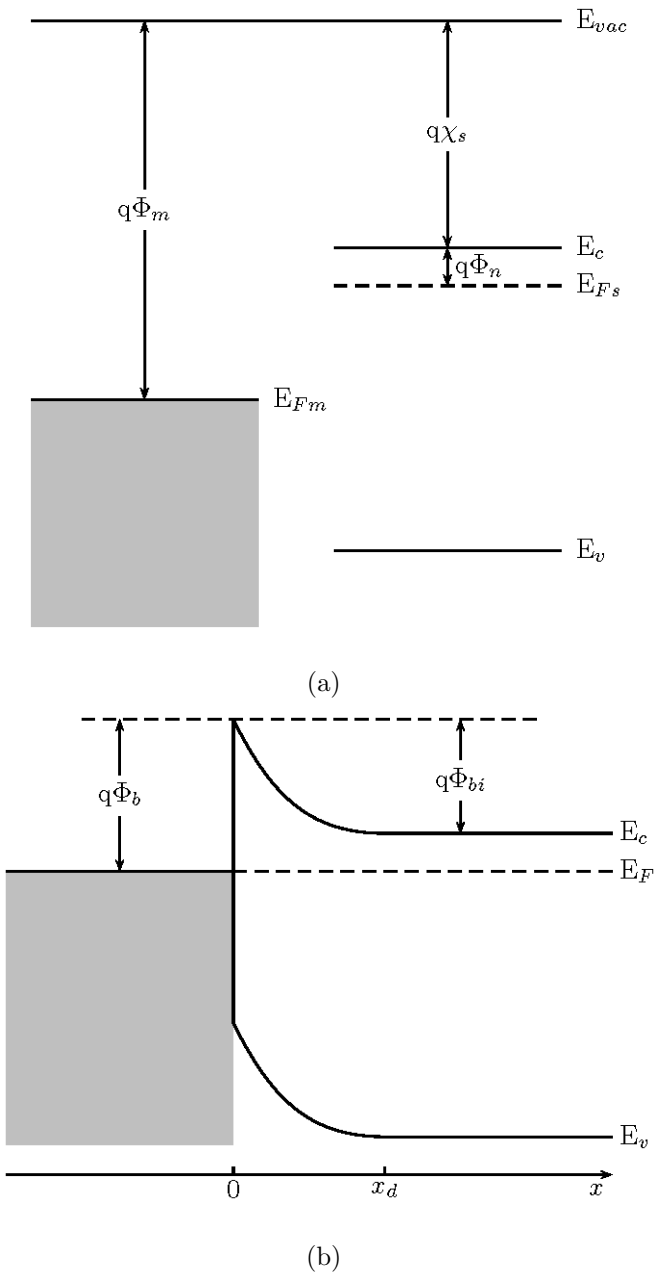

FIGURE 2.1. (a) The band diagram of separated metal and semiconductor. (b) The band diagram of Schottky contact without applied bias voltage.

Φ_{bi} is the built-in potential that electrons must overcome to move from semiconductor to metal. The built-in potential is given by

$$\Phi_{bi} = \Phi_b - \Phi_n \tag{2}$$

Because the carrier concentration is relatively low in semiconductor compared with that of metal, the positive charges are distributed from the metal-semiconductor interface to certain depth in semiconductor. The layer that has the positive charges is depletion region. x_d is the edge of depletion layer.

Suppose the depletion layer has abrupt edge and the donors in the layer are fully depleted, the positive charge density $\rho = qN_D$ inside the depletion layer, where N_D is the donor concentration. Otherwise, the charge density is 0. By solving Poisson's equation inside the depletion layer in one-dimension

$$\frac{dE(x)}{dx} = \frac{\rho}{\varepsilon_s} = \frac{qN_D}{\varepsilon_s} \tag{3}$$

where ϵ_s is the dielectric constant of the semiconductor. We get

$$E(x) = \frac{qN_D}{\varepsilon_s}(x - x_d) \tag{4}$$

with boundary condition $E(x) = 0$ for $x \geq x_d$. The maximum electric field $|E_{max}| = qN_d x_d/\varepsilon_s$ at $x = 0$, which is the interface position. By integrating electric field in the depletion layer, the potential in the layer is

$$\psi(x) = -\int_0^x E(x')dx' = -\frac{1}{2}\frac{qN_D}{\varepsilon_s}[(x_d - x)^2 - x_d^2] = \frac{qN_D}{\varepsilon_s}(xx_d - \frac{1}{2}x^2) \tag{5}$$

So the built-in potential

$$\Phi_{bi} = \psi(x_d) - \psi(0) = \frac{1}{2}\frac{qN_D}{\varepsilon_s}x_d^2 = \frac{1}{2}E_{max}x_d \tag{6}$$

Then we can get the thickness of the depletion layer without applied bias voltage

$$x_d = \sqrt{\frac{2\varepsilon_s}{qN_D}\left(\Phi_{bi} - \frac{kT}{q}\right)} \tag{7}$$

The correction term kT/q comes from the majority carriers distribution tail, where k is Boltzmann constant and T is temperature.

If bias voltage is applied to the contact, the built-in potential and also the depletion layer thickness are changed. The built-in potential decreases if the metal is applied with positive voltage and the semiconductor with negative voltage, as shown in Fig. 2(a). The

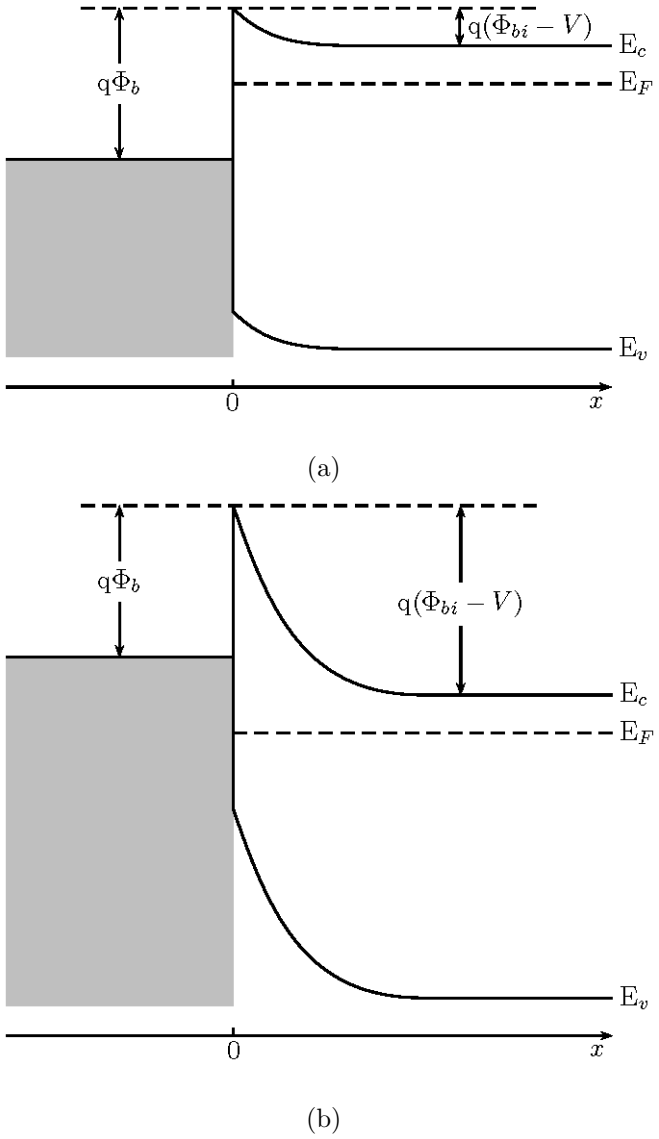

FIGURE 2.2. (a) Energy band diagram of forward bias. (b) Energy band diagram of reverse bias

Fermi energy of metal is lowered relative to that of semiconductor. This is the forward-bias condition. The electrons move easier from semiconductor to metal because of the lower barrier. The thickness of the depletion layer is also decreased, then the electric field at interface is weaker. The built-in potential increases if the metal is applied with negative voltage and the semiconductor with positive voltage, as shown in Fig. 2(b). The Fermi energy of the metal is higher than that of the semiconductor. The thickness of the depletion layer

increases, then the electric field at the interface is stronger. Meanwhile, the electrons have to overcome higher barrier to move from semiconductor to metal. This is the reverse condition. But the potential barrier height Φ_b doesn't change. That means, at ideal condition, the electrons in metal still have the same barrier height moving from metal to semiconductor no matter what the applied bias voltage is.

With applied bias voltage V (positive for forward bias and negative for reverse bias), the built-in potential now changes to $\Phi_{bi} - V$ and the thickness of depletion layer changes to

$$x_d = \sqrt{\frac{2\varepsilon_s}{qN_D}\left(\Phi_{bi} - V - \frac{kT}{q}\right)} \tag{8}$$

At forward-bias condition, the junction can have large current because of lowered built-in potential. At reverse-bias condition, the junction has small current because of raised built-in potential. So the junction has rectifying effect.

2.1.1. *Barrier Height Changing Effects*

For ideal, intimate and abrupt contacts, the barrier potential height depends only on the work function of the metal and the electron affinity of the semiconductor. But in reality, the barrier height can be changed by Schottky effect and metal-induced-gap-states (MIGS) effect. So the current-voltage relation is more complicate and deviates from the ideal curve. Even for same metal and semiconductor, the surface of the materials can be different due to varied fabrication conditions. This will make the current-voltage characteristic of the device even more complicate. But we are going to discuss only Schottky effect and MIGS effect in this work.

2.1.1.1. *Schottky Effect.* Schottky effect is the lowering of barrier height due to induced charges at the metal-semiconductor interface by charged carriers in semiconductor. Suppose an electron exists at position x in semiconductor from the interface of metal and n-type semiconductor, it induces positive surface charge on the metal surface, as shown in Fig. 3(a). The interaction of the electron and the induced surface charge is equivalent to the interaction of the electron and its image with positive charge at $-x$ in metal (Fig. 3(b)). This interaction

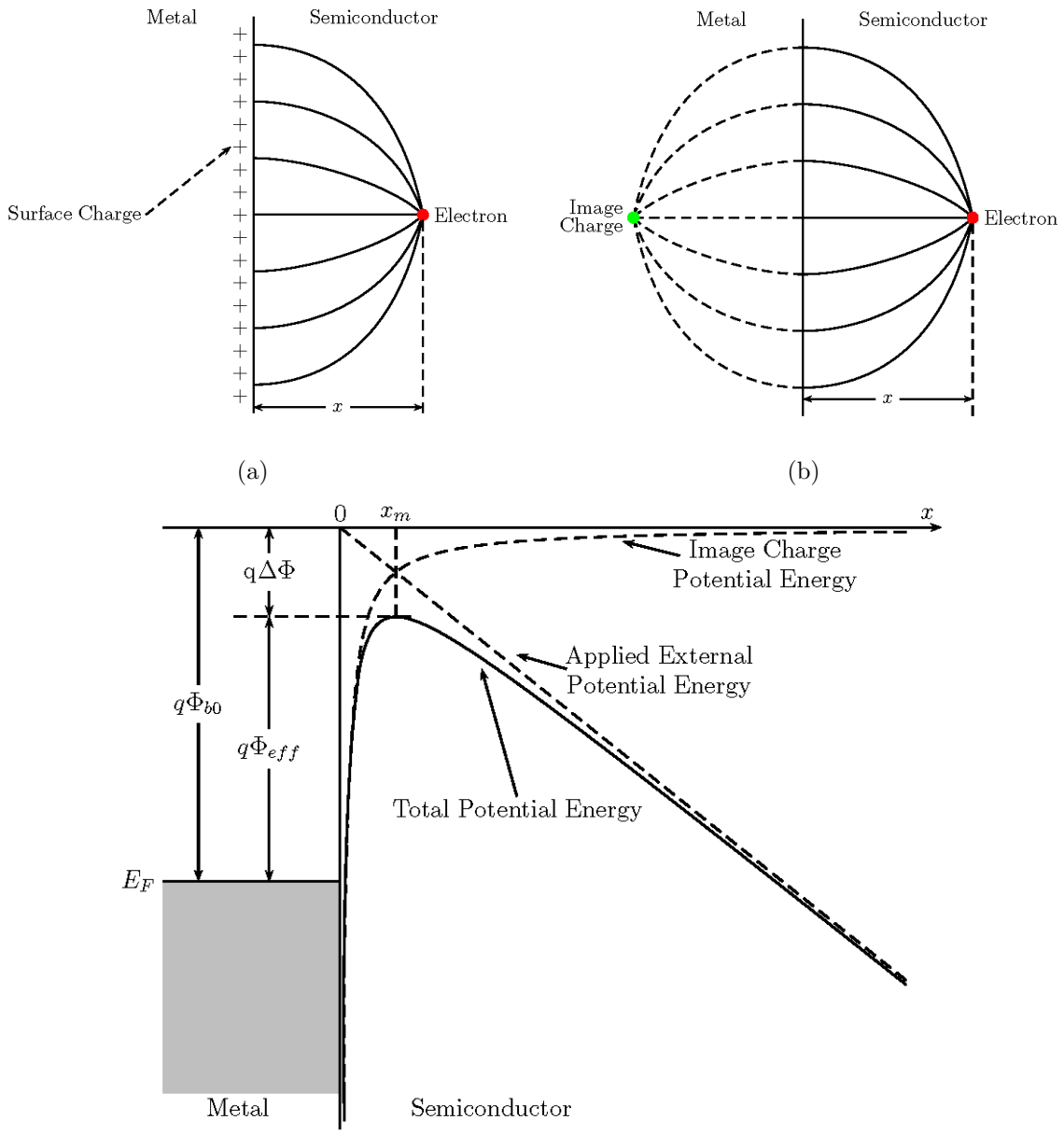

FIGURE 2.3. (a) Electron in semiconductor and induced positive charges on metal surface. (b) Electron in semiconductor and positive image charge in metal. (c) Band diagram of Schottky effect.

will reduce the barrier height, as shown in Fig. 3(c). The force between the electron and its

image charge is

$$F = -\frac{q^2}{4\pi\varepsilon_s(2x)^2} = -\frac{q^2}{16\pi\varepsilon_s x^2} \tag{9}$$

Then the work that moves the electron from infinity to position x is

$$W = -\int_{\infty}^{x} F(x)dx = -\frac{q^2}{16\pi\varepsilon_s x} \tag{10}$$

Suppose an external electric field E is applied along x direction, the total potential energy of an electron at position x in semiconductor is

$$\psi(x) = -qEx - \frac{q^2}{16\pi\varepsilon_s x} \tag{11}$$

At the highest potential energy at position x_m, $\left.\frac{d\psi(x)}{dx}\right|_{x=x_m} = 0$. Then from above equation, we can get

$$x_m = \sqrt{\frac{q}{16\pi\varepsilon_s E}} \tag{12}$$

From Fig. 3(c) and Eq. 11, the lowering of potential barrier height is

$$\Delta\Phi = |\psi(x_m)| = \sqrt{\frac{qE}{4\pi\varepsilon_s}} \tag{13}$$

Because the Schottky effect is mainly in the layer very close to the interface, the electric field at the interface, which is the maximum electric field, can be used in the above equation. From Eq. 4, Eq. 8, and set $x = 0$, then the above equation changes to

$$\Delta\Phi = \sqrt{\frac{qE_{max}}{4\pi\varepsilon_s}} \tag{14}$$

with the maximum electric field

$$E_{max} = \sqrt{\frac{2qN_D}{\varepsilon_s}\left(\phi_{bi} - V - \frac{kT}{q}\right)} \tag{15}$$

From the above equation, we can see that the lowering of the barrier height is proportional to the 1/4 power of applied voltage. At forward bias condition, the barrier height lowering is less than that at zero bias voltage because the applied voltage is positive. At reverse bias condition, the barrier height lowering is greater than that at zero bias voltage. So the carriers

can move easier from metal to semiconductor at reverse bias condition than at forward bias condition.

In the derivation of the barrier height lowering, the static permittivity ε_s of bulk semiconductor is used. If the interface emitted electrons move from the interface to $x = x_m$ in a shorter time than the dielectric relaxation time, the semiconductor is not fully polarized in such a short time. Then the permittivity in the region near the interface from $x = 0$ to $x = x_m$, may be different from that of the static value.

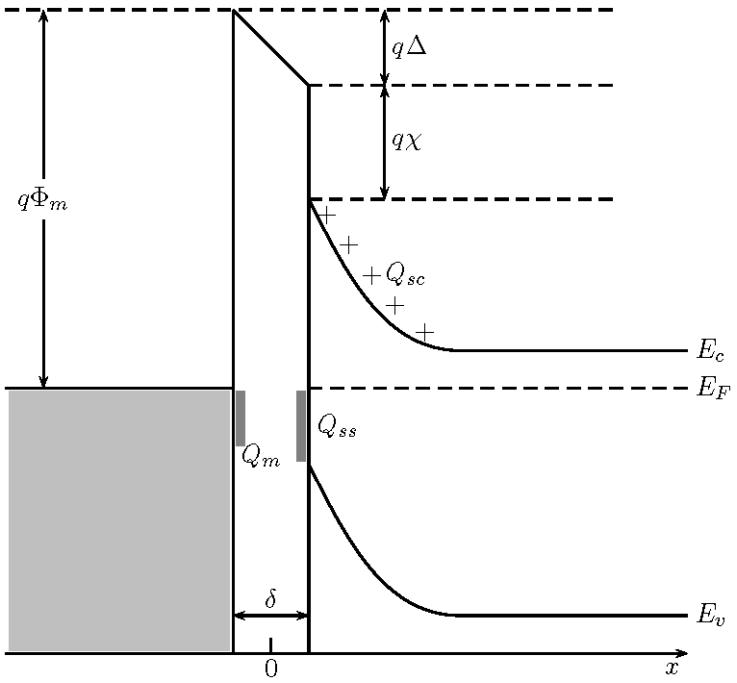

FIGURE 2.4. Schematic of energy band diagram of metal and n-type semiconductor contact with an interfacial layer and the charge distribution in the layer.

2.1.1.2. *Metal-Induced-Gap-States.* As metal gets contact with semiconductor, as shown in Fig. 2.4, the conduction band of the metal overlaps with both valence band and the part of forbidden band below Fermi level. The wave functions of states near the interface on both sides are bulk-like if the energy of the states is below the valence band edge. But the wave function of metal can only tunnel into the forbidden band gap of semiconductor because of the continuity condition of wave function if the energy of the stats is above the

valence band edge and below Fermi level[66]. The wave function tail causes the formation of a metal-semiconductor interface layer and energy states inside the layer[67]. The states are called metal-induced-gap-states[68]. The MIGS is dominantly donor-like if the states are closer to valence-band edge and acceptor-like if the states are closer to conduction band edge. The branch point is the energy of the states at which the dominant characteristics of MIGS changes. The net charge in the layer can be positive, neutral, or negative depending on whether the branch point is above, equal, or below the Fermi level.

At thermal equilibrium, the interface is electrically neutral. So

$$Q_m + Q_s = 0 \tag{16}$$

where Q_m is the charge at metal side and Q_s is the charge at semiconductor side. On the semiconductor side, the charge includes surface charge at interface and space charge in the depletion layer. Then we can rewrite the above equation as

$$Q_m + Q_{ss} + Q_{sc} = 0 \tag{17}$$

where Q_{ss} is the surface charge and Q_{sc} is the space charge in the depletion layer. The charges at interface form a layer with thickness, δ, in the order of angstroms and the potential drop across the layer is Δ. Due to the alignment of Fermi level of metal and surface states, the surface states Q_{ss} and the potential drop Δ depend on the applied voltage[69].

Because the surface states and the bulk traps in the depletion layer are in thermal equilibrium with the metal and the semiconductor, respectively, there is a region close to the interface whose quasi-Fermi level stays in between the Fermi levels of the metal and the semiconductor. Inside this layer, the states filled with electrons are in thermal equilibrium with the semiconductor and the empty states are in thermal equilibrium with the metal. That means, part of the states in this near-surface layer (NSL) are always in thermal equilibrium with the semiconductor and the accumulated charge is voltage dependent. Electrons can tunnel through the near-surface layer, just like through the barrier, Δ, of the interface layer. If the density of states inside the layer is too low, it can be just neglected. If the

density of states inside the layer is too high, the effect can not be differentiated because the electron transport is not sensitive to the barrier shape. Brillson, et al.[70] and Hashizume, et al.[71] observed the states below conduction band edge near the interface and inside the depletion region due to metal deposition on GaN and AlGaN surfaces, respectively. The charge density in NSL can increase or decrease the charge density inside the depletion layer, so it can be very different from the other part in the depletion region.

Suppose Δ_{NSL} is the potential drop across the near-surface layer with the thickness δ_{NSL}. It is voltage dependent. If we don't consider Schottky effect, the barrier height can be written as

$$\Phi_{eff} = \Phi_{b0} - \Delta_{NSL} \tag{18}$$

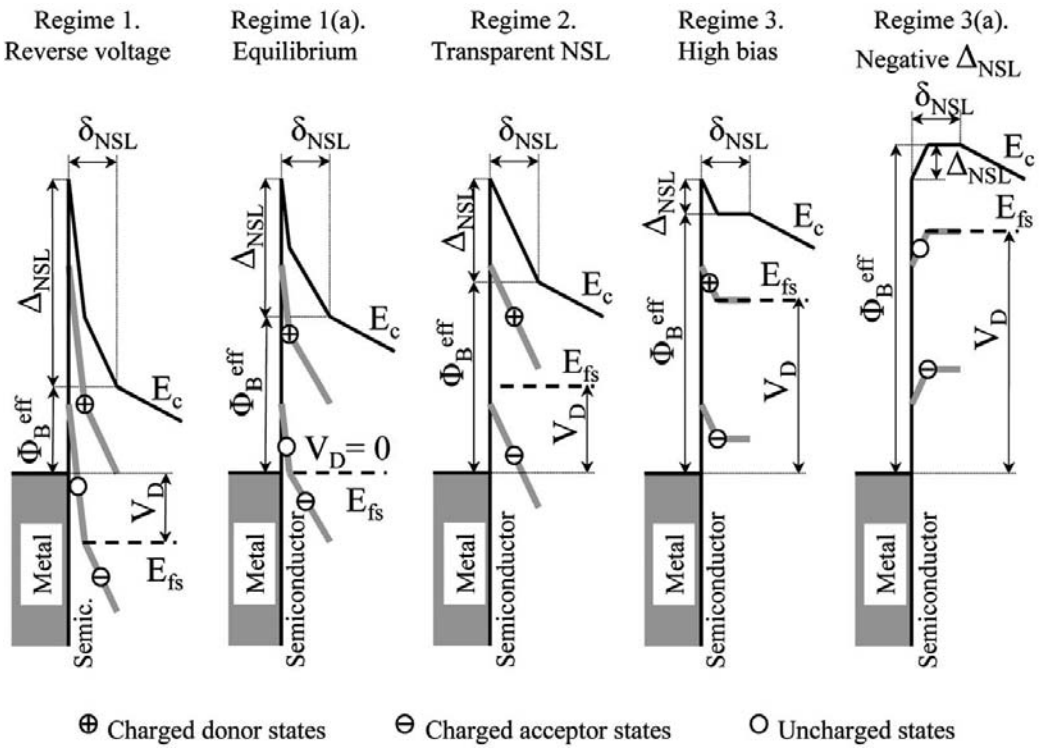

FIGURE 2.5. Schematic representation of the role of a NSL in an energy-band diagram of a Schottky interface. For simplicity, the interfacial layer is not shown. Reprinted with permission from Cojocari and Hartnagel, *J. Vac. Sci. Technol. B*, 24, 2544 (2006). ©2006, American Institute of Physics

In the Fig. 2.5, donor and acceptor states in near-surface layer are shown. The states just below the conduction band are donors and the states just above the Fermi level of the metal are acceptors. We assume that the density of donors is higher than that of acceptors. Depending on the quasi Fermi level, there are three different regimes.

(1) The quasi Fermi level is close to the acceptor states in this regime. As the applied voltage increases, the total negative charges of acceptors decrease. The first and second figures of Fig. 2.5 show the effect. The potential Δ_{NSL} increases because of the remained positive charged donors. Then according to Eq. 18, the effective barrier height is higher.

(2) Negative charged acceptors only neutralize part of positive charged donors near the quasi Fermi level, as shown in the third figure of Fig. 2.5. The potential drop Δ_{NSL}, is relative stable with the change of applied voltage. Then the near-surface layer is transparent to current flow.

(3) The quasi Fermi level is close to the donor states in this regime. Suppose both donor and acceptor have higher density than the doping concentration and either donor or acceptor has much higher state density than the other. As shown in the fourth figure of Fig. 2.5, if the applied voltage increases, the total positive charge of donors decreases. Then the potential Δ_{NSL} decreases, the effective barrier height Φ_{eff} increases. The positive charged doping atoms are neutralized by the relative dense acceptors in NSL, and the remained negative charged acceptors can raise the conduction band edge. Then the donor density is tend to increase and reduce the effect of acceptors. So the quasi Fermi level in NSL has constant energy difference compared with donor states and conduction band edge. That means, the quasi Fermi level is pinned to the donor states in NSL. So the conduction band in the near-surface layer has flat region. If the voltage is too high, as shown in the fifth figure of Fig. 2.5, the potential Δ_{NSL} can be negative, the effective barrier gets higher.

For a very coarse approximation, we assume that the thickness δ_{NSL} doesn't change with the applied voltage and the net charge density ρ inside NSL changes linearly with the applied voltage at regime 1 and 3. The potential Δ_{NSL} can be written as

$$\Delta_{NSL}(V) = \frac{1}{2}\frac{\rho(V)}{\varepsilon_s}\delta_{NSL}^2 = c_1(V - c_2) \tag{19}$$

following Eq. 6 with constants c_1 and c_2.

2.1.2. *Current Transport Properties*

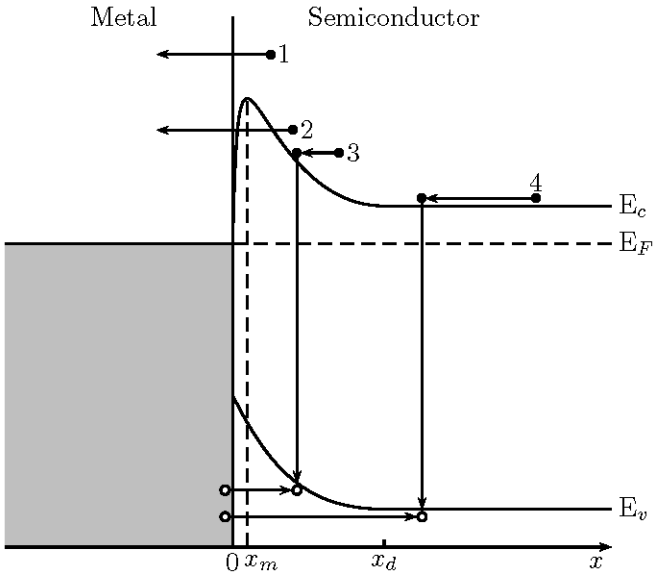

FIGURE 2.6. Schematic of four different transport mechanisms in metal-semiconductor (n-type) contact.

Here we just consider metal and n-type semiconductor Schottky contact now. The Schottky contact is unipolar device because the current transport is mainly by majority carriers. There are four transport mechanisms in the device, as shown in Fig. 2.6. First, electrons with energy higher than the barrier height transport from semiconductor to metal. This is the dominate mechanism for the semiconductor with moderate doping. Second, electrons with energy lower than barrier height tunnel through the barrier to metal. This mechanism is mainly occurred in heavily doped semiconductor. Third, electron-hole recombination in

depletion layer. Fourth, holes are injected from metal to semiconductor. This mechanism is actually the electron-hole recombination in neutral region.

For the first transport mechanism, there are thermionic emission, diffusion, and combined thermionic-diffusion theories. Usually, thermionic emission theory is applied to high-mobility semiconductor device and diffusion theory is applied to low-mobility semiconductor device.

2.1.2.1. *Thermionic Emission Theory.* Thermionic emission theory proposed by Bethe[72] is based on the assumptions that the electron energy is much larger than kT and higher than the barrier height so that the shape of the barrier can be ignored. The current depends only on the barrier height and carrier concentration. Meanwhile, thermal equilibrium is also established at metal-semiconductor interface.

At first, we don't consider Schottky effect, that means the barrier height doesn't change with applied bias voltage. By integrating the carriers with energy higher than barrier height and moves along $-x$ direction, the current density flow from semiconductor to metal is

$$J_{sm} = \int_{E_F+q\Phi_{b0}}^{\infty} qv_x dn \tag{20}$$

where v_x is the carrier velocity along $-x$ direction. In consideration of density of states and distribution function of carriers, finally the current density can be written as[73]

$$J_{sm} = A^* T^2 \exp(-\frac{q\Phi_{b0}}{kT}) \exp(\frac{qV}{kT}) \tag{21}$$

where

$$A^* = \frac{4\pi q m^* k^2}{h^3} \tag{22}$$

is the effective Richardson constant of thermionic emission. Quantum mechanical reflection and optical phonon scattering effects are not considered in the above derivation. h is Planck's constant. m^* is the effective mass of carriers in semiconductor and depends on the carrier transport direction in semiconductor. If the effective mass of the carriers at conduction band edge is isotropic, $A^*/A = m^*/m_0$ where m_0 is the mass of free electron, $A = 120 A/cm^2K^2$ is Richardson constant for free electron. For semiconductors with anisotropic effective mass,

the effective Richardson constant of a single energy minimum is[74]

$$\frac{A_l^*}{A} = \frac{1}{m_0}(l_1^2 m_y^* m_z^* + l_2^2 m_z^* m_x^* + l_3^2 m_x^* m_y^*)^{1/2} \tag{23}$$

where $l = (l_1, l_2, l_3)$ is the direction of the emitting plane. l_1, l_2, l_3 are the projections of l to principal axes of the ellipsoid. m_x^*, m_y^*, and m_z^* are the components of the effective mass tensor.

When electrons flow from metal to semiconductor, the current density doesn't change with applied bias voltage because the barrier height is independent of the bias voltage. Then the current density should be same as the current density from semiconductor to metal by setting the applied bias voltage to zero. The current density flowing from metal to semiconductor is

$$J_{ms} = -A^* T^2 \exp(-\frac{q\Phi_{b0}}{kT}) \tag{24}$$

By adding Eq. 21 and Eq. 24, the total current density is

$$\begin{aligned} J_n &= A^* T^2 \exp(-\frac{q\Phi_{b0}}{kT}) \left[\exp(\frac{qV}{kT}) - 1\right] \\ &= J_{ST} \left[\exp(\frac{qV}{kT}) - 1\right] \end{aligned} \tag{25}$$

where

$$J_{ST} = A^* T^2 \exp\left(-\frac{q\Phi_{b0}}{kT}\right) \tag{26}$$

is the saturation current density in thermionic emission process.

In consideration of Schottky effect, the barrier height changes with applied bias voltage. Then $\Phi_{eff} = \Phi_{b0} - \Delta\Phi$ has to replace Φ_{b0} in Eqs. 21, 24, 25, and 26.

2.1.2.2. *Diffusion Theory.* Diffusion theory developed by Schottky[75] is based on the assumptions that the carrier energy is much larger than kT and higher than the barrier height. The theory considers the electron collisions within the depletion region. The mean free path of the carriers in the depletion region is less than the thickness of the depletion layer. So the diffusion and the drift theories of carriers are valid in the depletion region.

In the depletion region, electrons diffuse along their concentration gradient direction and drift along local electric field direction. So the electron current density is

$$\begin{aligned} J_n &= q\left[n(x)\mu_n E(x) + D_n\frac{\partial n(x)}{\partial x}\right] \\ &= qD_n\left[-\frac{qn(x)}{kT}\frac{\partial\psi(x)}{\partial x} + \frac{\partial n(x)}{\partial x}\right] \end{aligned} \tag{27}$$

where $E(x)$ is electric field, $\psi(x)$ is electric potential, μ_n is the electron mobility, $n(x)$ is electron concentration along x direction, and D_n is the diffusion constant of electron. Mobility is the proportional constant between drift velocity and local electric field at low electric field strength. The relation between the mobility and the diffusion constant of electron is

$$D_n = \frac{kT}{q}\mu_n \tag{28}$$

Hole has the similar relation of the mobility and the diffusion constant.

At steady-state condition, the current density is constant along x direction if recombination process is not included. By multiplying $exp[-q\psi(x)/kT]$ at both sides of Eq. 27 and then integrating in the depletion region. Then the right-hand side is

$$\begin{aligned} RHS &= qD_n\int_0^{x_d}\left[-\frac{qn(x)}{kT}\frac{\partial\psi(x)}{\partial x} + \frac{\partial n(x)}{\partial x}\right]\exp\left[-\frac{q\psi(x)}{kT}\right]dx \\ &= qD_n\int_0^{x_d}\frac{d\left\{n(x)\exp\left[-\frac{q\psi(x)}{kT}\right]\right\}}{dx}dx \\ &= qD_n n(x)exp\left[-\frac{q\psi(x)}{kT}\right]\Bigg|_0^{x_d} \end{aligned} \tag{29}$$

The boundary conditions are

$$\begin{aligned} \psi(0) &= 0 \\ \psi(x_d) &= \Phi_{bi} - V \\ n(0) &= N_C\exp\left(-\frac{q\Phi_{b0}}{kT}\right) \\ n(x_d) &= N_C\exp\left(-\frac{q\Phi_n}{kT}\right) \end{aligned} \tag{30}$$

where N_C is the effective density of states in conduction band. In the boundary conditions for electron density $n(x)$, Boltzmann distribution is used because the energy difference between conduction band and Fermi level is greater than several kT. Then the current density is

$$J_n = qN_C D_n \frac{\exp\left(-\frac{q\Phi_{b0}}{kT}\right)\left[\exp\left(\frac{qV}{kT}\right)-1\right]}{\int_0^{x_d}\exp\left[-\frac{q\psi(x)}{kT}\right]dx} \tag{31}$$

If we neglect Schottky effect, substitute Eq. 5 into the above equation and use Eq. 8, then we can get

$$\begin{aligned} J_n &\approx \frac{q^2 N_C D_n}{kT}\sqrt{\frac{2qN_D(\Phi_{bi}-V)}{\varepsilon_s}}\exp\left(-\frac{\Phi_{b0}}{kT}\right)\left[\exp\left(\frac{qV}{kT}\right)-1\right] \\ &= J_{SD}\left[\exp\left(\frac{qV}{kT}\right)-1\right] \end{aligned} \tag{32}$$

where

$$J_{SD} = \frac{q^2 N_C D_n}{kT}\sqrt{\frac{2qN_D(\Phi_{bi}-V)}{\varepsilon_s}}\exp\left(-\frac{q\Phi_{b0}}{kT}\right) \tag{33}$$

is the saturation current density for diffusion process. Compare Eq. 26 and Eq. 33, we can see that the saturation current density in thermionic emission process is more sensitive with temperature, while the saturation current density in diffusion process is more sensitive with applied voltage.

2.1.2.3. *Thermionic Emission-Diffusion Theory.* Crowell and Sze[76] combined Bethe's thermionic emission theory and Schottky's diffusion theory to develop a new theory for the calculation of current flow in Schottky contact. Fig. 2.7 shows the energy band diagram of Schottky contact with the consideration of Schottky effect. Fully depletion approximation between the interface to $x = x_d$ is used, which means the donors are all ionized. Because x_m is comparable to the mean free path of electrons and the potential changes too fast in the region from the metal-semiconductor interface to $x = x_m$, neither quasi-fermi level nor effective density of states is suitable to describe the electron distribution in the thin layer from $x = 0$ to $x = x_m$. In the region from $x = x_m$ to $x = x_d$, quasi-fermi level or imref $\varphi(x)$

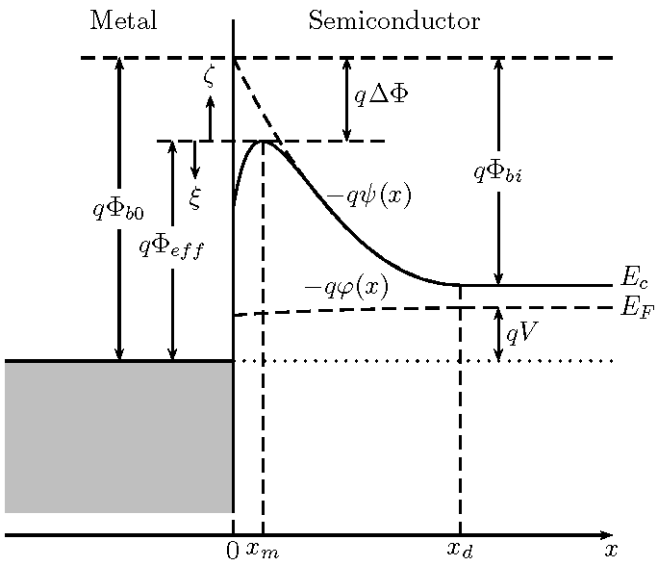

FIGURE 2.7. Band diagram of Schottky contact with Schottky effect.

can be used to find the current density. The current density is

$$J = -q\mu n(x)\frac{d\varphi(x)}{dx} \tag{34}$$

where μ is the electron mobility and $n(x)$ is the electron density

$$n(x) = N_c \exp\left\{\frac{q}{kT}\left[\psi(x) - \varphi(x)\right]\right\} \tag{35}$$

where $\psi(x)$ is the electron potential, N_c is the effective density of states in the conduction band. Then we can integrate Eq. 34 with $n(x)$ from Eq. 35 from x_m to x_d. Now we get

$$\exp\left[-\frac{q\varphi(x_m)}{kT}\right] - \exp\left[\frac{qV}{kT}\right] = -\frac{J}{\mu N_c kT}\int_{x_m}^{x_d} \exp\left[-\frac{q\psi(x)}{kT}\right] dx \tag{36}$$

with the boundary condition

$$\varphi(x_d) = -V \tag{37}$$

where V is the applied bias voltage.

Suppose the narrow layer in between $x = 0$ and x_m is a sink of electrons, the current density is

$$J = q(n_m - n_0)v_r \tag{38}$$

where v_r is the effective recombination velocity at maximum potential energy, n_m is the electron density at x_m when there is current flow and n_0 is the electron density at x_m at quasi-equilibrium condition. At quasi-equilibrium condition, the position and the magnitude of the highest electron potential don't change during the procedure to reach equilibrium. If Fermi level in metal is used as energy reference, then

$$\begin{aligned} n_0 &= N_c \exp(-\frac{q\phi_{eff}}{kT}) \\ n_m &= N_c \exp\left\{\frac{q}{kT}\left[-\varphi(x_m) - \phi_{eff}\right]\right\} \end{aligned} \tag{39}$$

Then we can get

$$J = \frac{qN_c v_r}{1 + v_r/v_d} \exp\left(-\frac{q\Phi_{eff}}{kT}\right)\left[\exp\left(\frac{qV}{kT}\right) - 1\right] \tag{40}$$

where

$$v_d = \left\{\frac{q}{\mu kT}\int_{x_m}^{x_d} \exp\left[-\frac{q}{kT}\left(\psi(x) + \phi_{eff}\right)\right] dx\right\}^{-1} \tag{41}$$

is the effective diffusion velocity for the electrons transport from x_d to x_m.

Suppose Maxwellian distribution can be used for electrons at the $x \geq x_m$ region, and only thermionic emitted electrons flow from metal to the $x \geq x_m$ region. Then

$$v_r = \frac{\int_0^\infty v_x \exp(-m^* v_x^2/2kT) dv_x}{\int_{-\infty}^\infty \exp(-m^* v_x^2/2kT) dv_x} = \sqrt{\frac{kT}{2m^*\pi}} = \frac{A^* T^2}{qN_c} \tag{42}$$

where A^* is the effective Richardson constant, $N_c = 2(\frac{2\pi m^* kT}{h^2})^{3/2}$[73] is the density of states in conduction band. If $v_d \gg v_r$, then

$$\frac{v_r}{1 + v_r/v_d} \to v_r$$

So the thermionic emission theory can be applied. If $v_d \ll v_r$, then

$$\frac{v_r}{1 + v_r/v_d} \to v_d$$

So the diffusion theory can be applied.

The electron potential can be replaced with

$$\psi = \phi_{eff} + \Delta\Phi - Ex - \frac{q}{16\pi\varepsilon_s x} \tag{43}$$

in Eq. 40 in consideration of Schottky effect in the current density.

In the thermionic emission process that is described by recombination velocity v_r, the electrons has a probability, f_p, to be reflected back by electron optical-phonon scattering even the electrons already pass the highest potential energy[77, 78]. The Maxwellian distribution of electrons can also be changed because the electrons are quantum-mechanically reflected by Schottky barrier and the electrons tunnel through Schottky barrier[79, 80]. By considering the quantum-mechanical reflection and tunneling effects, we define f_Q as the ratio of current densities with the consideration of the effects and without the consideration of the effects. The ratio f_Q depends on the electric field and the energy difference between electron and the potential maximum $\psi(x_m)$. Then the current density changes to

$$J = J_s[\exp(\frac{qV}{kT}) - 1] \tag{44}$$

with

$$J_s = A^{**}T^2 \exp(-\frac{q\phi_{eff}}{kT}) \tag{45}$$

$$A^{**} = \frac{f_p f_Q A^*}{1 + f_p f_Q v_r / v_d} \tag{46}$$

The effective Richardson constants for electrons and holes are almost constant in the range from about $10^4 V/cm$ to about $10^5 V/cm$ for metal-Si contact[81]. The value for holes is smaller than that of electrons. The quasi-Fermi level, or imref is almost flat in the whole depletion layer[82].

2.1.2.4. *Tunneling Current.* Tunneling current may be dominant if the semiconductor is heavily doped or works at low temperature. The current density from semiconductor to metal[79, 73]

$$J_{sm} = \frac{A^* T}{k} \int_0^{q(\Phi_{b0} - \Delta\Phi)} F_s T(\eta)(1 - F_m) d\eta \tag{47}$$

where η is potential energy measured from Φ_{eff} downward, as shown in Fig. 2.7. F_s and F_m are the Fermi distribution of carriers in semiconductor and metal, respectively. $T(\eta)$ is the carriers transmission coefficient below Φ_{eff} through the barrier.

Similarly, the current density from metal to semiconductor is

$$J_{ms} = -\frac{A^* T}{k} \int_0^{q(\Phi_{b0}-\Delta\Phi)} F_m T(\eta)(1-F_s) d\eta \tag{48}$$

The total tunneling current density is the summation of Eq. 47 and Eq. 48.

If the tunneling current flow is the dominate process, the transmission can be approximated as[83]

$$T(\eta) \sim \exp(-\frac{q\Phi_{eff}}{E_{00}}) \tag{49}$$

where

$$E_{00} = \frac{q\hbar}{2}\sqrt{\frac{N_D}{\varepsilon_s m^*}}$$

N_D is the donor concentration. Then the tunneling current density

$$J_t \sim \exp(-\frac{q\Phi_{eff}}{E_{00}}) \tag{50}$$

So the tunneling current density increases with donor concentration.

2.1.2.5. *Minority Carrier Current Density.* At low injection condition, current density is due to majority carrier transport. As the forward bias voltage increases high enough, the ratio, γ, of current density due to minority carrier to total current density is increasing because of carrier drift.

The continuity and the current density equations are

$$\frac{1}{q}\frac{\partial J_p}{\partial x} + \frac{p_n - p_{n0}}{\tau_p} = 0 \tag{51}$$

$$q\mu_p p_n E - qD_p \frac{\partial p_n}{\partial x} = J_p \tag{52}$$

where μ_p is the hole mobility, J_p is hole current density, p_n is the minority (hole) concentration in n-type semiconductor, and p_{n0} is the hole concentration in thermal equilibrium condition. The solution of the equations depends on the device structure.

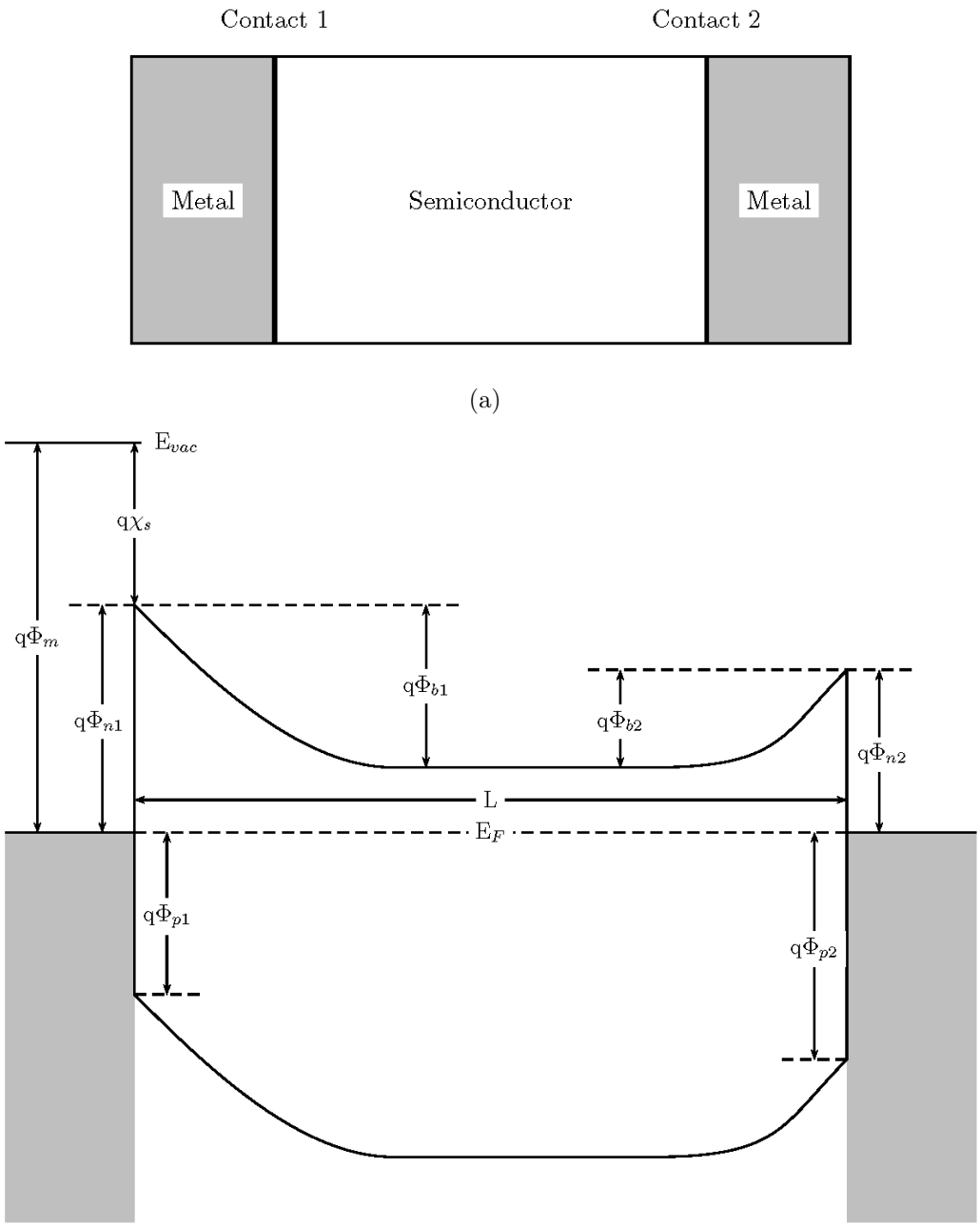

FIGURE 2.8. (a) Schematic of a simplified metal-semiconductor-metal structure. (b) Energy diagram of the simplified MSM structure.

2.2. Metal-Semiconductor-Metal Structure

The metal-semiconductor-metal (MSM) structures have two terminals with one piece of semiconductor sandwiched in between two pieces of metal, as shown in Fig. 8(a). The two

contacts at both sides of the semiconductor can be named as 1 and 2. Suppose the semiconductor is n-type and the device is symmetric. Fig. 8(b) shows the energy band diagram of the MSM structure with ideal, intimate and abrupt contacts at thermal equilibrium.

In the figure, L is the thickness of semiconductor slice. Φ_{n1} and Φ_{n2} are the potential barrier heights for electrons at contacts 1 and 2, respectively. Φ_{b1} and Φ_{b2} are the built-in potential for electrons at two contacts. Φ_{p1} and Φ_{p2} are the potential barrier heights for holes at two contacts. If the barrier heights $\Phi_{n1} = \Phi_{n2}$ and the two contacts have same size, the MSM structure is symmetric.

The MSM structure actually is two back-to-back aligned Schottky contacts. Suppose bias voltage is applied to two contacts with positive to the metal of contact 2 and negative to the metal of contact 1. Then contact 1 is revers biased and contact 2 is forward biased. As the applied bias voltage increases, the total depletion layer thickness of both contact also increases. The total thickness is L when the applied voltage is reach-through voltage V_{rt}, as shown in Fig. 9(a). This figure also shows the electric field within semiconductor. Fig. 9(b) shows the energy diagram. At reach-through voltage V_{rt}, we can get the relation from Eq. 8 and Fig. 9(a)

$$\sqrt{\frac{2\varepsilon_s}{qN_D}(\Phi_{b1} + V_1)} + \sqrt{\frac{2\varepsilon_s}{qN_D}(\Phi_{b2} - V_2)} = L \tag{53}$$

Then,

$$V_{rt} = V_1 + V_2 = \frac{qN_D}{2\varepsilon_s}L^2 - (\Phi_{b1} - \Phi_{b2}) - L\sqrt{\frac{2qN_D}{\varepsilon_s}(\Phi_{b2} - V_2)} \tag{54}$$

As the applied bias voltage increases even higher, the thickness of the depletion layer at contact 2 is getting smaller according to Eq. 7. Finally, the thickness of the depletion layer is zero and the electric field is zero at contact 2, as shown in Fig. 10(a). Then the potential energy at contact 2 doesn't change, that means the curve of the potential energy is flat, as shown in Fig. 10(b). The bias voltage under this condition is called flat-band voltage. From Eq. 8

$$x_{d1} = L \;\; = \;\; \sqrt{\frac{2\varepsilon_s}{qN_D}(\Phi_{b1} + V_1)}$$

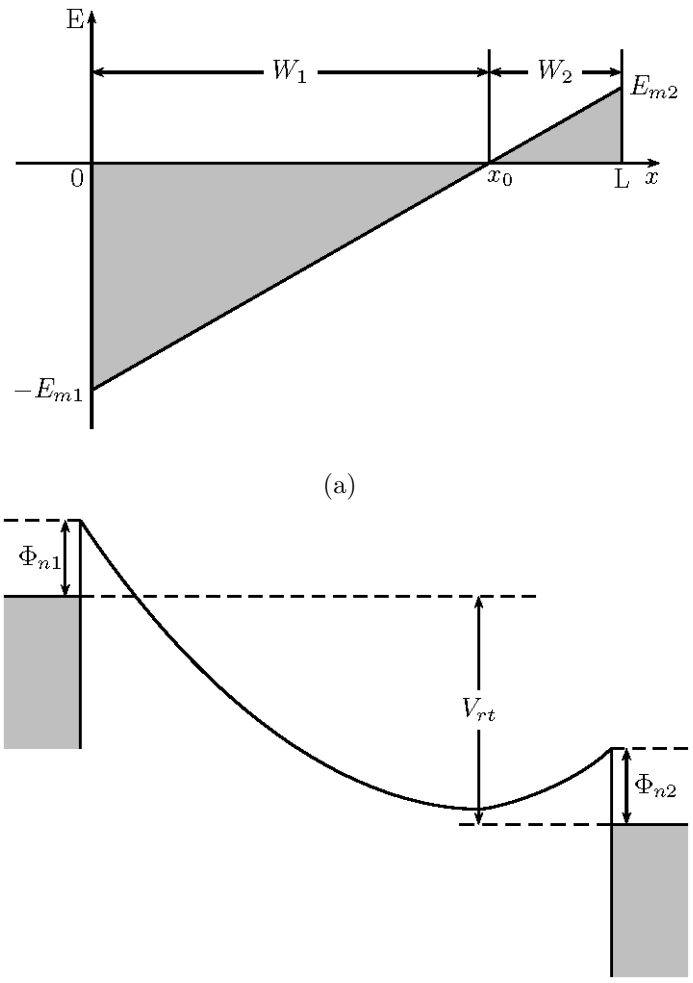

FIGURE 2.9. At reach-through bias voltage, V_{rt}, (a) Electric field within semiconductor and the depletion regions. (b) Energy diagram of the structure.

$$x_{d2} = 0 \quad = \quad \sqrt{\frac{2\varepsilon_s}{qN_D}(\Phi_{b2} - V_2)} \tag{55}$$

Then, we can get

$$V_{fb} = V_1 + V_2 = \frac{qN_D}{2\varepsilon_s}L^2 - (\Phi_{b1} - \Phi_{b2}) = \frac{qN_D}{2\varepsilon_s}L^2 - \Delta\Phi_b \tag{56}$$

where $\Delta\Phi_b = \Phi_{b1} - \Phi_{b2}$ is the difference of build-in potential at both contacts. Now Eq. 54 can be written as

$$V_{rt} = V_{fb} - \sqrt{4(V_{fb} + \Delta\Phi_b)(\Phi_{b2} - V_2)} \tag{57}$$

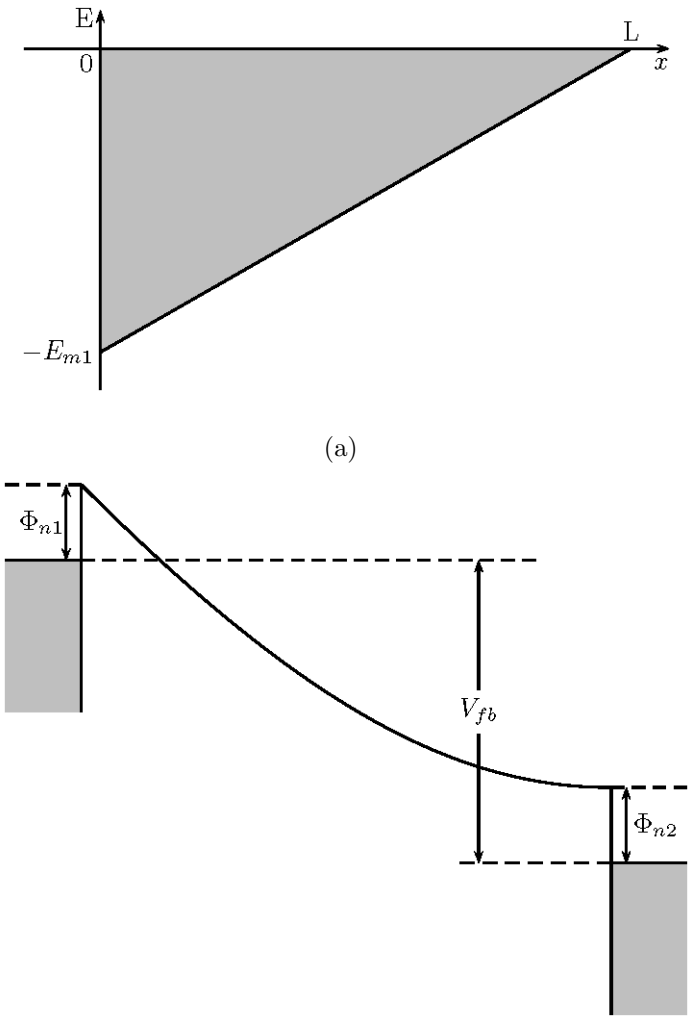

FIGURE 2.10. At flat-band bias voltage, V_{fb}, (a) Electric field within semiconductor and the depletion region. (b) Energy diagram of the structure.

If the applied bias voltage keeps increasing, the band bends even lower, as shown in Fig. 11(b). The electric fields at the two contacts are also increasing, as shown in Fig. 11(a), until the device is breakdown due to the high electric field at reverse-biased contact.

2.2.1. *Electron Current Transport*

According to the applied voltage, the reach-through voltage, and the flat-band voltage, the whole current-voltage curve can be divided into three regions: (1) $V < V_{rt}$, (2) $V_{rt} \leq$

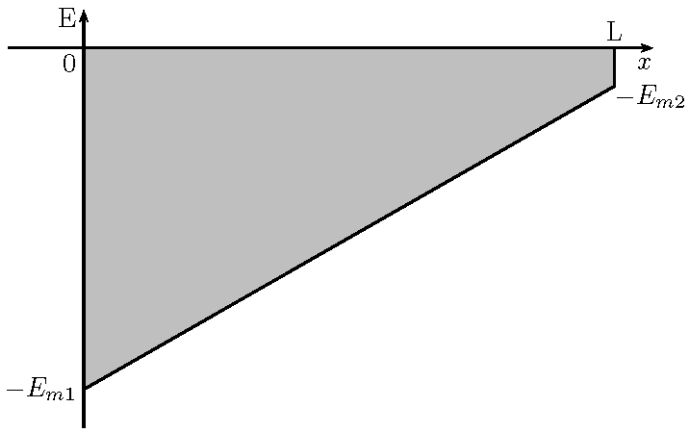

(a)

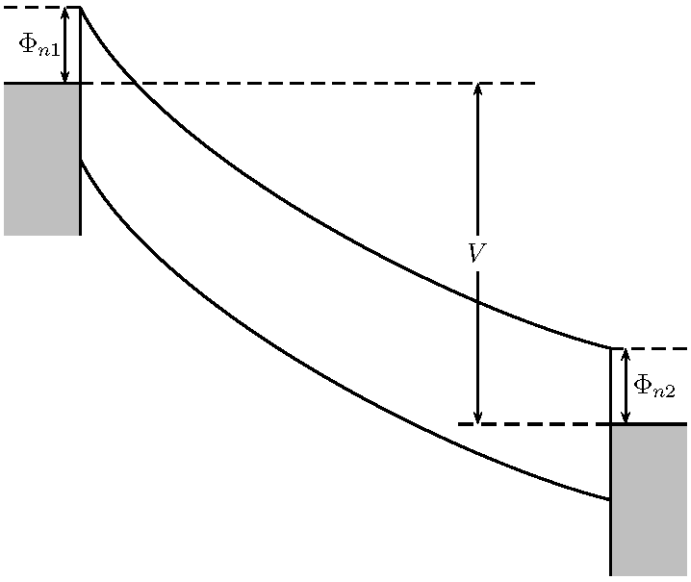

(b)

FIGURE 2.11. When the applied bias voltage is great than V_{fb}, (a) Electric field within semiconductor. (b) Energy diagram of the structure.

$V < V_{fb}$, (3) $V \geq V_{fb}$, and (4) the applied voltage above breakdown voltage. We will discuss the first three regions separately except for the last case.

2.2.1.1. *Small Applied Voltage Region* $V < V_{rt}$. Suppose the applied voltages over contact 1 and 2 are V_1 and V_2 (Fig. 2.12), respectively. Then

$$V = V_1 + V_2 \tag{58}$$

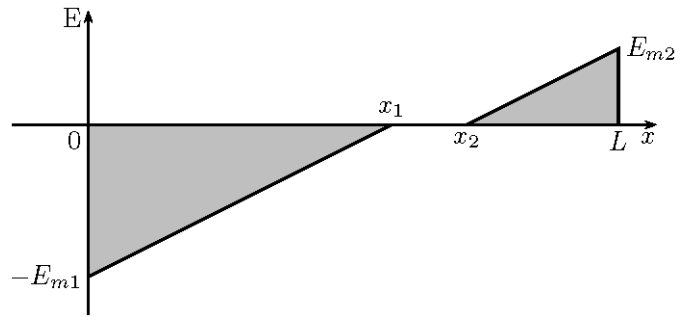

(a)

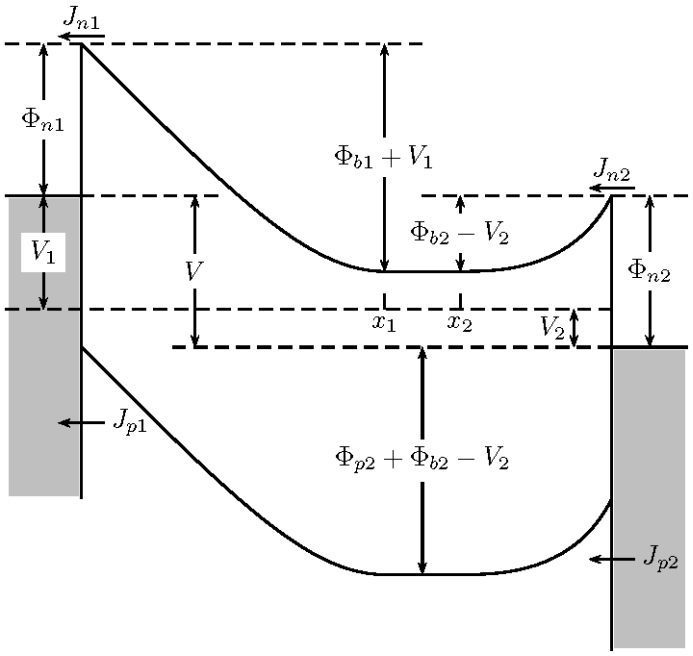

(b)

FIGURE 2.12. At small voltage $V < V_{rt}$, (a) Electric field and (b) Energy diagram of the structure.

Because of the restriction of current continuity, the currents due to majority carrier are equal at both contacts, that is

$$J_{n1} = J_{n2} \tag{59}$$

From Eq. 44 and 45 with applied voltage $V = -V_1$ for contact 1, the current density magnitude with reverse bias is

$$\begin{aligned} J_{n1} &= A^{**}T^2 \exp\left(-\frac{q\Phi_{eff}}{kT}\right)\left[\exp\left(-\frac{qV_1}{kT}\right) - 1\right] \\ &= A^{**}T^2 \exp\left(-\frac{q\Phi_{n1}}{kT}\right)\exp\left(\frac{q\Delta\Phi_{n1}}{kT}\right)\left[1 - \exp\left(-\frac{qV_1}{kT}\right)\right] \end{aligned} \tag{60}$$

with the consideration of Schottky effect. In additional to image effect, the barrier height is also changed due to the penetration of electron wave function into semiconductor band gap[81]. A static dipole layer is induced at the metal-semiconductor interface. Then the barrier height varies slowly with the electric field. To a first approximation, the barrier height change is[81]

$$(\Delta\Phi)_{static} \approx \alpha_1 E_{max} \tag{61}$$

where $\alpha_1 = \dfrac{\partial\phi_{n1}}{\partial E_{max}}$ is the coefficient. From Eq. 15 and Fig. 8(b), the maximum electric fields at two contacts are

$$\begin{aligned} E_{max1} &= \sqrt{\frac{2qN_D}{\varepsilon_s}(V_{b1} + V_1)} \\ E_{max2} &= \sqrt{\frac{2qN_D}{\varepsilon_s}(V_{b2} - V_2)} \end{aligned} \tag{62}$$

if we neglect the term kT/q when the term is relative small compared with the applied voltage and the build-in potentials. Then Eq. 60 changes to[81, 84]

$$J_{n1} = A_n^{**}T^2 \exp\left(-\frac{q\Phi_{n1}}{kT}\right)\exp\left[\frac{q}{kT}(\Delta\Phi_{n1} + \alpha_1 E_{max1})\right]\left[1 - \exp\left(-\frac{qV_1}{kT}\right)\right] \tag{63}$$

And the forward current density change to

$$J_{n2} = A_n^{**}T^2 \exp\left(-\frac{q\phi_{n2}}{kT}\right)\exp\left[\frac{q}{kT}(\Delta\Phi_{n2} + \alpha_2 E_{max2})\right]\left[\exp\left(\frac{qV_2}{kT}\right) - 1\right] \tag{64}$$

From Eqs. 59, 63, and 64, we get

$$(\Delta\Phi_{n1} - \Delta\Phi_{n2}) + (\alpha_1 E_{max1} - \alpha_2 E_{max2}) - (\Phi_{n1} - \Phi_{n2}) = \frac{kT}{q}\ln\left[\frac{\exp\left(\frac{qV_2}{kT}\right) - 1}{1 - \exp\left(-\frac{qV_1}{kT}\right)}\right] \tag{65}$$

The current-voltage relation could be solved numerically from Eqs. 62 and 65.

2.2.1.2. $V_{rt} \leq V < V_{fb}$. In this region, the total thickness of the depletion layers is equal to the thickness of the semiconductor. From Eqs. 8, 15, and 56, the maximum electric fields at both contacts are

$$\begin{aligned} E_{max1} &= \frac{V + V_{fb} + 2\Delta\Phi_b}{L} \\ E_{max2} &= \frac{|V - V_{fb}|}{L} \end{aligned} \tag{66}$$

and the applied voltages at the two contacts are

$$\begin{aligned} V_1 + \Phi_{b1} &= \frac{(V + V_{fb} + 2\Delta\Phi_b)^2}{4(V_{fb} + \Delta\Phi_b)} \\ \Phi_{b2} - V_2 &= \frac{(V_{fb} - V)^2}{4(V_{fb} + \Delta\Phi_b)} \end{aligned} \tag{67}$$

As the applied voltage increases, the barrier height of reverse-biased contact increases and the other one decreases. The current density of electrons is restricted by that of the reverse-biased contact and the same as Eq. 63.

2.2.1.3. $V \geq V_{fb}$. As the applied voltage increases above the flat-band voltage, the electron current density can be gotten from Eq. 63 and Eq. 66 must be used to find the maximum electric field at both contacts. As the applied voltage keeps increasing, finally the reverse-biased contact will be breakdown because the electric field is stronger at the contact 1 than that at the contact 2.

2.2.2. *Hole Current Transport*

The holes are from the thermionic-emission of contact 2. The potential barrier for holes at the contact 2 is $\Phi_{p2} + \Phi_{b2} - V_2$, as shown in Fig. 12(b). When the applied voltage is less than the reach-through voltage V_{rt}, hole current is the diffusion transport from the depletion layer edge, x_2, of the contact 2 to the depletion layer edge, x_1, of the contact 1. We can substitute the following relations into Eq. 51

$$J_p = -qD_p \frac{\partial p_n(x)}{\partial x} \tag{68}$$

$$D_p = \frac{kT}{q}\mu_p \tag{69}$$

Now we get

$$\frac{\partial^2 p_n(x)}{\partial x^2} - \frac{p_n(x) - p_{n0}}{D_p \tau_p} = 0 \tag{70}$$

The general solution is

$$p_n(x) - p_{n0} = A \exp\left(\frac{x}{L_p}\right) + B \exp\left(-\frac{x}{L_p}\right) \tag{71}$$

where $L_p = \sqrt{D_p \tau_p}$ is the diffusion length. The boundary conditions are

$$\begin{aligned} p_n(x_1) &= p_{n0} \exp\left(-\frac{qV_1}{kT}\right) \\ p_n(x_2) &= A_p^* T^2 \exp\left[-\frac{q}{kT}(\phi_{p2} + \phi_{b2} - V_2)\right] \end{aligned} \tag{72}$$

where A^* is the effective Richardson constant of holes. Then the hole current density is[84]

$$\begin{aligned} J_{p1} &= qD_p \frac{dp_n(x)}{dx}\Big|_{x_1} = \frac{qD_p p_{n0}}{L_p} \tanh\left(\frac{x_2 - x_1}{L_p}\right)\left[1 - \exp\left(-\frac{qV_1}{kT}\right)\right] \\ &+ \frac{A_p^* T^2 \exp\left[-\dfrac{q(\Phi_{p2} + \Phi_{b2})}{kT}\right]}{\cosh\left(\dfrac{x_2 - x_1}{L_p}\right)}\left[\exp\left(\frac{qV_2}{kT}\right) - 1\right] \end{aligned} \tag{73}$$

with the condition that $J_{p1} = 0$ when the applied voltage is 0. If the applied voltage increase over the reach-through voltage V_{rt}, the thickness of the neutral region reduces to zero. Then the above equation still can be used with $x_2 - x_1 = 0$

$$J_{p1} = A_p^* T^2 \exp\left[-\frac{q(\Phi_{p2} + \Phi_{b2})}{kT}\right]\left[\exp\left(\frac{qV_2}{kT}\right) - 1\right] \tag{74}$$

Substitute Eq. 67 into the above equation, we can get

$$J_{p1} = A_p^* T^2 \exp\left(-\frac{q\Phi_{p2}}{kT}\right)\left[\exp\left(-\frac{q(V_{fb} - V)^2}{4kT(V_{fb} + \Delta\Phi_b)}\right) - \exp\left(-\frac{q\Phi_{b2}}{kT}\right)\right] \tag{75}$$

Here $V_{rt} \leq V < V_{fb}$. At $V = V_{fb}$, the above equation changes to

$$J_{p1} = A_p^* T^2 \exp\left(-\frac{q\Phi_{p2}}{kT}\right) \tag{76}$$

If the applied voltage keeps increasing above the flat-band voltage V_{fb}, the barrier lowering effect at contact 2 must be included. Now the hole current density is[84]

$$J_{p1} = A_P^* T^2 \exp\left(-\frac{q\Phi_{p2}}{kT}\right) \exp\left(\frac{q\Delta\Phi_{p2}}{kT}\right) \tag{77}$$

with $V > V_{fb}$ and

$$\Delta\Phi_{p2} = \sqrt{\frac{qE_{max2}}{4\hbar\varepsilon_s}} = \sqrt{\frac{q(V - V_{fb})}{4\hbar\varepsilon_s L}} \tag{78}$$

2.2.3. *Total Current Transport*

The total current density is the summation of current density of holes and electrons. We define the following quantities for the following parts.

$J_{ns} = A_n^* T^2 \exp\left(-\frac{q\Phi_{n1}}{kT}\right)$ is the electron saturation current density.

$J_{ps} = A_p^* T^2 \exp\left(-\frac{q\Phi_{p2}}{kT}\right)$ is the hole saturation current density.

According to the applied voltage, there are three different regions of current density.

2.2.3.1. $V < V_{rt}$. Add Eq. 60 and 73, we get

$$\begin{aligned} J = J_{n1} + J_{p1} &= J_{ns} \exp\left(\frac{q\Delta\Phi_{n1}}{kT}\right)\left[1 - \exp\left(-\frac{qV_1}{kT}\right)\right] \\ &\quad + \frac{qD_p p_{n0}}{L_p} \tanh\left(\frac{x_2 - x_1}{L_p}\right)\left[1 - \exp\left(-\frac{qV_1}{kT}\right)\right] \\ &\quad + \frac{J_{ps}}{\cosh\left(\frac{x_2 - x_1}{L_p}\right)} \exp\left(-\frac{q\Phi_{b2}}{kT}\right)\left[\exp\left(\frac{qV_2}{kT}\right) - 1\right] \end{aligned} \tag{79}$$

2.2.3.2. $V_{rt} < V < V_{fb}$. Add Eq. 60 and 75, then

$$\begin{aligned} J &= J_{ns} \exp\left(\frac{q\Delta\Phi_{n1}}{kT}\right)\left[1 - \exp\left(-\frac{qV_1}{kT}\right)\right] \\ &\quad + J_{ps}\left[\exp\left(-\frac{q(V_{fb} - V)^2}{4kT(V_{fb} + \Delta\Phi_b)}\right) - \exp\left(-\frac{q\Phi_{b2}}{kT}\right)\right] \\ &\approx J_{ns} \exp\left(\frac{q\Delta\Phi_{n1}}{kT}\right) + J_{ps}\left[\exp\left(-\frac{q(V_{fb} - V)^2}{4kT(V_{fb} + \Delta\Phi_b)}\right) - \exp\left(-\frac{q\Phi_{b2}}{kT}\right)\right] \end{aligned} \tag{80}$$

if $V_1 \gg \frac{kT}{q}$.

2.2.3.3. $V > V_{fb}$. Add Eq. 60 and 77 with the condition $V_1 \gg \frac{kT}{q}$, then

$$J = J_{ns} \exp\left(\frac{q\Delta\Phi_{n1}}{kT}\right) + J_{ps} \exp\left(\frac{q\Delta\Phi_{p2}}{kT}\right) \tag{81}$$

From the above analysis, we can see that the metal-semiconductor-metal structure differs from single Schottky contacts. Current flow in MSM structures is due to the transport of both electrons and holes, but the current flow in Schottky contacts is mainly due to the transport of majority carriers. Current-voltage curve of Schottky contacts is not symmetric, that means it has rectifying effect. The current-voltage curve of MSM structures is symmetric and does not have rectifying effect if the structure is symmetric. If the structure is not symmetric, like different barrier heights or different sizes of two contacts, the current-voltage curve can be asymmetric and has certain degree of rectifying effect. Because the total current density has electron and hole parts in MSM structure, it is possible that the current flow is dominated by either electron or hole carrier transport depending on the barrier height of the contacts. If the electron current density dominates, the second terms in the Eq. 79, 80, and 81 can be neglected. As the applied voltage is greater than the reach-through voltage, the current density increases slowly with the applied voltage because it is proportional to $\exp(V^{1/2})$. The current density changes relative faster with the applied voltage as $V < V_{rt}$ because of the term $[1 - \exp(-qV_1/kT)]$. If the hole transport dominates, the current density increases slowly as $V < V_{rt}$, then very fast till $V = V_{fb}$, and finally slow down again. Because the electron current density is restricted by reverse-biased contact, the hole current density can be much larger than the electron current density at high bias voltage even if the barrier of holes is higher than that of electrons.

CHAPTER 3

CURRENT-VOLTAGE CHARACTERISTICS OF GALLIUM NITRIDE/DEOXYGUANOSINE BASED PHOTODETECTOR

3.1. Background of Electronic Devices Based on Modified Deoxyguanosine

DNA molecules have self-assembly and self-recognition properties. The combination of those properties of DNA and modern nano-fabrication technology stimulated researches on the physical mechanism of conductivity. DNA based field effect transistor (FET)[11], diode[85], and photodetector[65] have already fabricated. Among DNA bases, guanosine has the lowest oxidation energy which favors charge transfer[61].

Guanosine derivatives have been successfully self-assembled on solid-state surface like mica[86] and silicon[65, 63]. But the process on polar GaN surface is still not investigated. GaN surface is polar because of its noncentrosymmetric wurtzite lattice structure and large strain polarization field due to the absence of native substrate for epitaxial growth[35]. The surface can be terminated by gallium or nitrogen layer to form positive or negative polarity. The surface polarity may influence the self-assembling process of guanosine derivatives.

UV photodetectors have potential applications in sciences and industries. But many of the commercially available detectors based on silicon (Si) have several drawbacks due to its narrow bandgap. First, the photodetectors usually have to work at low-temperature because they have large dark current at room temperature. Second, silicon is not so sensitive in ultraviolet(UV) region as in visible and infrared regions[87]. Third, the efficiency of the photodetectors is even reduced because external filters are used to block visible light. On the other hand, wide bandgap materials, like gallium nitride (GaN), have lower dark current at room temperature so that the devices based on such materials can work in UV region

at room or even high temperatures[87]. Those devices based on GaN can work in harsh conditions because of its hardness and resistance to chemicals.

Rinaldi, et al., modified guanosine molecules to tune the conductivity. They also studied the effects of different solvents to change the self-assembly length of guanosine molecules in order to get to the optical lithography scale[88]. As the concentration of modified deoxyguanosine derivatives (3′, 5′-di-O-decanoyl-2′-deoxyguanosine, $dG(C_{10})_2$) in chloroform ($CHCl_3$) is in between 0.01 to 0.04M, two-dimensional ribbon-like structure self-assembled on SiO_2 surface. Otherwise, deoxyguanosine molecules only form disordered structure[63]. Checked with atomic force microscopy (AFM) measurements, the length of ribbon-like structure is found typically around 100nm[63]. Within this length scale, ribbons aligned to form crystal structure. Above this length scale, only randomly ensemble of ribbon formed just like in polycrystalline. They fabricated bow-tie shaped electrode structure by electron beam lithography (EBL), as shown in Fig. 3.1, and investigated the conductivity of self-assembled deoxyguanosine by current-voltage(I-V) characterization with deoxyguanosine molecules bridging the two metal electrodes[65, 63, 88]. The I-V curves show strong dependence on the distance between two electrodes. First, when the distance is about 800nm, the curve is symmetric nonohmic and has the characteristic of hysteresis loop for upward-downward voltage sweeps. Then, the distance is narrowed to about 120nm, the curve is nonlinear. The current is zero when the voltage is in between -2V and 2V. Then the current increases to sub-μA as the bias voltage increases. The hysteresis effect is very weak. Finally, when the distance is further reduced to 60nm, the I-V curve changes to asymmetric and shows rectifying characteristic. The current reaches up to the order of μA with positive bias voltage to 10V, while the current is only in the order of nA with negative bias voltage. In the first case, the device characteristic is similar to that of metal-dielectric-metal structure. The device has the properties of metal-semiconductor-metal structure in the last case because it shows clear diode characteristic[63]. The photocurrent measurements show that the bandgap

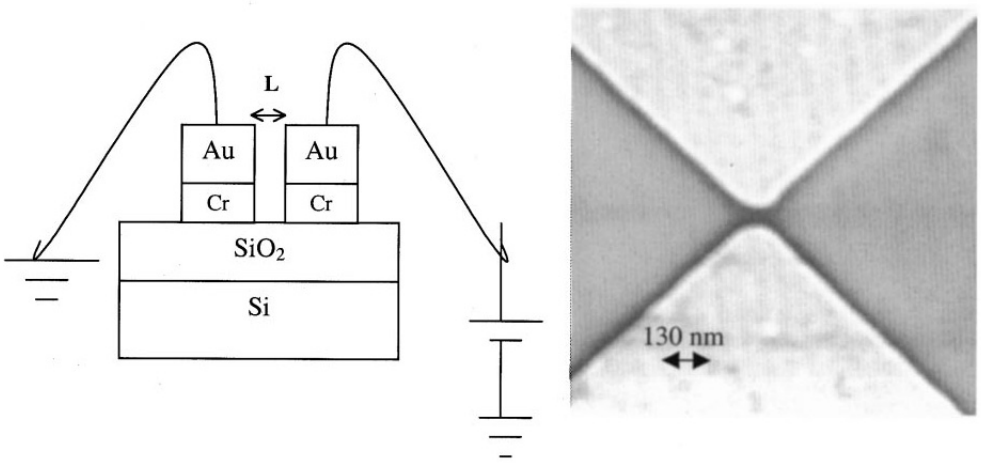

FIGURE 3.1. Left image is the schematic of the bow-tie structure. Right image is an SEM image of the gold nanoelectrodes fabricated by EBL and lift-off onto a SiO_2/Si substrate. Reprinted with permission from R. Rinaldi, et. al., *Appl. Phys. Lett.*, 78, 3541 (2001). ©2001 American Institute of Physics

of the self-assembled guanosine structure is about 3.4eV[65, 63], which is very close to that of GaN.

3.2. Experiments

3.2.1. *Modified Deoxyguanosine Derivative Synthesis*

The synthesis of deoxyguanosine derivative (DG) follows the protocol of Gottarelli, et al.[89] The molecular weight of the deoxyguanosine derivative is 575.74. The modified deoxyguanosine derivatives (3′, 5′-di-O-decanoyl-2′-deoxyguanosine, $dG(C_{10})_2$) powder is dissolved in chloroform ($CHCl_3$) solution with concentration 3.3×10^{-2} M.

3.2.2. *Atomic Force Microscopy Characterization*

Atomic Force Microscopy(AFM) is widely used to measure surface features with atom size resolution. As it raster scans the sample surface, AFM keeps the force constant between its probe and the sample surface. The sharp probe is attached to a cantilever. The probe position is monitored by a light beam that incidents on the cantilever and is reflected to a

light sensor. As the distance between the probe and the sample surface changes, the force also changes and the reflected beam position changes accordingly. The feedback system of AFM sends signal to a piezoelectric transducer to adjust the probe position in perpendicular direction to the sample surface through the cantilever. Then the force goes back to its original level. The in-plane resolution depends on the sharpness of the probe used to image the sample surface. The vertical resolution depends on the relative vibration of the probe. By reducing the vibration from environment, the vertical resolution can be improved. AFM has two operation mode: deflection (contact) mode and vibration (non-contact) mode. In deflection mode, the roughness of the sample surface is directly recorded through the deflection motion of the probe as it is trying to keep the force constant. In the vibration mode, the cantilever is vibrated with a frequency at or close to its resonant frequency. Vibration mode can be operated with frequency modulation and amplitude modulation. With frequency modulation, the vibration frequency change is recorded as the distance changes. With amplitude modulation, the amplitude and the phase of the vibration is recorded as the distance changes. The phase change of the vibration is different for different material surface.

GaN substrates with Ga- and N-polarity were measured by atomic force microscopy with contact mode and 0^o scan angle. The solution was spin-coated on GaN substrates by dropping 10μL solution with 4000RPM speed and 30sec duration. The spin-coated samples were measured by AFM also with contact mode and 0^0 scan angle. Then the qualities of samples with different substrate surface polarities were compared.

3.2.3. *Nano-Electrodes Fabrication*

It is very crucial to select metal electrode for future electrical characterization. The Fermi level of metal should be close to HOMO or LUMO states of SADG so that the potential barrier height between two material is low. Here HOMO is highest occupied molecular orbitals and LUMO is lowest unoccupied molecular orbitals. Fig. 3.2 shows some metals' work function and the energy level of DNA bases. The guanosine molecules were modified

to tailor its energy levels so that the Fermi level of SADG can be close to the work function of one metal[88].

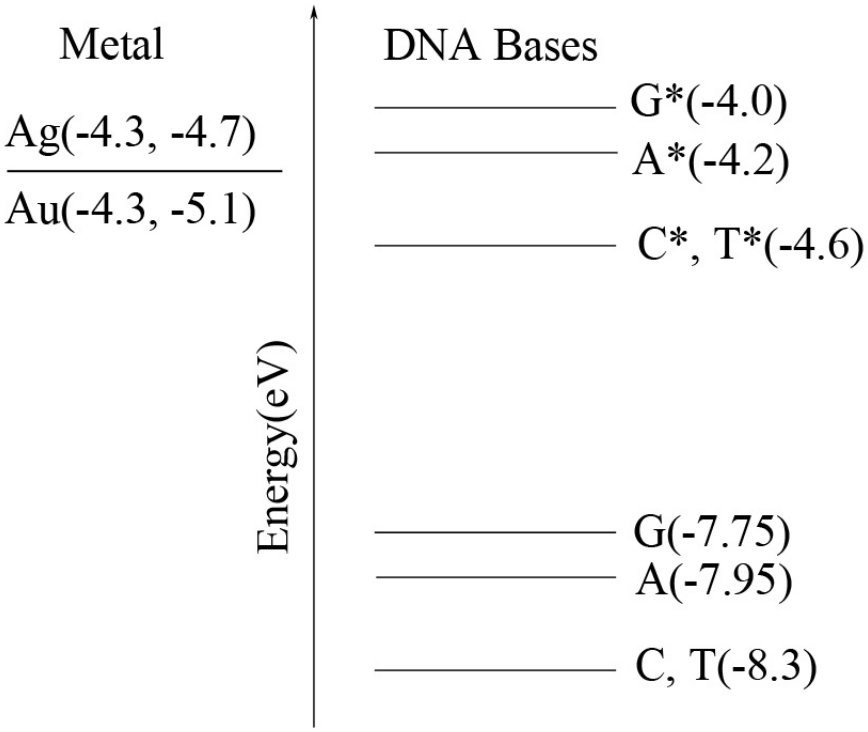

FIGURE 3.2. Schematics of work functions of gold and silver and energy levels of DNA bases. The values of metal work functions are taken from Hodgman and Veazey[90], Ashcroft and Mermin[91], and Barrow[92]. The energy level of guanine are from Sugiyama and Saito[93] and Wetmore[94]. The values of the other DNA bases adenine (A), thymine (T), and cytosine (C) were deduced from yield data of charge transfer between DNA bases[95]. The energy difference between π-π^* of single base is 3.75eV[42].

GaN substrates that have better DG film quality were used to fabricate nano-electrodes. The schematic of nano-electrodes structure is shown in Fig. 3.3(a). First, the substrates were passivated with silicon nitride (Si_3N_4). The electrodes must be wire-bonded with wire that is connected to power source and meters to form a close circuit for current-voltage and photocurrent measurements. The smallest wire used in wire-bonder is about 15μm

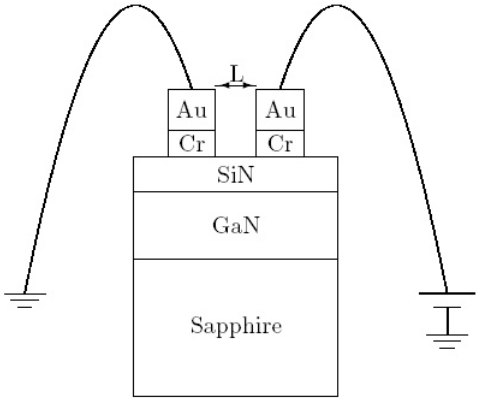

(a)

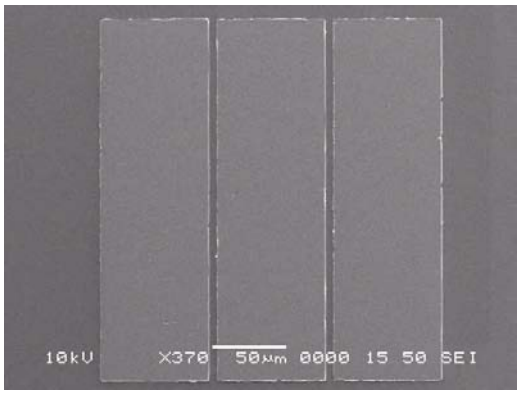

(b)

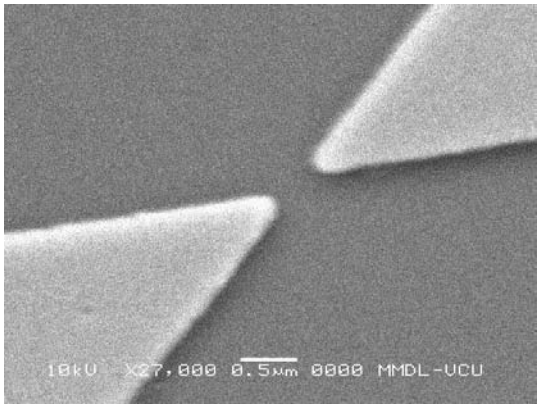

(c)

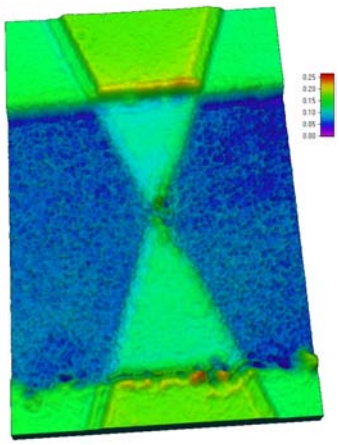

(d)

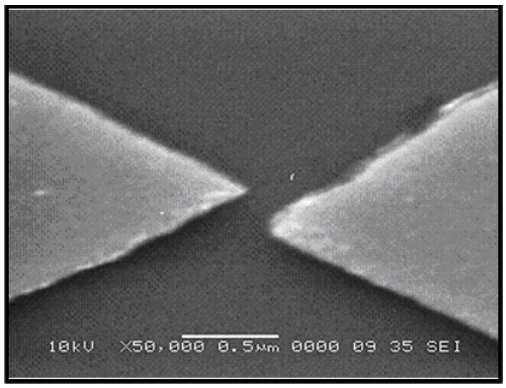

(e)

FIGURE 3.3. (a)Schematic of nano-electrodes, (b)SEM image of metal pad, (c) SEM image of one pair of electrodes, (d) Confocal image of one pair of electrodes, and (e) Mis-aligned nano-electrodes.

in diameter. It is much larger than the size of nano-electrodes which is in less than 1μm scale. Meatal pads which are bigger than the wire must be fabricated first for wire-bonding. Because the size of metal pads, as shown in Fig. 3.3(b), is too big for EBL fabrication, it will take too long machine time. So the metal pads were deposited in vacuum evaporator with masks. The thicknesses of chromium and gold are 8nm and 30nm, respectively. The size of metal pads is about 200μm$\times$80μm. The distance between two adjacent pads is 5μm. Then electrodes with bow-tie shape (Fig. 3.3(c)) were fabricated by EBL in between two metal pads. The confocal image Fig. 3.3(d) shows one pair of the fabricated nano-electrodes. We can see clearly the bow-tie shape of the whole electrodes, part of meatal pads and the height profile of the structure.

Then the electrodes were scanned by scanning electron microscopy (SEM) to check the quality of them and get the real distance between two electrodes. During the whole fabrication and the characterization procedures, some nano-electrodes may be mis-aligned (Fig. 3.3(e)), damaged by wire-bonding or by other procedures. Only part of the fabricated devices can work. The gap distances of the nano-electrodes that we are using are 72nm, 100nm, 458nm, and 484nm, respectively. We name the electrodes pairs NE56 with 72nm, NE54 with 100nm, NE23 with 458nm and NE12 with 484nm. The substrate of electrode pair NE54 was not passivated. The good electrodes were wire-bonded with gold wire. Finally, the samples were mounted on a print circuit board (PCB) and the gold wires from electrodes were soldered to leads of chip carrier for electrical measurements.

3.2.4. *Current-Voltage and Photocurrent Characterization*

During the measurements, samples were purged with nitrogen gas to prevent the absorption of humidity. The current-voltage (I-V) measurements were taken under dark. Both of current-voltage (I-V) and photocurrent measurements were taken at room temperature. The equipments used in both experiments were controlled by computer with LabVIEW program. The computer communicates with equipments through GPIB interface with IEEE448.2 protocol. Before the measurements of self-assembled deoxyguanosine crystal (SADG) in between

nano-electrodes, dark-current of nano-electrode pairs were measured first. Dark photocurrents were also measured. Then 3μL deoxyguanosine solution was dropped in between nano-electrode pairs with Hamilton syringe, as shown in Fig. 3.4. In I-V measurement, HP 363

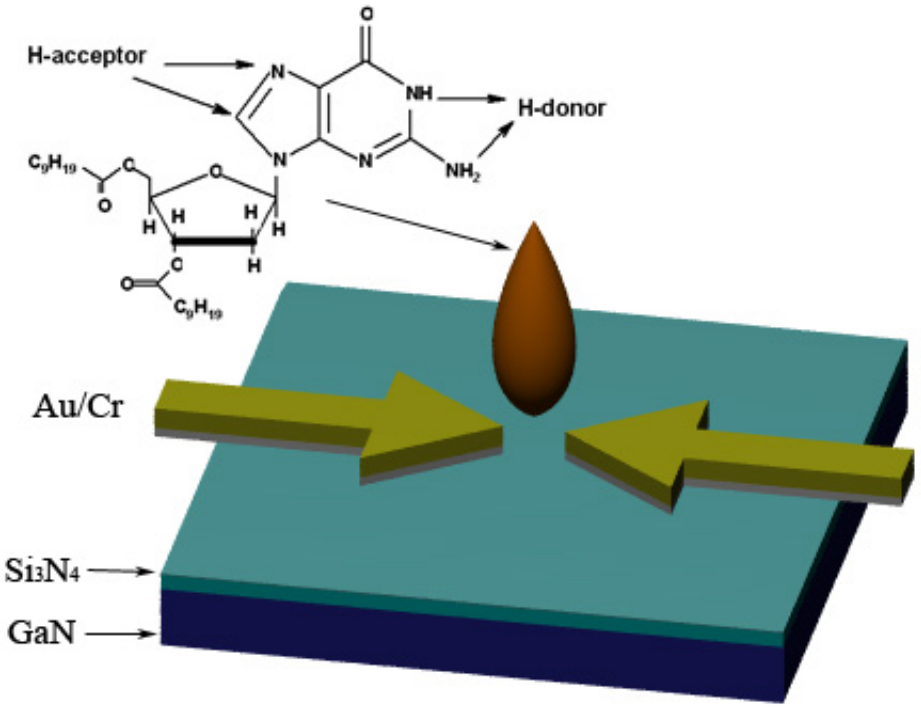

FIGURE 3.4. Schematic of the drop of deoxyguanosine solution in between nano-electrodes

DC power supply and Keithley 486 Pico-Ammeter were connected in series with samples. The applied bias to the samples changed from -10V to 10V with 0.1V step. The computer can change the voltage of DC power supply and read the current value through the circuit by pico-ammeter. While in photocurrent measurements, we used Oriel 6253 xenon arc lamp with 150W power, Oriel 7200 monochromator with a grating of 1200lines/mm, Stanford Research System SR850 lock-in amplifier, and SR540 chopper. Xenon lamp is a white light source covering from UV to near-infrared. The light beam from xenon lamp is collimated and focused on the entrance slit of the monochromator. The single wavelength light from the exit of the monochromator passes the chopper, then is focused onto the samples. The monochromator has a resolution of 0.1nm and works in 200nm to 1200nm range with blazing

wavelength at 350nm. Lock-in amplifier is a phase-sensitive detector which collects only the signal with frequencies falling in the very narrow band-width around a reference frequency. The chopper controller is connected to lock-in amplifier directly through BNC cable and its frequency is used as the reference frequency of lock-in amplifier. The frequency of chopper is set to 1KHz in the photocurrent experiments. The measured signal from samples is sent to lock-in amplifier by BNC cable. Voltage or current signal can be sent to lock-in amplifier. Then the lock-in amplifier calculates Fourier transform of the product of input signal and the internal sine or cosine wave which has reference frequency. The amplitude of the wave which has a different frequency will be zero after Fourier transform. Only the wave which has a very close frequency with the reference can be obtained in consideration of calculation and system error. Then the obtained signal is sent to a band-pass filter. Finally, the signal-to-noise ratio is improved. The computer controls the monochromator to select single wavelength of light that is focused to the samples and the lock-in amplifier to record the voltage across the device. Lock-in amplifier scans for 10 second at each wavelength and then record average voltage.

3.3. Results

3.3.1. *AFM Measurements*

From Fig. 3.5 to Fig. 3.8, AFM images of bare Ga- and N-polar GaN surface and DG films on both surface are listed. In Table 3.1, the roughness of all samples are listed.

TABLE 3.1. Roughness of bare and SADG film on Ga- and N-face GaN substrate

Samples	Roughness(nm)		
	15μm×15μm	3μm×3μm	1μm×1μm
Ga-polar	6.463	5.356	
SADG on Ga-polar	10.917	3.25	1.834
N-polar	11.271	7.747	
SADG on N-polar	4.882	1.045	

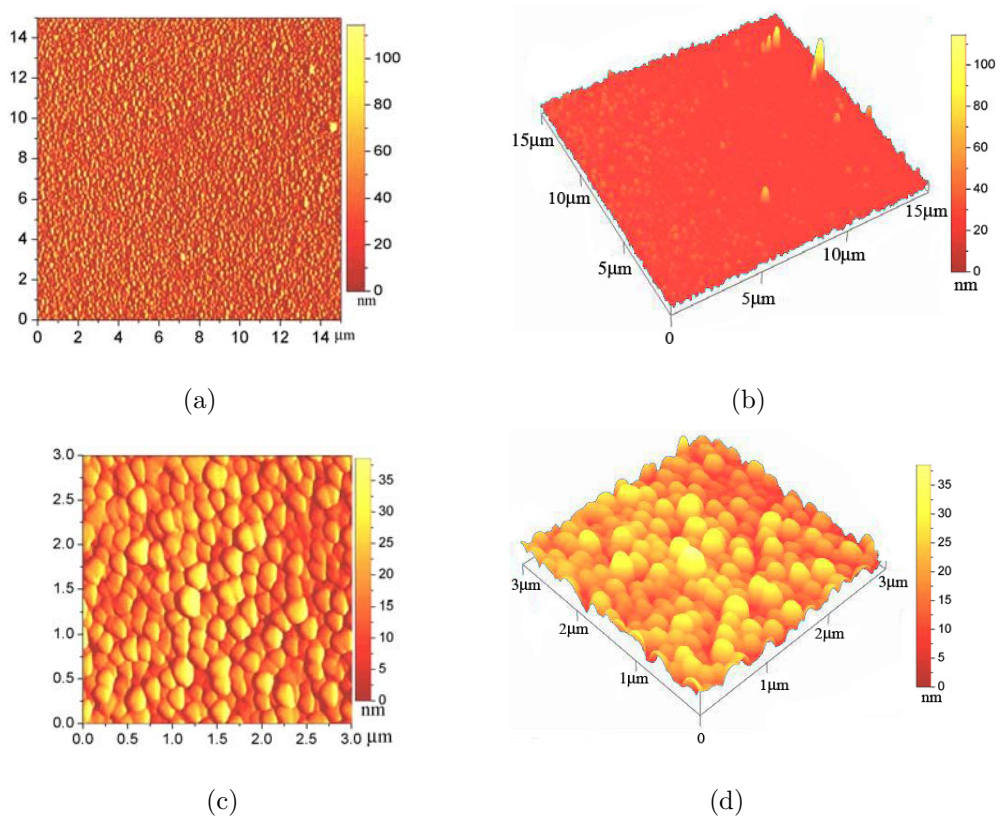

FIGURE 3.5. AFM images of Ga-polar surfaces with (a) top view of 15μm×15μm area, (b) 3-dimensional view of 15μm×15μm area, (c) top view of 3μm×3μm area, and (d) 3-dimensional view of 3μm×3μm area.

From Fig. 3.5-3.6 and Tab. 3.1, Ga- and N-polar surface of GaN have the roughness of 5.356nm and 7.747nm for 3μm×3μm area, respectively. The roughness of Ga-polar surfaces is also less than that of N-polar surface for 15μm×15μm area. Ga-polar surfaces of GaN are smoother than N-polar as indicated by Ponce, et al.[96] Ga-polar surfaces show close-packed islands with different sizes and shapes, as shown in Fig. 3.7(c). The boundaries of islands are very clear. From Fig. 3.8(c), we can see that the islands on N-polar surfaces have less density and relatively large size distribution. The boundaries change slowly in height from island to island. So there are wide ditches between islands and the boundaries are not as clear as that in Ga-polar surface. After the deposition, the self-assembled deoxyguanosine films are smoother on N-polar surface than that on Ga-polar surface, as shown in Fig. 3.7-3.8

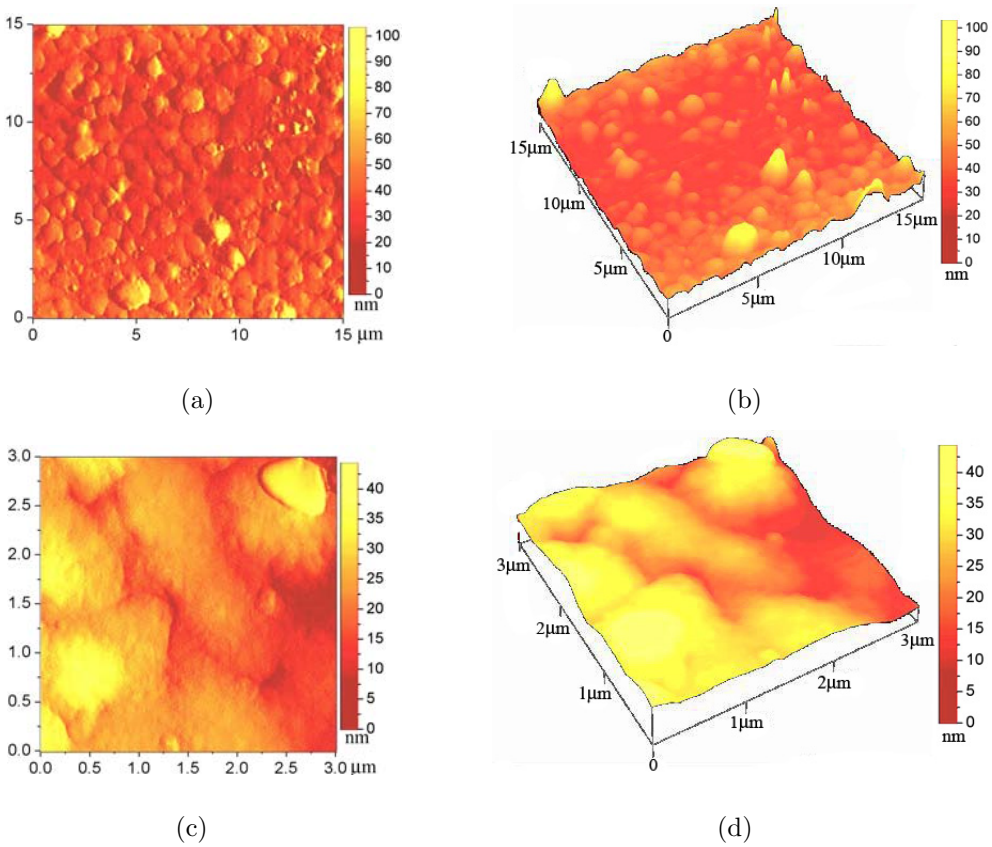

FIGURE 3.6. AFM images of N-polar surfaces with (a) top view of 15μm×15μm area, (b) 3-dimensional view of 15μm×15μm area, (c) top view of 3μm×3μm area, and (d) 3-dimensional view of 3μm×3μm area.

and Tab. 3.1. But as we compare Fig. 3.7(a) with Fig. 3.8(a), DG forms separate, different shape islands with close sizes on Ga-polar substrate and very different size islands with long and wide ditches in between islands on N-polar substrate. The structure of DG films on Ga-polar substrate is similar to the substrates except for relative larger ditches between DG islands. But the structure of DG films on N-polar substrates is not similar to the substrates. For 3μm×3μm area, Fig. 3.7(c) on Ga-polar substrate shows clear thread-like structure, but Fig. 3.8(c) does not show clear thread-like structure. Fig. 3.7(e) has the smallest area with 1μm×1μm within one island on Ga-polar substrate and show very smooth surface with roughness of only 1.834nm. So the Ga-polar surface has better quality, especially on very

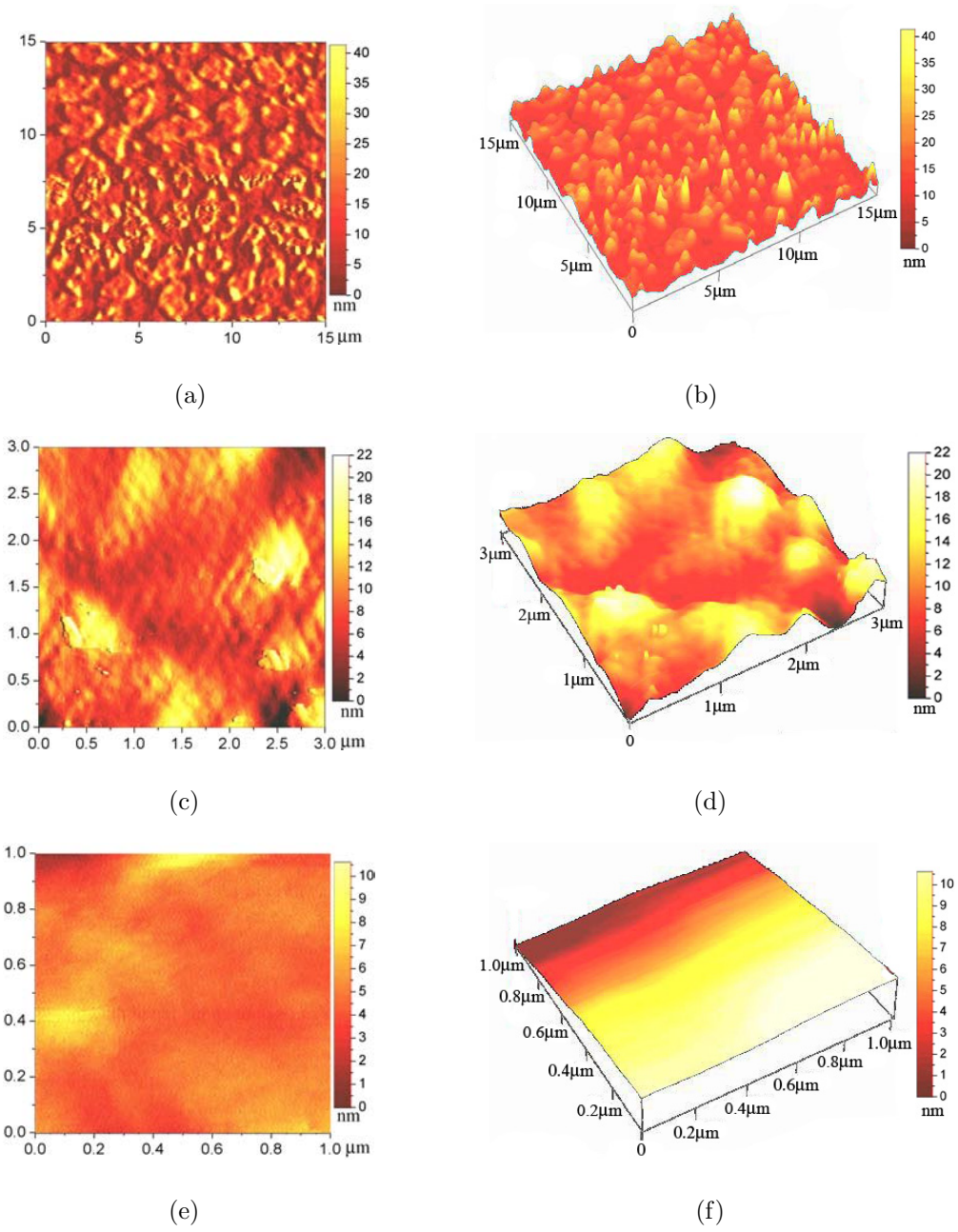

FIGURE 3.7. AFM images of self-assembled deoxyguanosine structures on Ga-polar surfaces with (a) top view of 15μm×15μm area, (b) 3-dimensional view of 15μm×15μm area, (c) top view of 3μm×3μm area, (d) 3-dimensional view of 3μm×3μm area, (e) top-view of 1μm×1μm area, and (f) 3-dimensional view of 1μm×1μm area.

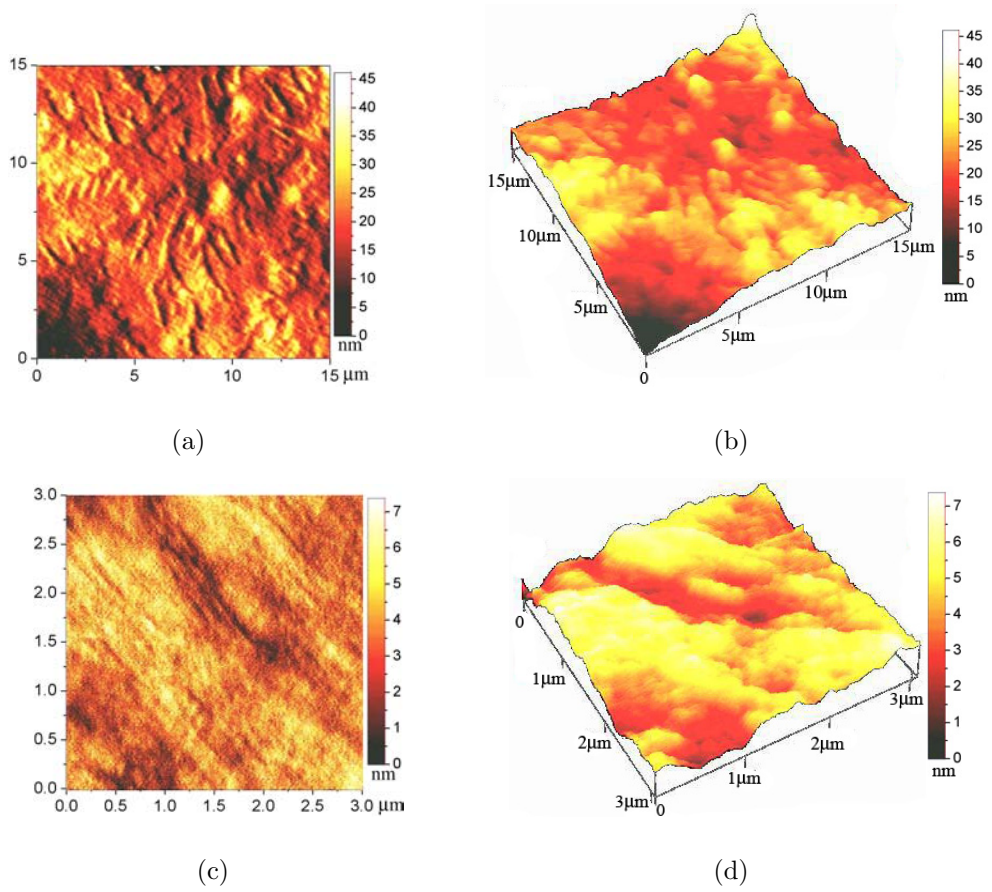

FIGURE 3.8. AFM images of self-assembled deoxyguanosine structures on N-polar surfaces with (a) top view of 15μm×15μm area, (b) 3-dimensional view of 15μm×15μm area, (c) top view of 3μm×3μm area, and (d) 3-dimensional view of 3μm×3μm area.

small area, for self-assembly process of deoxyguanosine derivative than N-polar surface does. In the following experiments, we just used Ga-polar GaN substrates.

3.3.2. *Current-Voltage Characterization Results*

3.3.2.1. *Dark Leakage Current of the Devices.* The ribbon-like self-assembled deoxyguanosine structure and GaN substrate are parallel connected in between one pair of nano-electrodes. If we want to get the current just passing through deoxyguanosine, we have to get the current passing through the substrate first. The current through the GaN substrate is called dark leakage current. In the measurements of dark leakage current, same

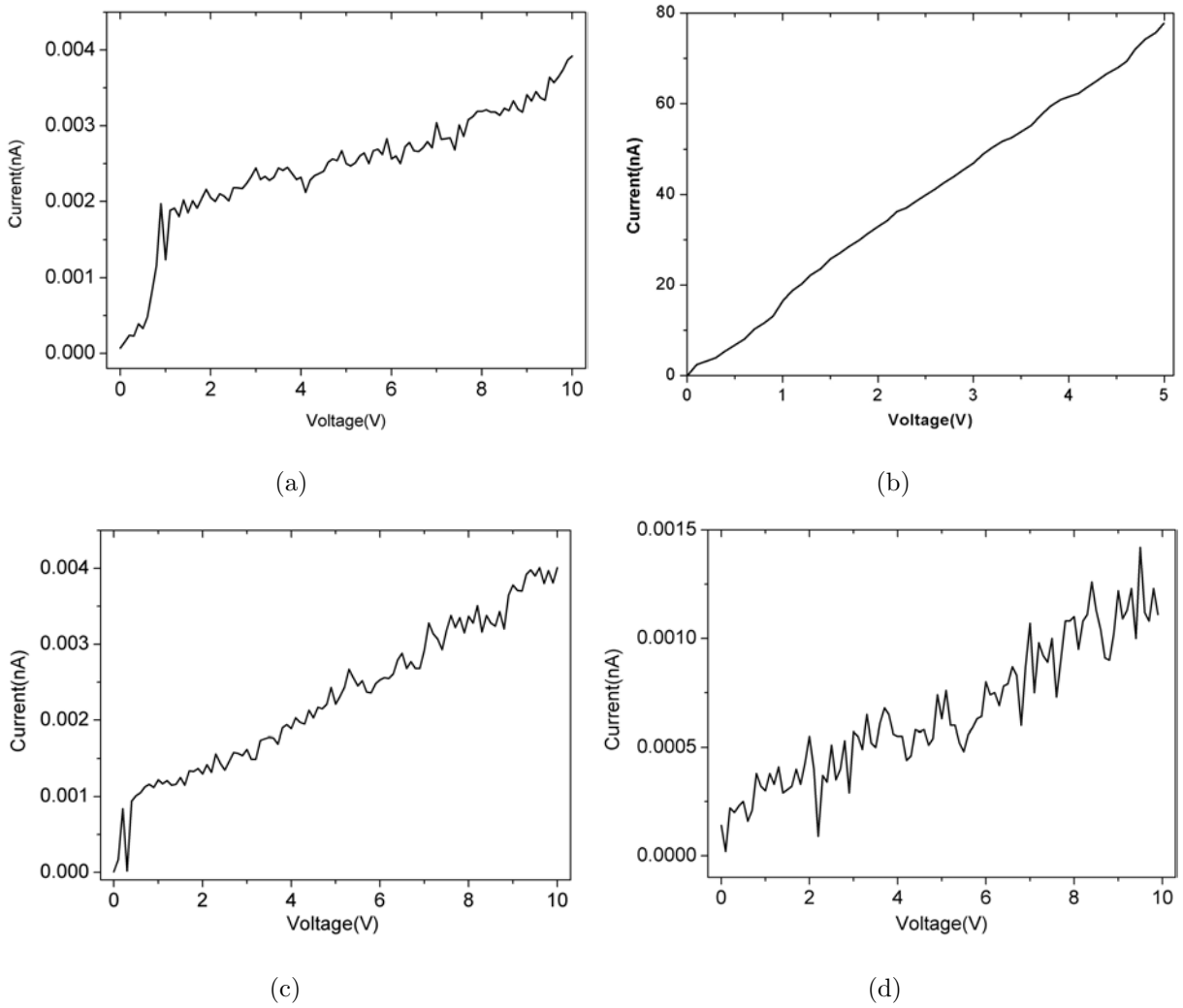

FIGURE 3.9. Dark leakage currents between nano-electrodes for (a) electrode pair NE56 with 72nm gap, (b) electrode pair NE54 with 100nm gap, (c) electrode pair NE23 with 458nm gap, and (d) electrode pair NE12 with 484nm gap.

settings were used as in the measurements of deoxyguanosine. From Fig. 3.9, the dark leakage currents of the devices are in pico-ampere level up to 10V bias except for the electrode pair NE54. The current of electrode pair NE54 reaches about 80nA when the bias gets to 5V because its substrate was not passivated with silicon nitride. Dark leakage current curve of electrode pair NE56, as shown in Fig. 3.9(a), has very small value at 0V bias and goes up to about 4pA at 10V bias. Just like the characteristic of the electrode pair NE56, the

leakage current curve of the electrode pair NE54 in Fig. 3.9(b) is not zero either at 0V bias and goes up to about 80nA to 5V. For the electrode pairs NE23 and NE12, Fig. 3.9(c) and 3.9(d) show the similar characteristics as that of NE56. Thermal excitation of carriers in GaN semiconductor may cause the phenomena. As the bias goes up and overcomes the potential barrier, the curves are more like straight line. Because the dark leakage current is very small and closes to the measurement limit of Keithley pico-ammeter, the curves show large fluctuation.

3.3.2.2. *Current-Voltage Measurements of SADG.* The I-V curves of the self-assembled deoxyguanosine crystals in the four devices are shown in the Fig. 3.10. The currents show the dependence on the gap distance and the substrate properties. The I-V curves (Fig. 3.10(a), 3.10(b), and 3.10(c)) of the device NE56, NE54, and NE23, respectively, show asymmetric, rectifying diode-like characteristic. The current of NE56 reaches about 10nA at 10V forward bias, but only in the order of pA at reverse bias. The current of NE23 can reach over 200nA at 10V forward bias, and over 0.3nA at 10V reverse bias. But the current of NE54 gets to several μA at forward and reverse bias, much higher than the other devices, probably because the substrate of NE54 was not passivated. The I-V curve of the device NE12 shows asymmetric resistance characteristics. The current in one direction is about three times higher than in opposite direction at 10V bias and is higher than that of the devices NE56 and NE23. Next, we will discuss the current-voltage characteristics in detail of the devices separately.

3.3.2.2.1. I-V of the Device NE56. Fig. 3.11 shows the I-V curve at forward bias condition. From Fig. 3.11(b), we can see that the current increases slowly below 0.3V, then increases faster up to about 2V. Finally, the current change slows down when the bias voltage is over about 2V, as shown in Fig. 3.11(a) and this trend is clearer in Fig. 3.11(c) with logarithm plot of current.

From the discussion of metal-semiconductor-metal current-voltage relation in Sect. 2.2.3 of Chap. 2, we can see that minority carrier transport must be dominant in this device

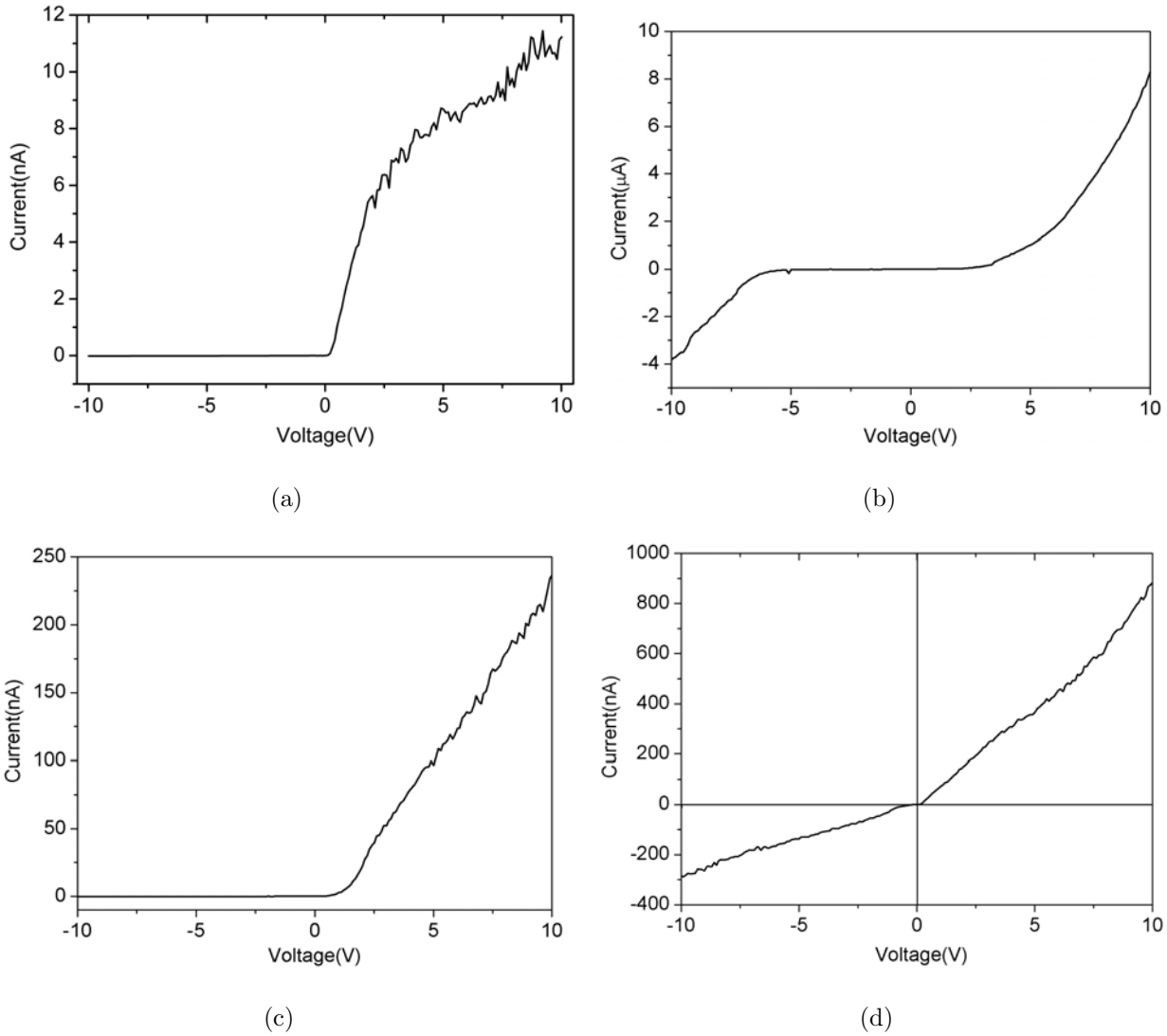

FIGURE 3.10. Current-voltage curves of SADG bridging (a) electrode pair NE56 with 72nm gap, (b) electrode pair NE54 with 100nm gap, (c) electrode pair NE23 with 458nm gap, and (d) electrode pair NE12 with 484nm gap.

because the majority carrier transport follows the same trend if the applied bias voltage is over the reach-through voltage V_{rt}. The change of majority carrier transport is relative slow because it is proportional to $\exp(V^{1/2})$ due to Schottky effect. The change of minority carrier transport is much faster in the applied bias voltage range $V_{rt} < V < V_{fb}$ because it is proportional to $\exp[-(V_{fb} - V)^2]$.

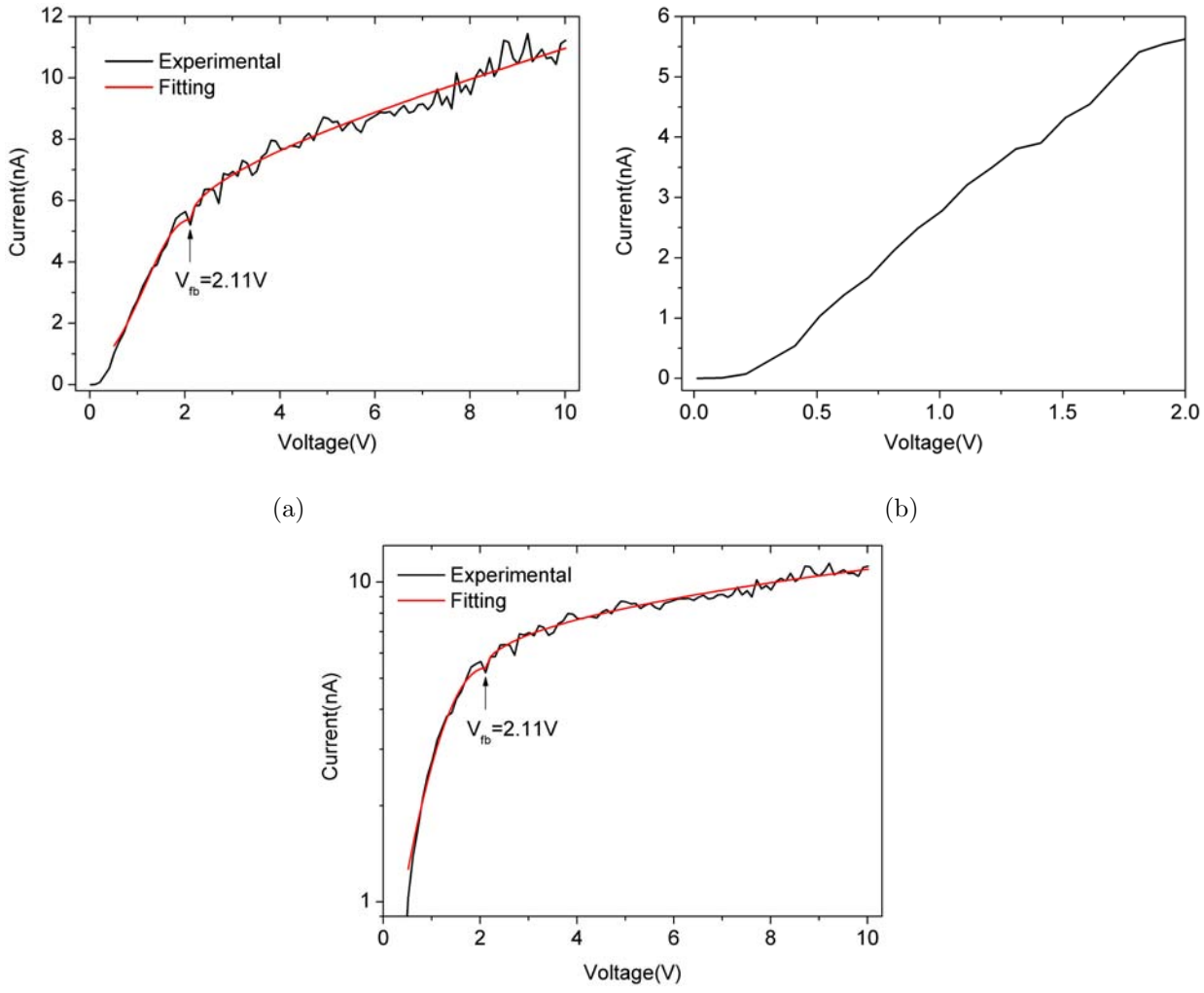

FIGURE 3.11. Experimental and fitting current-voltage curves of the device NE56 with forward-bias (a) Linear plot of whole voltage range, (b) Linear plot of small voltage range, and (c) Semi-logarithm plot of the whole voltage range.

Because there are just several points and the current is very low and close to dark leakage current at the first part of I-V curve, we will not try to fit this part and just analysis the last two parts when the applied voltage is greater than the estimated reach-through voltage V_{rt}. From Fig. 3.11(b), the voltage at which the curve slope changes is estimated to be about $0.3V$.

For one MSM structure, the build-in potentials Φ_{b1} and Φ_{b2} at both contacts are constant. So that the flat-band voltage V_{fb} is also constant from Eq. 56 in Chap. 2 because it depends only on the build-in potential difference and the thickness of the semiconductor. If we neglect the majority carrier transport, Eq. 80 can be simplified as

$$\begin{aligned} J &\approx J_{ps} exp\left[-\frac{q}{4kT(V_{fb}+\Delta\Phi_b)}(V_{fb}-V)^2\right] \\ &= J_{ps}\exp[-\alpha(V_{fb}-V)^2] \end{aligned} \tag{82}$$

where we set $\alpha = \dfrac{q}{4kT(V_{fb}+\Delta\Phi_b)}$ for simplicity. We also neglect the second term in the square bracket of Eq. 80 because q/kT is $38.6V^{-1}$ at room temperature (300K) and make the term very small even with small value of Φ_{b2}. Similarly, Eq. 81 can be simplified as

$$J = J_{ps}\exp\left(\frac{q}{kT}\sqrt{\frac{q(V-V_{fb})}{4\hbar\varepsilon_s L}}\right) = J_{ps}\exp\left(\beta\sqrt{V-V_{fb}}\right) \tag{83}$$

where $\beta = \sqrt{\dfrac{q^{3/2}}{4k^2T^2\hbar\varepsilon_s L}}$, if we only consider Schottky effect. By piecewise fitting the data, we can get

$$I(V) = 5.38\exp\left[-0.57(V-2.11)^2\right](nA) \tag{84}$$

when $0.5V < V < 2.11V$ and

$$I(V) = 5.38\exp\left(0.25\sqrt{V-2.11}\right)(nA) \tag{85}$$

when $V > 2.11V$. The red curves in Fig. 3.11(a) and 3.11(c) are the fitting result. We can see the fitting curves match the experimental data very well. The flat-band voltage V_{fb} is also shown with an arrow on the figures. So the constants are

$$\begin{aligned} I_{ps} &= 5.38 \pm 0.13nA \\ V_{fb} &= 2.11 \pm 0.16V \\ \alpha &= 0.57 \pm 0.09V^{-2} \\ \beta &= 0.25 \pm 0.01V^{-1/2} \end{aligned} \tag{86}$$

where I_{ps} is the product of the saturation current density J_{ps} and the cross section of the contacts.

The dynamic resistance of the device under forward-bias condition is

$$R(V) = \frac{1}{dI/dV} = -\frac{0.163 \exp\left[0.57(V-2.11)^2\right]}{V-2.11}(G\Omega) \tag{87}$$

when $V < 2.11V$ and

$$R(V) = 1.487\sqrt{V-2.11}\exp\left(-0.25\sqrt{V-2.11}\right)(G\Omega) \tag{88}$$

when $V > 2.11V$. As the applied voltage increases in the range $V_{rt} < V < V_{fb}$, the dynamic resistance first decreases slowly and then increases fast, especially when V is close V_{fb}. The minimum resistance is about $0.287G\Omega$ at $V = 1.17V$. The dynamic resistance increases fast at first, then relative slowly when $V > V_{fb}$. The maximum resistance is about $2.070G\Omega$ at $V = 10V$. The dynamic resistance has a jump from $V < V_{fb}$ side to $V > V_{fb}$ side.

Fig. 3.12 shows the I-V curve at reverse-bias condition. The curve has similar trend as at forward-bias condition. The current level is too low below $0.5V$ bias as shown in Fig. 3.12(b). We can fit the curve with Eqs. 82 and 83 and get

$$I(V) = 0.0029 \exp\left[-0.56(V-1.88)^2\right](nA) \tag{89}$$

when $0.2V < V < 1.88V$ and

$$I(V) = 0.0029 \exp\left(0.27\sqrt{V-1.88}\right)(nA) \tag{90}$$

when $V > 1.88V$. The red curves in Figs. 3.12(a) and 3.12(c) are the fitting result and match well with experimental data. The arrows in the above figures show the fitted flat-band voltage. So the constants are

$$\begin{aligned} I_{ps} &= 0.0029 \pm 0.0002nA \\ V_{fb} &= 1.88 \pm 0.16V \\ \alpha &= 0.56 \pm 0.15V^{-2} \\ \beta &= 0.27 \pm 0.02V^{-1/2} \end{aligned} \tag{91}$$

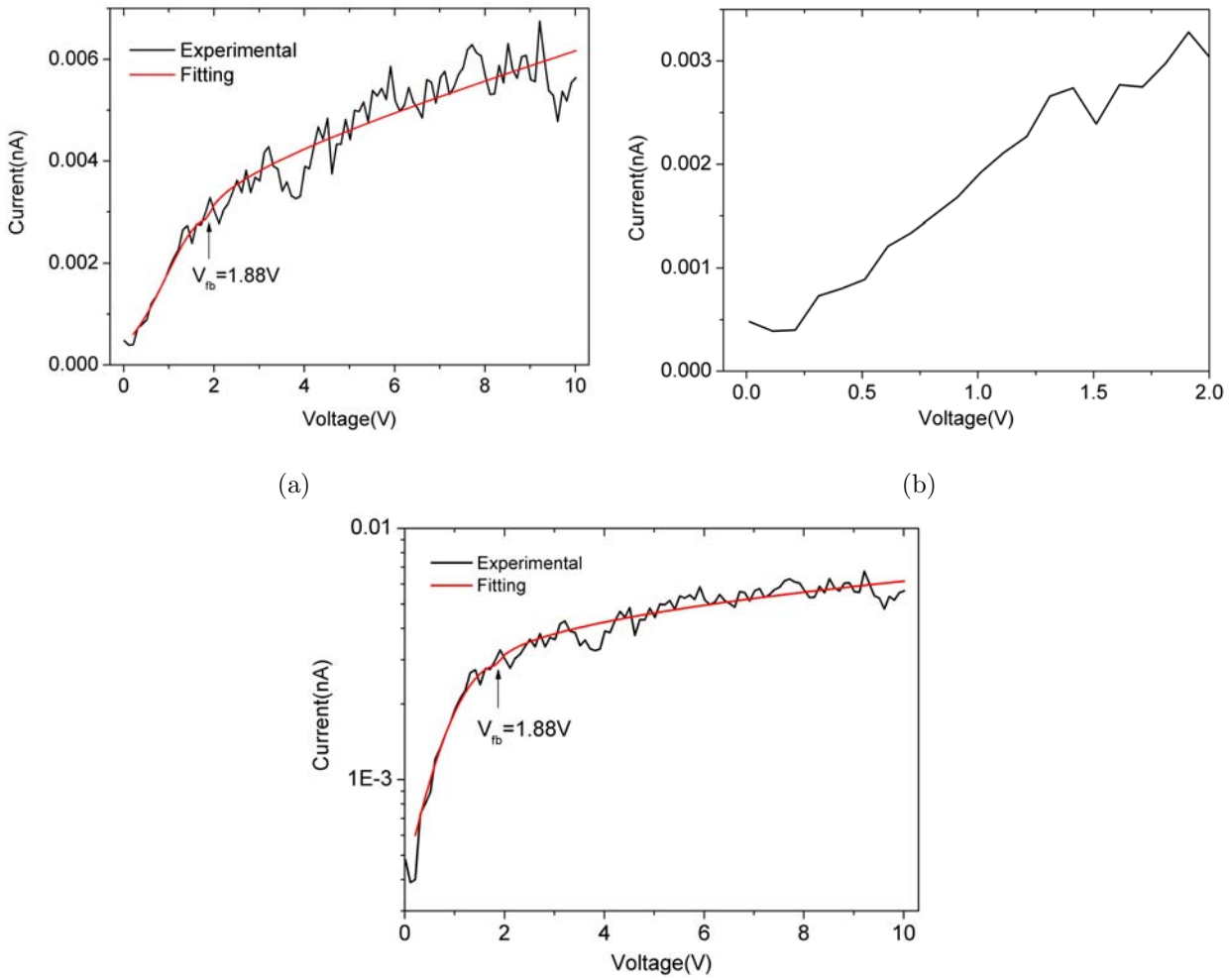

FIGURE 3.12. Experimental and fitting current-voltage curves of the device NE56 with reverse-bias (a) Linear plot of the whole voltage range, (b) Linear plot of the small voltage range, and (c) Semi-logarithm plot of the whole voltage range.

The dynamic resistance under reverse-bias condition is

$$R(V) = -\frac{307.882 \exp\left[0.56(V-1.88)^2\right]}{V-1.88}(G\Omega) \tag{92}$$

when $V < 1.88V$ and

$$R(V) = 2554.28\sqrt{V-1.88}\exp\left(-0.27\sqrt{V-1.88}\right)(G\Omega) \tag{93}$$

when $V > 1.88V$. The change of dynamic resistance has the similar trend as that under forward-bias condition. The minimum dynamic resistance is $537.205G\Omega$ at $V = 0.935V$ when $V_{rt} < V < V_{fb}$. The resistance at $V = 10V$ is $3372.16G\Omega$. The dynamic resistance is much bigger under reverse-bias condition.

Compare the results in Eq. 86 for forward-bias and Eq. 91 for reverse-bias conditions, we can consider that the values of V_{fb}, α, and β are equal at both bias conditions within the fitting error. The reason is that those three values depend only on the material system and the device structure and don't change with applied voltage. Meanwhile, the saturation current depends on the barrier height of the forward-biased contact from the definition in Sect. 2.2.3. Because the two saturation currents are different, the barrier height for minority carrier must be different at both contacts. From the definition of saturation current in Sect. 2.2.3 of Chap. 2, the current changes 10 times if the barrier height changes about $0.06V$ at room temperature and we assume the effective Richardson constant is same for both contacts. The barrier height difference at two contacts is estimated to be $0.19V$ from Eqs. 86 and 91.

3.3.2.2.2. I-V of the Device NE23. Fig. 3.13 shows the current-voltage curves of the device NE23 under forward-bias condition. From Fig. 3.13(b), the current has the similar trends as the device NE56 and changes also relative slow at about $V < 0.5$, although it is not so clear as in the device NE56. We first try to fit the current-voltage data under forward-bias condition with Eqs. 82 and 83 used for the device NE56. There is large discrepancy at $V < 1.4V$ region, as shown in Fig. 3.13(a). The reason is possibly that Eq. 82 only considers Schottky effect. Now we can try to include the effect of the near-surface layer in the barrier height change. From Eqs. 18 and 19, Eq. 84 changes to

$$J = J_{ps} \exp\left[-\alpha(V - V_{fb})^2 + c_1(V - c_2)\right] \tag{94}$$

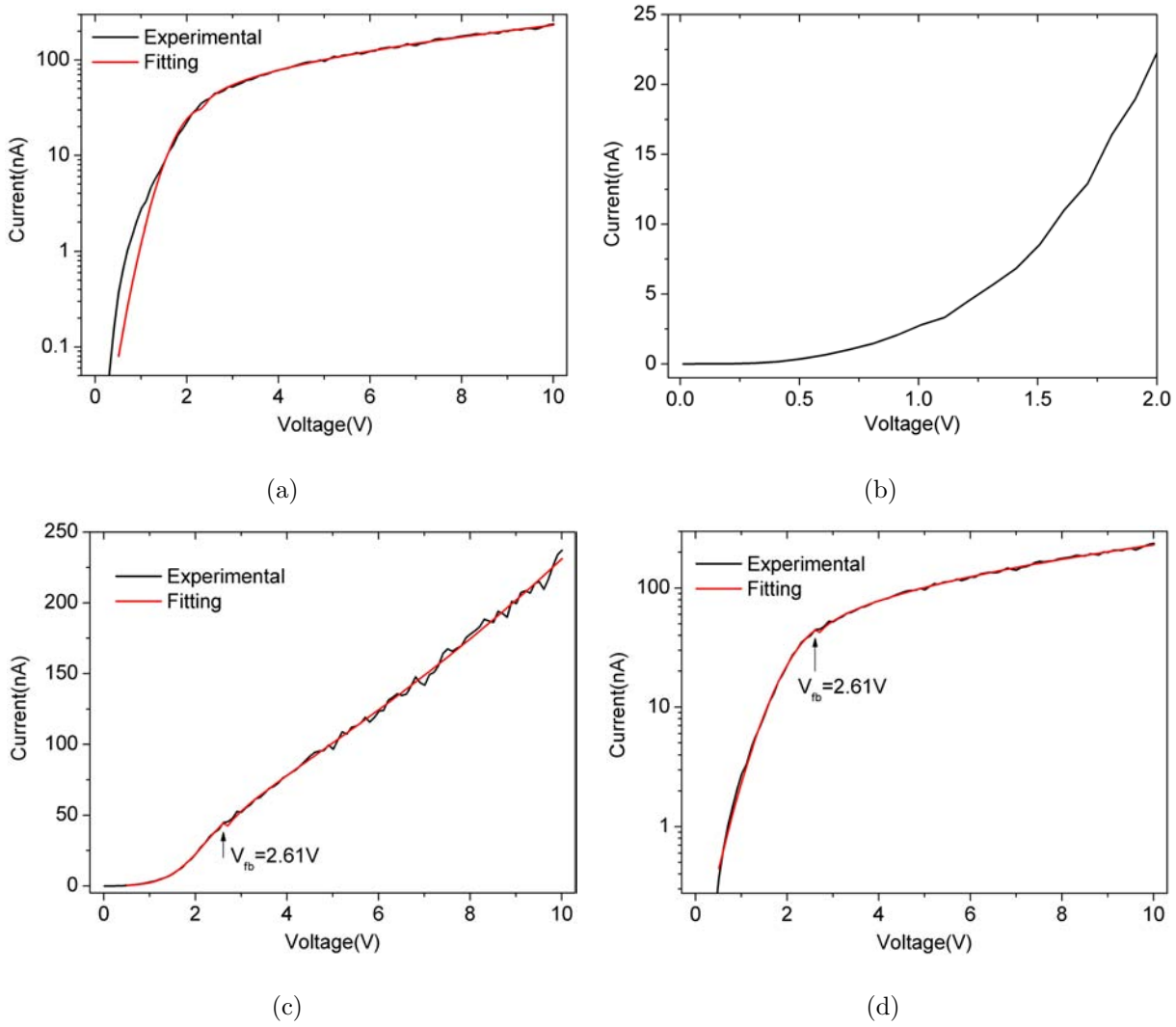

FIGURE 3.13. I-V curves of experimental and fitting of device NE23 at forward-bias condition (a) Semi-logarithm plot of the whole voltage range and fitted with Eqs. 82 and 83, (b) Linear plot at small voltage range, (c) Linear plot of the whole voltage range and fitted with Eqs. 94 and 83, and (d) Semi-logarithm plot of (c).

Same as the device NE56, we just try to fit the I-V curve with Eqs. 94 and 83 except for the small voltage range. Then we get the current

$$I(V) = 33.96 \exp\left[-0.73(V - 2.61)^2 + 0.66(V - 2.21)\right] (nA) \tag{95}$$

when $0.5V < V < 2.61V$ and

$$I(V) = 33.96 \exp\left(0.71\sqrt{V - 2.61}\right)(nA) \tag{96}$$

when $V > 2.61V$. Figs. 3.13(c) and 3.13(d) show the fitting results as red curves. The fitting result matches the experimental very well. The constants used in the equations are

$$\begin{aligned} J_{ps} &= 33.96 \pm 0.97nA \\ V_{fb} &= 2.61 \pm 0.06V \\ \alpha &= 0.73 \pm 0.23V^{-2} \\ \beta &= 0.71 \pm 0.01V^{-1/2} \\ c_1 &= 0.66 \pm 0.26V^{-1} \\ c_2 &= 2.21 \pm 0.11V \end{aligned} \tag{97}$$

The dynamic resistance under forward-bias condition is

$$R(V) = \frac{0.029 \exp\left[0.73(V - 2.61)^2 - 0.66(V - 2.21)\right]}{0.66 - 1.46(V - 2.61)}(G\Omega) \tag{98}$$

when $0.5V < V < 2.61V$, and

$$R(V) = 0.083\sqrt{V - 2.61} \exp\left(-0.71\sqrt{V - 2.61}\right)(G\Omega) \tag{99}$$

when $V > 2.61V$. The dynamic resistance decreases first and then increases slowly in the range $0.5V < V < 2.61v$. The minimum resistance is $0.0266G\Omega$ at $V = 2.234V$. In the range $V > 2.61V$, the dynamic resistance changes differently from the device NE56 and increases fast, then decreases slowly. At $V = 4.594V$, the resistance reaches its maximum value $0.0430G\Omega$. There is also a jump at V_{fb}, the dynamic resistance is also larger at $V < V_{fb}$ side and similar to the device NE56.

Compared with the values in Eq. 86, we can see that the flat-band voltage V_{fb} of NE23 is greater than the value of the device NE56 because of the larger thickness of the semiconductor

layer. The saturation current of NE23 is larger. So the barrier height of forward-biased contact in the device NE23 is lower than the height of the device NE56.

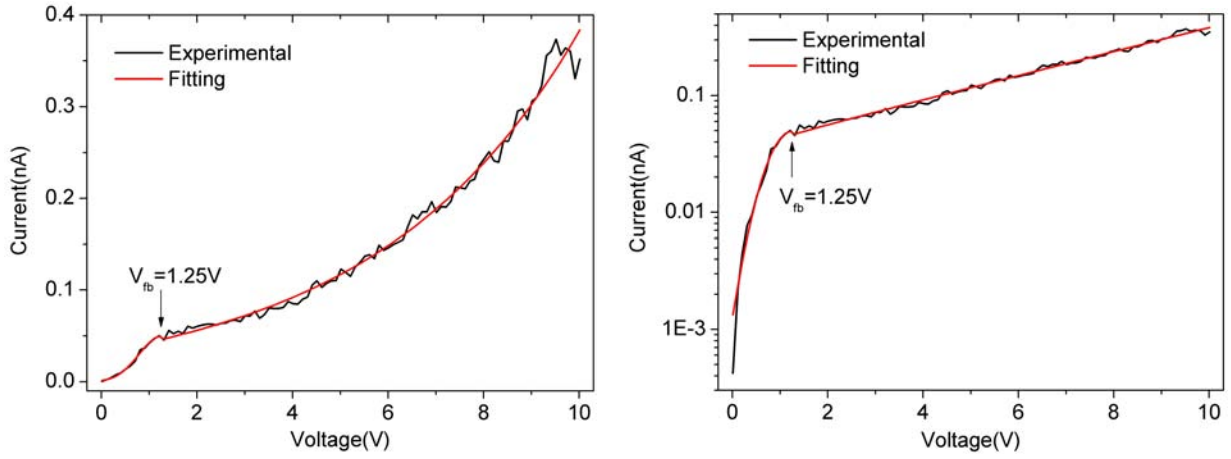

(a) (b)

FIGURE 3.14. Current-voltage curves of the device NE23 under reverse-bias condition (a) Linear plot of whole voltage range and (b) Semi-logarithm plot of whole voltage range.

The current-voltage curve of the device NE23 under reverse-bias condition is shown in Fig. 3.14. Compare Fig. 3.14 with Fig. 3.12 of the device NE56, we can see that the I-V curve of NE23 at the large voltage region is different from the curve of the device NE56. Because the device NE56 considers only Schottky effect, we are trying to include the effect of the near-surface layer to Eq. 83. Then Eq. 83 changes to

$$J = J_{ps} \exp\left[\beta\sqrt{V - V_{fb}} + c_1(V - c_2)\right] \tag{100}$$

By piecewise fitting of the I-V curves under reverse-bias condition with Eqs. 82 and 100, we can get

$$I(V) = 0.050 \exp\left[-2.34(V - 1.25)^2\right] (nA) \tag{101}$$

when $V < 1.25V$ and

$$I(V) = 0.050 \exp\left[0.047\sqrt{V - 1.25} + 0.23(V - 1.64)\right] (nA) \tag{102}$$

when $V > 1.25V$. The red curves in Fig. 3.14 are the fitting curves. They match the experimental data very well. The fitted values are

$$\begin{aligned} J_{ps} &= 0.050 \pm 0.011nA \\ V_{fb} &= 1.25 \pm 0.29V \\ \alpha &= 2.34 \pm 1.79V^{-2} \\ \beta &= 0.047 \pm 0.084V^{-1/2} \\ c_1 &= 0.23 \pm 0.02V^{-1} \\ c_2 &= 1.64 \pm 0.97V \end{aligned} \tag{103}$$

From the discussion of the device NE56, the barrier height difference at both contacts is estimated to be $0.17V$ from Eqs. 97 and 103, which is slightly smaller than that of the device NE56.

The dynamic resistance under reverse-bias condition is

$$R(V) = -\frac{4.27 \exp\left[2.34(V-1.25)^2\right]}{V-1.25}(G\Omega) \tag{104}$$

when $V < 1.25V$ and

$$R(V) = \frac{20 \exp\left[-0.047\sqrt{V-1.25} - 0.23(V-1.64)\right]}{0.23 + 0.0235(V-1.25)^{-1/2}}(G\Omega) \tag{105}$$

when $V > 1.25V$. The dynamic resistance first decreases, then increases fast in the range $V < 1.25V$. It reaches its minimum $15.242G\Omega$ at $V = 0.788V$. In the range $V > 1.25V$, the dynamic resistance increases very fast and decreases slowly after it reaches the maximum value $72.921G\Omega$ at $V = 1.541V$.

From the above values, the effect of NSL should be dominant rather than Schottky effect as $V > V_{fb}$. The current is at very low level, so the fitted value responsible for Schottky effect has small value and very big error. The difference of the flat-band voltage V_{fb} under forward- and reverse-biased conditions is possibly due to the NSL effect.

From the previous discussion, we can see that the dynamic resistance of the devices are very large. The first possible reason is that the diameter of the ribbon-like structure is in the order of Ångrström and the resistance is proportional to the cross-section of the structure. The second possible reason is that the carrier concentration is very low in the structure, so the carrier injection can not be very fast. The third one is that the barrier height is high and it causes the saturation current low. Compared the dynamic resistance of the device NE56 and NE23 under reverse-bias condition, we can see that the device NE23 has much smaller dynamic resistance than that of the device NE56. This is probably mainly because NE23 has much higher saturation current than that of NE56. The saturation current ratio of NE23 to NE56 is $0.05/0.0029 \approx 17$. Under forward-bias condition, the dynamic resistance ratio below V_{fb} has the similar value to the saturation current ratio of NE23 to NE56. But the dynamic resistance of NE23 is even higher than that of NE56 above V_{fb} probably because of the NSL effect of NE23 which is dominant instead of Schottky effect.

From Figs. 3.11 to 3.14, we can see that the current curve is smooth below the flat-band voltage V_{fb} and fluctuates clearly near and above V_{fb}. The fluctuation is probably due to the oscillation of current-voltage and NSL effect. For MSM structure, the capacitance decreases slowly as the applied voltage increases in the range $V > V_{rt}$ because the minority carrier current increases[84]. Meanwhile, the dynamic resistance is much smaller in the region $V_{rt} < V < V_{fb}$ than that in the region $V > V_{fb}$ except for the device NE23 under forward-bias condition. The time constant of the structure is longer in the region $V > V_{fb}$. The current is probably still oscillating when it is read by computer after the voltage change.

The change of potential drop in the near-surface-layer is induced by the redistribution of charges on deep states in NSL. When the applied voltage changes, the process of charge redistribution probably can not follow the voltage change so quickly and exactly. So the charge redistribution may have damping oscillation process. It induces the oscillation of the potential drop in NSL. For the device NE23 under forward-bias condition, the NSL effect is

probably the dominant effect in current-voltage relation. So the current fluctuation may be large due to the NSL effect.

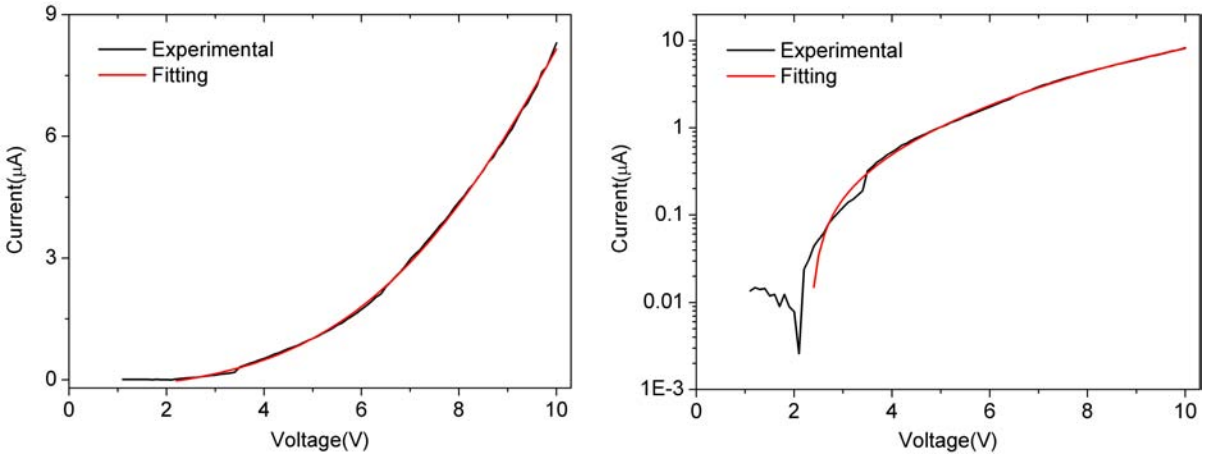

(a) (b)

FIGURE 3.15. Experimental and fitting current-voltage curves of the device NE54 under forward-bias condition (a) Linear plot of whole voltage range and (b) Semi-logarithm plot of whole voltage range.

3.3.2.2.3. I-V of the Device NE54. Fig. 3.15 shows the I-V curves of the device NE54 under forward-bias condition. The current fluctuates largely at low voltage region. The current jump from $3.4V$ to $3.5V$ may be due to experimental error. The current increases fast when the applied voltage is over about $2.4V$ till the largest voltage. The curve doesn't show the change of increasing trend at large voltage. So we fit the curve just with Eq. 80 neglecting the majority carrier transport and get

$$I(V) = 16.96 \exp\left[-0.023(V - 15.48)^2\right] - 0.31(\mu A) \tag{106}$$

when $V > 2.4V$. The constant values are

$$\begin{aligned} I_{ps} &= 16.96 \pm 1.24 \mu A \\ V_{fb} &= 15.48 \pm 0.45 V \\ \alpha &= 0.023 \pm 0.001 V^{-2} \end{aligned}$$

$$c_3 \quad = \quad 0.31 \pm 0.04 \mu A \tag{107}$$

Here we set $c_3 = J_{ps} \exp\left(-\frac{q\Phi_{b2}}{kT}\right)$ for the second term in the square bracket of Eq. 80. The red curves in the figure are the fitting result. The fitted flat-band voltage V_{fb} is out of the range of the applied voltage and the curve has only one trend above the small voltage region. We have to increase the voltage even higher to get turn-point of the curve. The saturation current is about three orders higher than that of the device NE56 and the gap distances of the two device are close. The substrate property may play a very important role for the difference because the substrate of NE56 was passivated, but not the device NE54. The dynamic resistance under forward-bias condition is

$$R(V) = -\frac{1.28 \exp\left[0.023(V - 15.48)^2\right]}{V - 15.48} (M\Omega) \tag{108}$$

when $V > 2.4V$. The dynamic resistance keeps decreasing till $10V$ and reaches its minimum value $0.467M\Omega$ at $10V$.

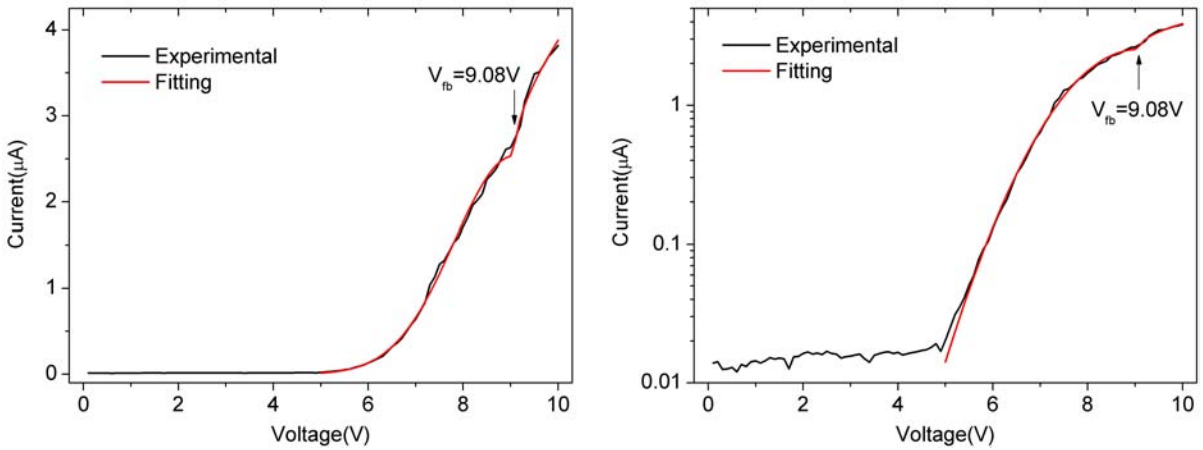

FIGURE 3.16. Experimental and fitting current-voltage curves of the device NE54 under reverse-bias condition (a) Linear plot of the whole voltage range and (b) Semi-logarithm plot of the whole voltage range.

Fig. 3.16 shows the current-voltage curve under reverse-bias condition. The current keeps at low level and increases very slowly from $0V$ to about $5V$. Then the current goes up very

fast and slows down over $8V$. As discussed before, we can fit the curve with Eqs. 82 and 83 except the region below $5V$. Then we get

$$I(V) = 2.54 \exp\left[-0.31(V - 9.08)^2\right] (\mu A) \tag{109}$$

when $5V < V < 9.08V$ and

$$I(V) = 2.54 \exp\left(0.44\sqrt{V - 9.08}\right) (\mu A) \tag{110}$$

when $V > 9.08V$. The constant values are

$$\begin{aligned} I_{ps} &= 2.54 \pm 0.02 \mu A \\ V_{fb} &= 9.08 \pm 0.01 V \\ \alpha &= 0.21 \pm 0.01 V^{-2} \\ \beta &= 0.44 \pm 0.01 V^{-1/2} \end{aligned} \tag{111}$$

The red curves are the fitted results and match the experimental data. The device NE54 has the same property of the flat-band voltage as that of the device NE23. The flat-band voltages V_{fb} are different under forward- and reverse-bias condition and have larger value under forward-bias condition. The barrier height difference at both contacts is estimated to be $0.014V$ from Eqs. 107 and 111. The dynamic resistance under reverse-bias condition is

$$R(V) = -\frac{0.635 \exp\left[0.31(V - 9.08)^2\right]}{V - 9.08} (M\Omega) \tag{112}$$

when $5V < V < 9.08V$ and

$$R(V) = 1.790\sqrt{V - 9.08} \exp\left(-0.44\sqrt{V - 9.08}\right) (M\Omega) \tag{113}$$

when $V > 9.08V$. The dynamic resistance first decreases fast, then very slow, and finally increases very fast in the region $5V < V < 9.08V$. The minimum value is $0.824M\Omega$ at $V = 7.81V$. The dynamic resistance increases monotonically when $V > 9.08V$. Compared with the devices NE56 and NE23, the device NE54 has much smaller dynamic resistance mainly due to the much larger saturation current.

3.4. Discussion

From the above analysis of the four devices, the devices with gap distance up to $458nm$ show semiconductor characteristics and the one with gap distance $484nm$ shows resistance characteristics. So the length of self-assembled deoxyguanosine crystal is longer than that Rinaldi, et al. got[65]. The carrier transport in SAGC is band-like. The current-voltage curves show strong rectification characteristics and the minority carriers dominant the current flow. That means the potential barriers at both contacts of the metal-semiconductor-metal structure are not same and the barrier height of minority carriers is lower than that of the majority carriers. Because the modified guanosine molecules have large dipole moment up to 7 Debye. The self-assembled ribbon-like structure, as shown in Fig. 1.3, also has dipole moment along the ribbon axis. Suppose the majority carriers in SAGC are electrons. When the deoxyguanosine molecules self-assemble between two metal nano-electrodes, SAGC must have polarization along the direction of the ribbon-like structure that connects the two metal electrodes. This intrinsic polarization will tilt the band structure of SAGC and push the Fermi level down to valence band. As the length of the ribbon-like structure gets longer, the polarization should be stronger and the Fermi level is pushed deeper down to valence band. When the self-assembled structure gets contact with metal electrodes, the Fermi level in SAGC is going to align the Fermi level in the metal electrodes. The formed barriers at two ends of the self-assembled ribbon-like structure will be different due to the tilted band of SAGC. The difference should be larger for longer ribbon-like structure. But from the discussion of the devices NE56 and NE23, we can see the opposite result. Probably NSL effect induces the contradiction because it is clear shown in the device NE23. The lower the Fermi level is, the lower the barrier height is for holes. So we can see that the saturation current of the device NE23 with gap distance $458nm$ is higher than that of the device NE56 with gap distance $72nm$.

Usually Schottky effect plays the most important role in current-voltage characteristics. The effect of near-surface layer affects some devices under certain conditions. It is still not

clear when the NSL effect has clear influence on the I-V characteristics. Because the barrier height of contacts also depends on the materials, the interface of metal-semiconductor, and fabrication process, et al., some of the fitting results, like the flat-band voltage of the devices NE23 and NE54, can not be explained by the ideal model with consideration of Schottky effect and NSL effect.

When we compare the result with that in Ref. [97] by Cingolani, et al., we can see several different characteristics.

- The current-voltage curves are asymmetric even for the device with gap distance up to $458nm$ in our research. The I-V curve in the reference is almost symmetric for the device with $120nm$ gap distance. So the self-assembled structure may not have strong polarization along the direction connecting the two metal electrodes because the current depends on the barrier heights at two contacts as discussed previous. Although the I-V curve shows MSM characteristics for the device with $120nm$ gap distance, the semiconductor is probably not a simple parallel-strand ribbon-like structure with same direction or the polarization of the structure is canceled out because of unknown reasons if it is a parallel-strand ribbon-like structure.
- The currents in our devices is much lower than that in the reference except for the device NE54 which has the similar current magnitude. Probably just like the devices we used, the substrate properties causes the difference. The substrate of the device NE54 was not passivated, but the substrate of the other devices were passivated. Rinaldi, et al. used silicon substrate and the substrate was passivated with silicon dioxide (SiO_2).
- I-V curves of the device NE54 and the device with $60nm$ gap distance in the reference don't get to the flat-band voltage till $10V$ voltage because the currents are still increasing very rapidly at $10V$. The devices NE56, NE23 and the one with $120nm$ gap distance in the reference have similar flat-band voltage.

- Because the saturation currents of the device NE56 and NE23 are lower than the devices NE54 and that in the reference, the dynamic resistance is much bigger in the device NE56 and NE23. So the response time of the devices may be different.

We can conclude that the deoxyguanosine molecules can self-assemble into semiconductor in confined spaces up to $458nm$. The substrate property affects the self-assembly of deoxyguanosine structure. The process of the same substrate can also have different impact on SAGC. The intrinsic polarization of ribbon-like SAGC induces asymmetric I-V characteristics. So the device based on SAGC can be used in rectifying circuits.

CHAPTER 4

PHOTOCURRENT CHARACTERISTICS OF GALLIUM NITRIDE/ DEOXYGUANOSINE BASED PHOTODETECTOR

4.1. Metal-Semiconductor Photodiode

A photodiode based on semiconductor has a depletion region. The electron-hole pairs created by incident photons are separated by the electric field in the depletion region. The response time can be very short if the thickness of the region is small. But the quantum efficiency may be low because the small volume that photons interact with semiconductor. The photodiode can work under either bias or unbias condition. Under unbias condition, it is called photovoltaic mode and works similar to solar cell. Under bias condition, photodiode is reverse-biased to reduce carrier transmit time. The photodiode can be p-n junction, metal-semiconductor diode, or p-i-n diode. Depending on the semiconductor material used, photodiode has very different working region and efficiency because the semiconductor material has its own absorption region. The absorption region determines the longest wavelength of the incident light that the photodiode can detect. If the wavelength is too short, the absorption of light and the creation of electron-hole pairs are mainly occurred in the narrow-layer near surface. The created electron-hole pairs can recombine in a very short time, then can not be collected. Silicon photodiodes can have very high quantum efficiency in near-infrared regime while metal-semiconductor photodiode are very sensitive in UV and visible regime because many semiconductors have high absorption coefficients in this region[73].

Metal-semiconductor photodiodes have different working regimes. Depending on the incident photon energy and bias voltage, it can be

(1) When $E_g > h\nu > q\Phi_n$ and $V < V_B$, where ν is the frequency of incident photons, h is Planck constant, and V_B is the breakdown voltage, the electrons in metal can

be excited by incident photons to energy that is higher than the barrier height at the metal-semiconductor contact. Electrons can also be excited from defect levels to conduction band. The electrons then can be collect by the semiconductor.

(2) When $h\nu > E_g$ and $V < V_B$, electron-hole pairs are created by incident photons. The electrons and the holes are collected by semiconductor and metal, respectively.

(3) When $h\nu > E_g$ and $V \approx V_B$, it works like an avalanche photodiode. The electron-hole pairs are created not only by incident photons but also by the carriers in semiconductor.

4.2. Metal-Semiconductor-Metal Photodetector

Metal-semiconductor-metal photodetector is based on metal-semiconductor photodiode. MSM photodetector based on wide-band gap semiconductor has very low dark current because the rectifying effect of Schottky contacts and the high resistivity of semiconductor[98]. The device also has very short response time due to small capacitance. It has already been used for high-speed applications.

As photons incident on the semiconductor of the device, as shown in Fig. 2.8(a) in Chap. 2, there are also three different regimes as described in the previous section. If the energy of the incident photons are high enough to excite electrons from valence band or defect levels to conduction band, there are two different situations in semiconductor. First, if the electron-hole pairs are created inside depletion layer, electrons and holes drift to contacts under electric field and then are collected by contacts or recombine. Second, the electrons and the holes created outside the depletion layer, the neutral region, can diffuse to the depletion layer, then are collected by the contacts or recombine. If the bias voltage is low, the carriers can be tunneling through Schottky barriers and collected by contacts. As the bias voltage increases, the thickness of the depletion layers and the electric fields inside the layer increase. The thickness of neutral region decreases, and finally vanishes. The probability of carriers collected will increases because the carriers can drift faster in higher electric field. So the

photocurrent goes up as the bias voltage increases. As the bias voltage is even higher, the photocurrent saturates.

4.3. Experimental Result

The fabrication and the photocurrent experimental procedure of the hybrid MSM structures are already described in Chap. 3. The devices used have the same names as in that chapter. The relation between energy E in eV and the wavelength λ in nm of light is

$$E(eV) = \frac{1240}{\lambda(nm)} \tag{114}$$

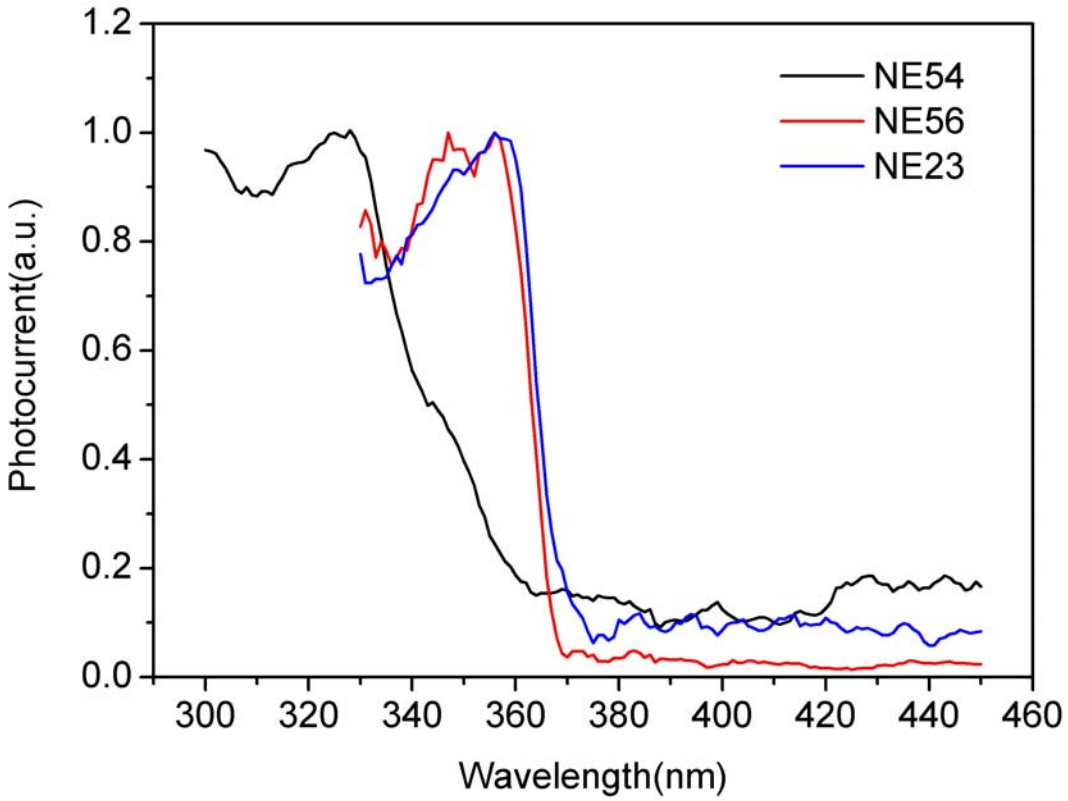

FIGURE 4.1. Normalized photocurrents of the device NE56, NE23 and NE54 at 0V bias.

Fig. 4.1 shows the photocurrent curves at 0V bias of the devices NE56, NE23, and NE54 in which SAGC show semiconductor characteristics in MSM structure as described in Chap. 3. From Fig. 4.1, we can see that the photocurrent curves of all three devices are at very low level, the background level, at long wavelength region of the incident light. As the wavelength

decreases, that means the energy of photons increases, the photocurrent curves start to go up. The wavelengthes at which the photocurrents start to increase are about $370nm(3.35eV)$, $374nm(3.32eV)$, and $364nm(3.41eV)$, respectively, for the devices NE56, NE23 and NE54. The photocurrents get to their high levels and then decrease slowly as the wavelength of incident light decreases even further. The photocurrents of the devices NE56, NE23, and NE54 get to the edge of the curves top at the wavelengths $357nm(3.47eV)$, $359nm(3.45eV)$, and $328nm(3.78eV)$, respectively. So the bandgaps of self-assembled deoxyguanosine structure in the device NE56 and NE23 are about $3.47eV(357nm)$ and $3.45eV(359nm)$, respectively. The bandgap of the device NE54 is higher and get to about $3.78eV(328nm)$. The increasing part of the curves of the devices NE56 and NE23 are almost parallel and steeper than that of the device NE54.

Compared with the device NE56 and NE23, the SAGC in the device NE54 has larger bandgap probably because of the relative weaker intrinsic polarization. The band is tilted smaller if the intrinsic polarization is weaker. If the barrier height of Schottky contact is small, the electrons in metal can be excited to high energy level so that the electrons can move to semiconductor at relative long wavelength. So the increasing part of the photocurrent curve can be gentle.

For the photocurrent curves, the bandgap of SAGC is larger in the device NE56 than that in the device NE23. Because the length of the ribbon-like structure of SAGC is shorter in NE56 than that in NE23, the intrinsic polarization should be weaker in NE56, just like what is described in Chap. 3. This can induce the difference of the bandgaps. The increasing part of the photocurrent curve is steep probably because the barrier height is relative high. The electrons in metal can be excited to high energy levels at relative short wavelength. This also proves the reasoning about the energy levels in MSM structure from current-voltage characteristic as described in Chap. 3.

Fig. 4.2 shows the change of photocurrent in the device NE23 with the applied bias voltage. The photocurrent has a increasing trend with increasing voltage. But the wavelengths

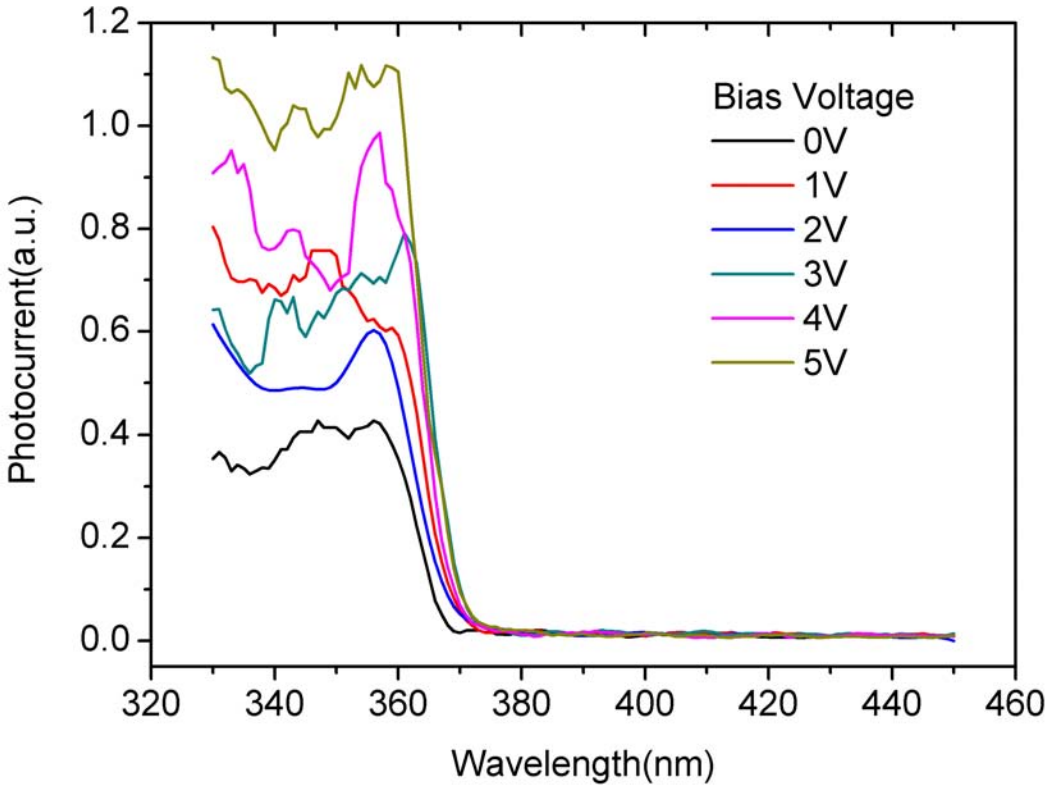

FIGURE 4.2. Photocurrents of the device NE23 at the applied bias from $0V$ to $5V$.

at which the photocurrents start to increase are very close under all bias condition. That means the barrier height doesn't change, or change very tiny under the bias voltage from $0V$ to $5V$ if the increasing of photocurrent at long wavelength is due to the electrons transporting from metal to semiconductor. The top edges of the photocurrents are also very close. The bandgap of SAGC doesn't change with the applied bias voltage. The photocurrent at $5V$ bias is greater than that at $4V$ bias. So the photocurrent does not saturate at $5V$ and can increase even higher at higher bias voltage. The fluctuation of photocurrent at short wavelength may be because the intensity of xenon lamp drops fast and is weak at short wavelength region.

4.4. Discussion

From the photocurrent characteristic of MSM structure based on self-assembled deoxyguanosine structure, we can see that SAGC shows semiconductor characteristic at confined space up to $458nm$ in length. The fabrication process of substrate also affects the conjugation and the alignment of energy levels of biomolecule deoxyguanosine to metal. So the photocurrent has different slope and the wavelength at which the photocurrent starts to increase. The intrinsic polarization also plays important role in the photocurrent measurement. It tilts the bands of SAGC, so the bandgap changes. We can see that both current-voltage and photocurrent characteristics show the same information about the metal-semiconductor-metal structure based on self-assembled ribbon-like deoxyguanosine structure.

CHAPTER 5

MODELING OF GALLIUM NITRIDE/DEOXYGUANOSINE-BASED HYBRID PHOTONIC CRYSTAL

5.1. Introduction

Photonic crystals(PC) are widely used to tailor light propagation[99, 25, 26, 100, 101, 24, 102] and control spontaneous and stimulated light emission[103, 104, 105, 106, 107, 30]. Because gallium nitride(GaN) and its alloys are dominant materials for light-emitting devices from green to UV region, photonic crystals based on GaN are investigated to improve extraction efficiency of light emitting devices[108, 109, 110, 111]. GaN-based photonic crystal nancocavities are also investigated to control light emission[104, 107, 106].

Because most biological agents emit or absorb lights in UV regime[112], the coupling efficiency between light source and biomolecules is very important in developing biocompatible nanophotonic sensing and labeling system in this regime. Among biomolecules, DNA has a fundamental role in biological processes. Among the bases of DNA, guanosine has the lowest oxidation potential, which favors carrier transport. The guanosine base has particular sequence of hydrogen-bond groups (Fig. 1.2) that can work as donors or acceptors[89] and promote the self-recognition and self-assembly processes in solution and directly onto solid surfaces from solution. Depending on the environment, guanosine can undergo different self-assembly pathways[89, 64]. Modified deoxyguanosine molecules self-assemble into ribbon-like structure in confined space on silicon dioxide[97] and gallium nitride[113] surfaces. GaN surface can form negative or positive polarity by nitrogen or gallium termination. The surface polarity can be used to enhance the self-assembly process of deoxyguanosine. Gallium terminated surface is found to be better than nitrogen terminated surface for the process, as described in Chap. 3. SAGC has similar optical properties($\sim 3.4eV$ bandgap) as that of

GaN from photocurrent measurement. Direct coupling of DNA nucleotides with GaN/AlN QD was investigated for possible conjugating to other biomolecules and found enhancement of photoluminescence from SAGC molecules[112].

The lattice constants of photonic crystal based on GaN are in the order of one or two hundred nanometer in UV to blue region. The modified deoxyguanosine molecules can self-assemble into crystal structure inside holes of GaN-based photonic crystals if the deoxyguanosine solution is infiltrated into the holes. By tuning lattice constant, hole radius, and slab thickness, the density of states of light can be tuned in the photonic crystals. So the coupling efficiency of deoxyguanosine to light source can be improved when the deoxyguanosine molecules are detected or work as functional linker to sense or label other biomolecules. Similar method was used in polymer hydrogel photonic crystals to sense glucose and lead[114, 115, 116]. The hybrid photonic crystal of GaN and SAGC with slab structure and no defects are simulated in this chapter.

5.2. Softwares Introduction

We use two software to design hybrid photonic crystal, MIT Photonic-Bands(MPB) from MIT and EMPLab$^{\text{TM}}$ from EM Photonics, Inc..

5.2.1. *MIT Photonic-Bands*

MIT Photonic-Bands(MPB) is a free software and was developed by Steven G. Johnson and J. D. Joannopoulos's Ab Initio Physics group. MPB can be used to compute band structure of periodic dielectric structures, waveguides or resonator modes. It is based on block-iterative frequency-domain methods in a planewave basis. The following part is the basic introduction of the theory used in the software according to Ref. [117] by Johnson and Joannopoulos.

Suppose light travels in linear dielectric medium without source, then

$$\nabla \times \frac{1}{\varepsilon(\vec{r})} \nabla \times |H\rangle = -\frac{1}{c^2} \frac{\partial^2}{\partial t^2} |H\rangle \tag{115}$$

where $|H\rangle$ is the magnetic field, c is the speed of light, and $\varepsilon(\vec{r})$ is the dielectric function. Suppose the dielectric function is periodic and a monochromatic light is considered, then from Bloch's theorem

$$|H\rangle = e^{i(\vec{k}\cdot\vec{r}-\omega t)}|H_{\vec{k}}\rangle \tag{116}$$

where ω is the frequency, $\vec{k}$ is the Bloch wavevector, and $|H_{\vec{k}}\rangle$ is a periodic function. Then Eq. 115 changes to

$$\hat{A}_{\vec{k}}|H_{\vec{k}}\rangle = (\nabla + i\vec{k}) \times \frac{1}{\varepsilon(\vec{r})}(\nabla + i\vec{k}) \times |H_{\vec{k}}\rangle = \frac{\omega^2}{c^2}|H_{\vec{k}}\rangle \tag{117}$$

where $\hat{A}_{\vec{k}}$ is a Hermite operator. The function $|H_{\vec{k}}\rangle$ can be expanded in some truncated basis

$$|H_{\vec{k}}\rangle \cong \sum_{m=1}^{N} h_m|b_m\rangle \tag{118}$$

As the number N goes to infinity, the expression is the exact solution. Then Eq. 117 changes to

$$Ah = \frac{\omega^2}{c^2}Bh \tag{119}$$

where h is the column vector of the coefficients h_m, A and B are $N \times N$ matrices with $A_{mn} = \langle b_m|\hat{A}_{\vec{k}}|b_n\rangle$ and $B_{mn} = \langle b_m|b_n\rangle$. Because only the dispersion relation of several lowest bands are required and the number of the required bands are much smaller than N, the software uses much less time to solve the required dispersion with iterative method, rather than solve the dispersions of all N bands from Eq. 119. Now, the only challenging problem is how to choose a compact, accurate basis with lowest number N so that it is possible to compute Ah and Bh quickly and assure the transverse of magnetic field.

5.2.2. *EMPLab^{TM}*

EMPLab$^{\mathrm{TM}}$ is a general-purpose commercial software developed by EM Photonics, Inc. It uses finite-difference time-domain(FDTD) method to simulate the propagation of electromagnetic wave. In FDTD, Maxwell's equations are discretized in both time- and space-domain. The most widely used discretizing method was proposed by Yee in 1966[118]. In Yee's method, every discretized node has electric and magnetic field components in all three

directions so that each electric field component is surrounded by four magnetic field components and each magnetic field component is also surrounded by four electric field components. The boundary conditions at the interface of two materials are satisfied naturally. The divergences of both electric and magnetic fields are zero implicitly in the absence of source. The electric field has half-step difference in time scale from the magnetic field. At each half time-step, only electric or magnetic field components are updated. The central differences of space and time have the second-order accuracy[119].

The software uses perfect-matched-layer(PML) absorbing boundary condition of the computation zone that was introduced by J.-P. Berenger in 1984[120]. PML is used to minimize the reflection of light with any direction, polarization, and frequency that incidents on the boundary layer.

FDTD method is accurate, rigorous and easy to implement. It can handle all the interested frequencies in one simulation. The grid size has to be reduced if more accurate result is required. As the grid size is reduced, then the time step is also reduced. Finally, the required time and space increases rapidly.

We designed the photonic crystal slab structure with MPB in frequency domain first, then verify the design with EMPLab$^{\mathrm{TM}}$ in time domain.

5.3. Refractive Index Measurement of SAGC by Ellipsometer

Because the refractive index of SAGC is not found in literature, we used variable angle spectroscopic ellipsometry(VASE) to measure it. VASE is a very accurate method to measure refractive index of materials. As light is reflected from a surface, s- and p-polarizations change differently from Fresnel formulas which Fresnel got in 1823[121].

$$
\begin{aligned}
r_s &= \left(\frac{E_r}{E_i}\right)_s = \frac{n_i\cos(\theta_i) - n_t\cos(\theta_t)}{n_i\cos(\theta_i) + n_t\cos(\theta_t)} \\
r_p &= \left(\frac{E_r}{E_i}\right)_p = \frac{n_t\cos(\theta_i) - n_i\cos(\theta_t)}{n_t\cos(\theta_i) + n_i\cos(\theta_t)}
\end{aligned}
\tag{120}
$$

where r_s and r_p are the reflection coefficient of s- and p-polarization, respectively. E_r and E_i are electric field of the reflected and incident light, respectively. n_i and n_t are the refractive

index of medium that incident and refracted light travel in. θ_i and θ_t are the incident and refracted angle relative to the normal of the two medium interface. From Snell's Law

$$n_i \sin(\theta_i) = n_t \sin(\theta_t) \tag{121}$$

If

$$\theta_i + \theta_t = 90^o \tag{122}$$

Then Eq. 121 changes to

$$n_i \cos(\theta_t) = n_t \cos(\theta_i) \tag{123}$$

If we put the above equation into Eq. 120 for p-polarization, we can see that $r_p = 0$. Under the condition of Eq. 122, the incident angle $\theta_B = \theta_i$ is

$$\theta_B = \arctan\left(\frac{n_t}{n_i}\right) \tag{124}$$

So, the reflection of p-polarization light just vanishes at the incident angle θ_B. This angle is called Brewster's angle.

We can define

$$\rho = \frac{r_p}{r_s} = \tan(\Psi) e^{i\Delta} \tag{125}$$

where r_p is the complex reflection coefficient of p-polarization light and r_s is the complex reflection coefficient of s-polarization. $\tan(\Psi)$ is the amplitude ratio of p- to s-polarization of reflection coefficient. Δ is the phase change. Ellipsometry results can be very accurate because it measures the relative change of p- and s-polarization light, rather than the absolute value. This theory is used for reflection mode of ellipsometer and there are ellipsometers that depend on transmission model. For thin films, ellipsometer can get the refractive index and the thickness simultaneously by changing the incident angle. When the incident angle is close to Brewster's angle, the reflection is weak for p-polarization and strong for s-polarization. The change of amplitude and phase is large. So the variable angle spectroscopic ellipsometry takes the measurement at several different incident angles, which are around Brewster's angle. Then the measured data of Ψ and Δ are fitted with models depending on the sample structure to get refractive index and probably thin film thickness. To measure the refractive

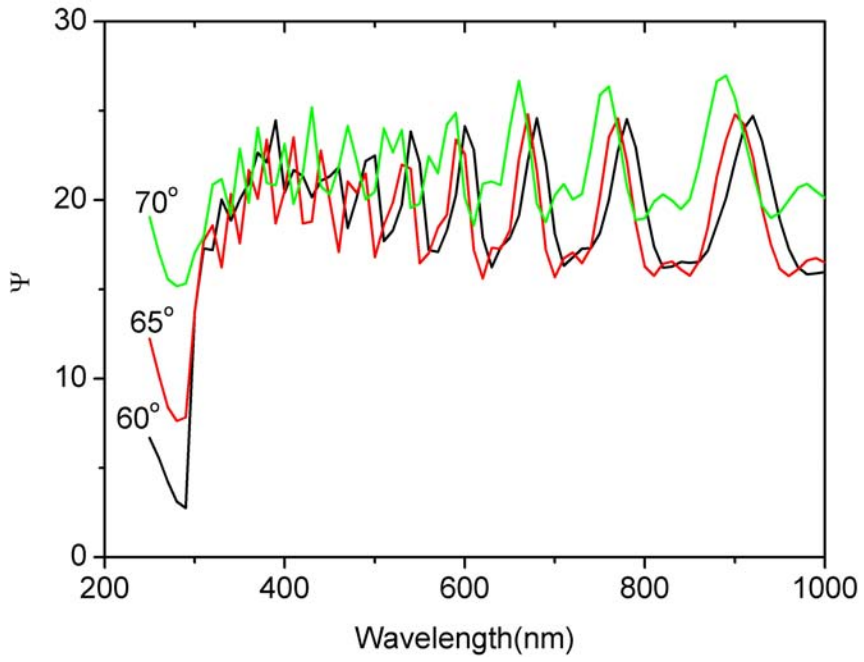

(a)

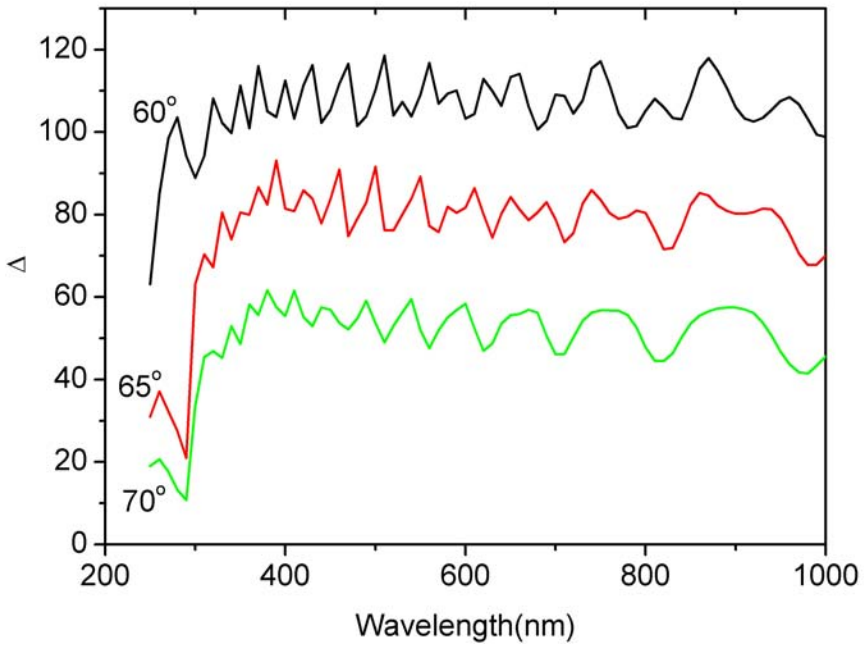

(b)

FIGURE 5.1. (a)Ψ and (b)Δ curves measured by VASE for SAGC thin films on GaN substrate at the incident angles of 60^o, 65^o, and 70^o.

index of SAGC, we deposit deoxyguanosine solution, which is described in Chap. 3, on GaN substrate. Then a thin film is formed. Then the samples were measured with VASE at incident angles of 60^o, 65^o, and 70^o. The Ψ and Δ were fitted with Cauchy relation for refractive index. The refractive index of SAGC was found to be about 1.19 at around $400nm$.

5.4. Modeling of Photonic Crystal

5.4.1. *Design of Photonic Crystal with Software MPB*

The substrate of photonic crystal is a free-standing GaN slab and air is above and beneath the slab, as shown in Fig. 1.1(b). There are hole arrays in the slab to form photonic crystals. The PC-slab can also be considered as periodic in the direction perpendicular to the slab if the slab is sandwiched between two air layers and the air layers are thick enough[33]. So the guided modes in neighboring slab don't interfere. The guided modes can be separated to TE- and TM-like modes because the slab is mirror symmetric about the center plane[33]. We only design the triangular structure because triangular has larger bandgap in TE-like mode. The refractive index of GaN is about 2.53 around 400nm[122]. The bandgap is small because the refractive index contrast is small between SAGC/air and GaN.

Because the calculation of band structure is much slower in 3-dimension than that in 2-dimension, first we find the hole radius in 2-dimension so that the bandgap is large. From Fig. 5.2, we can see that the maximum gap size reaches when the hole radius is about $0.4a$, where a is the lattice constant. Here we use unit based on lattice constant because Maxwell's equations are scale-invariant. After the infiltrating deoxyguanosine inside holes, the bandgap reduces because of the refractive index change. Because the bandgap of PC-slab depends on the thickness of the slab[33], we are trying to find the trend of bandgap changing with slab thickness, h, at certain hole radius, r, and concentrate around the regime with hole radius $r = 0.4a$.

5.4.1.1. *Photonic Crystal Slab with $r = 0.4a$.* From the Fig. 5.3, we can see that the lowest two bands of SAGC/GaN has lower energy than that of air/GaN with the same lattice parameters. The difference between the conduction bands under two conditions is even larger

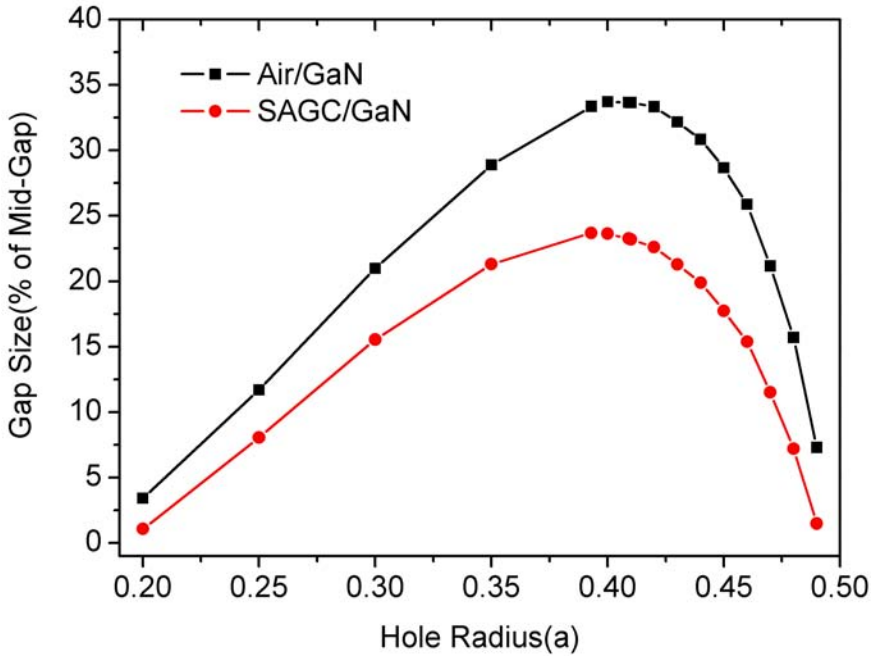

FIGURE 5.2. For air/SAGC and GaN photonic crystal, the gap size of 2D triangular lattice versus hole radius.

compared with the difference of valence bands. The bandgap size of SAGC/GaN is smaller because of the lower refractive index contrast. The bandgap size under two situations has maximum values, but at different slab thickness. The maximum bandgap is at $h = 0.8a$ and $h = 0.7a$ for air/GaN and SAGC/GaN, respectively. The bandgap size increases slowly with the increasing of slab thickness, then reduces rapidly after the maximum. Finally, the bandgap disappears. The trend of bandgap changing just likes what was discussed by Johnson, et al.[33]. If the slab thickness is too large, the energy difference between two neighboring bands is too small and probably can not be differentiated. New nodal plane will be formed in vertical direction with very little energy. On the other hand, the mode inside the slab can be weakly guided if the slab thickness is too thin. The slab is only a weak perturbation to the background. So, there exists a optimum thickness with maximum bandgap.

5.4.1.2. *Photonic Crystal Slab with* $r = 0.44a$. Fig. 5.4 shows the band edge of the lowest two bands and the bandgap information changing with slab thickness for the hole

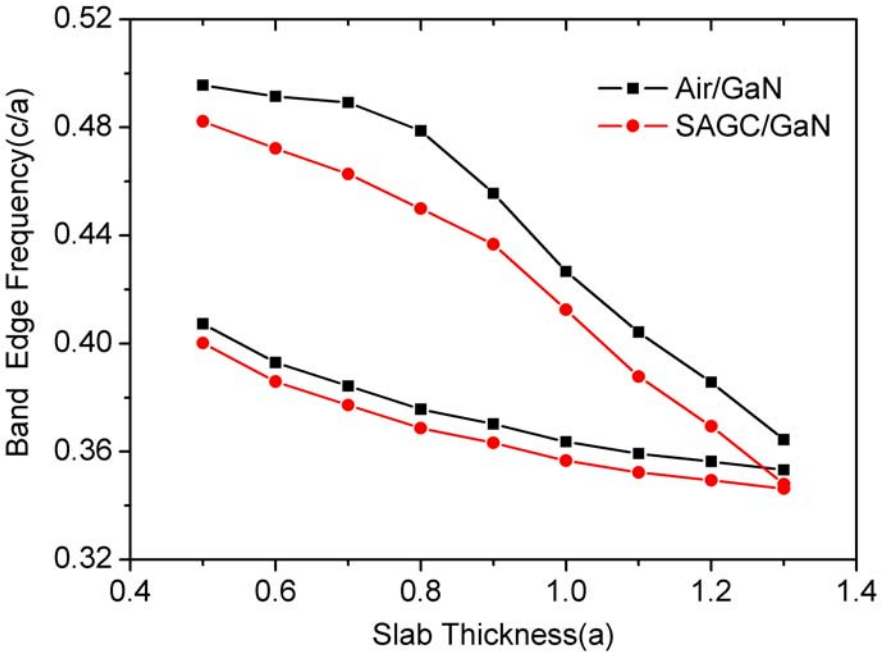

(a)

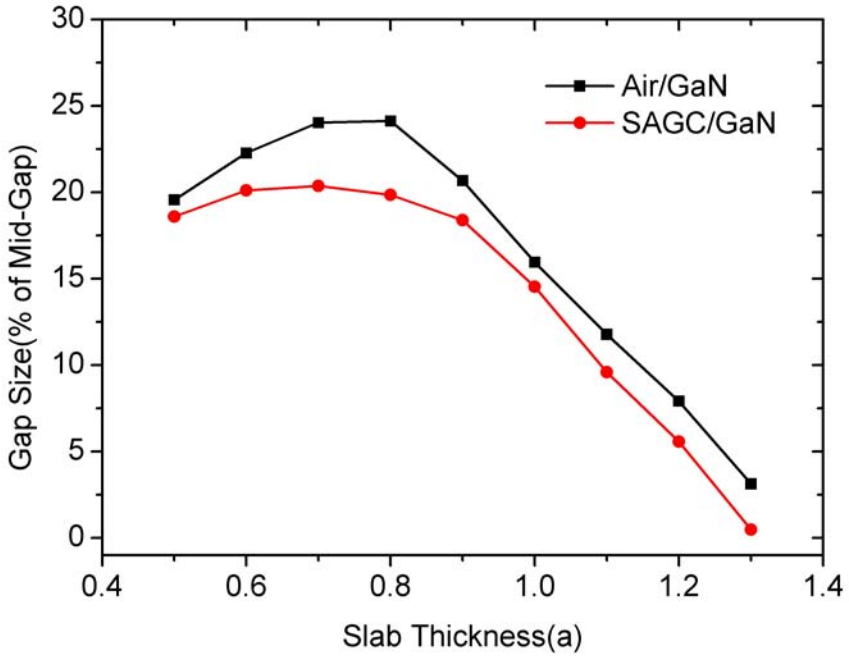

(b)

FIGURE 5.3. For the lowest two bands of photonic crystal slab at hole radius $r = 0.4a$, (a) Band edges and (b) bandgap size change with slab thickness.

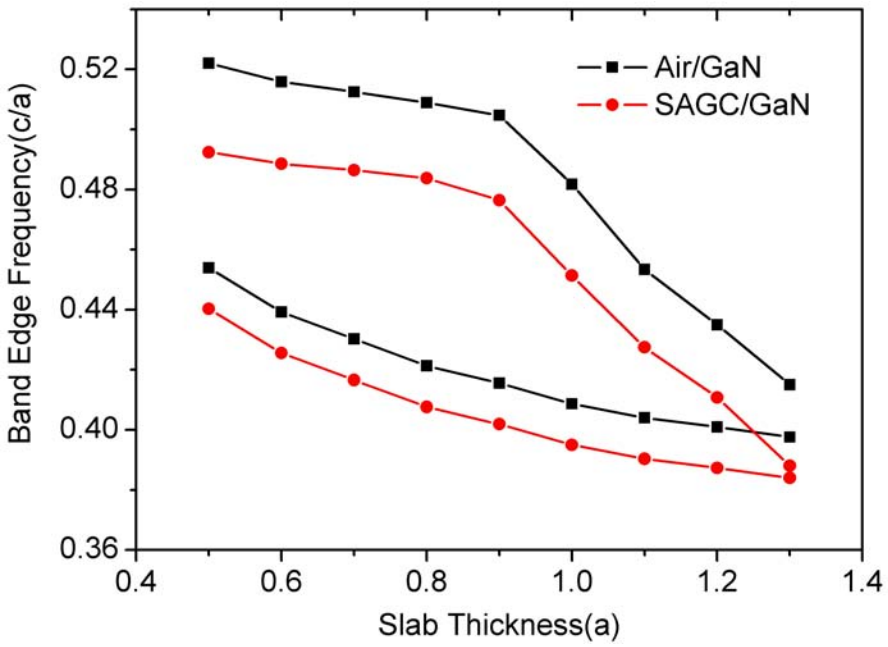

(a)

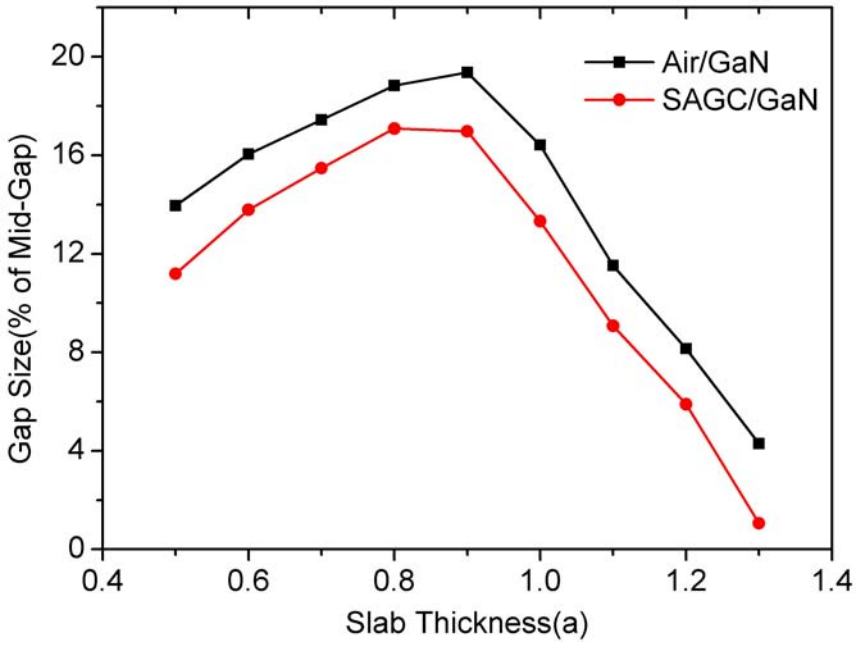

(b)

FIGURE 5.4. For the lowest two bands of photonic crystal slab at hole radius $r = 0.44a$, (a) Band edges and (b) Band gap size change with slab thickness.

radius $r = 0.44a$. The curves show the similar characteristics to that of the structure with $r = 0.4a$. But the differences of conduction and valence bands between air/GaN and SAGC/GaN are larger than that of the structure with $r = 0.4a$. The band edges are higher and the bandgap is smaller when $r = 0.44a$. The bandgaps reach the maximum values at $h = 0.9a$ and $h = 0.8a$ for air/GaN and SAGC/GaN systems, respectively.

5.4.1.3. *Photonic Crystal Slab with* $r = 0.35a$. Fig. 5.5shows the band edge of the two lowest bands and the bandgap change with slab thickness for the hole radius $r = 0.35a$. The band edges have the similar trend to the other two hole radii and the differences of the conduction and the valence bands between air/GaN and SAGC/GaN PC slab are smaller than that of the structure for $r = 0.4a$ and $r = 0.44a$. But the band edges are at lower energy. The bandgaps are small and reach the maximum value at $h = 0.7a$ and $h = 0.6a$ for air/GaN and SAGC/GaN PC slab, respectively.

5.4.2. *Verification of the Photonic Crystal Designs by EMPLab*^{TM}

According to the above analysis, the structures in the Tab. 5.1 are simulated by the software EMPLab$^{\mathrm{TM}}$. The center of the bandgap is at $3.1eV(400nm)$, in the blue-UV region. Because electromagnetic modes in band gap can not exist in photonic crystal, transmission

TABLE 5.1. Lattice Parameters of the Photonic Crystal Slab

r/a	h/a	a(nm)	r(nm)	h(nm)	AG VB(eV)	AG CB(eV)	SG VB(eV)	SG CB(eV)
0.40	0.7	175	70	122	2.73	3.47	2.68	3.28
0.44	0.9	191	84	172	2.69	3.51	2.60	3.14

simulation is used to get the bandgap. In the simulation, light source is a modulated Gaussian pulse that does not have direct current component. The frequency spectrum is a Gaussian peak with center shifted from frequency zero. The perfect-matched-layer absorbing boundary has eight layers.

Figs. 5.6 and 5.7 shows the simulation results. The left part of each figure is the band diagram that is solved by the software MPB. The black curve is edge of light cone. In light

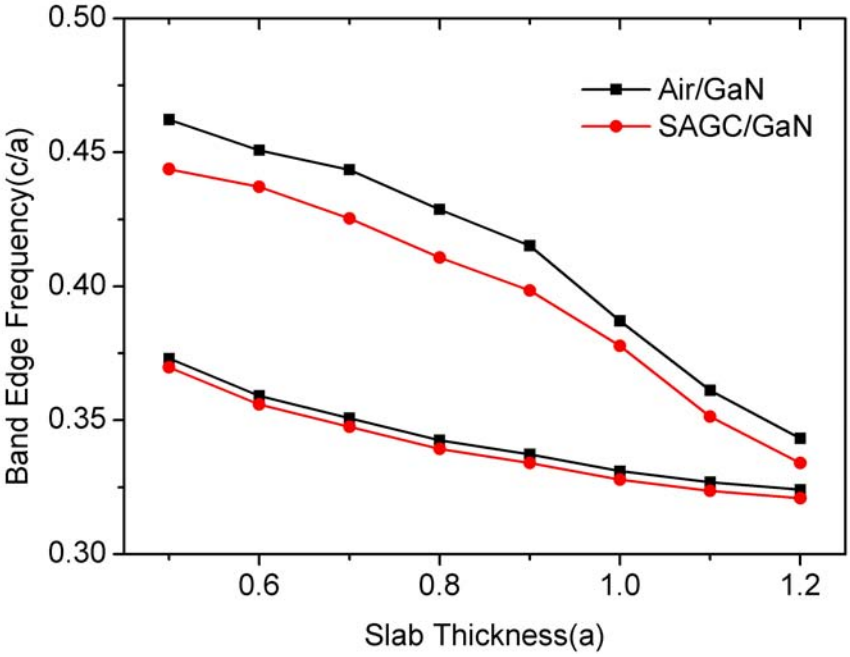

(a)

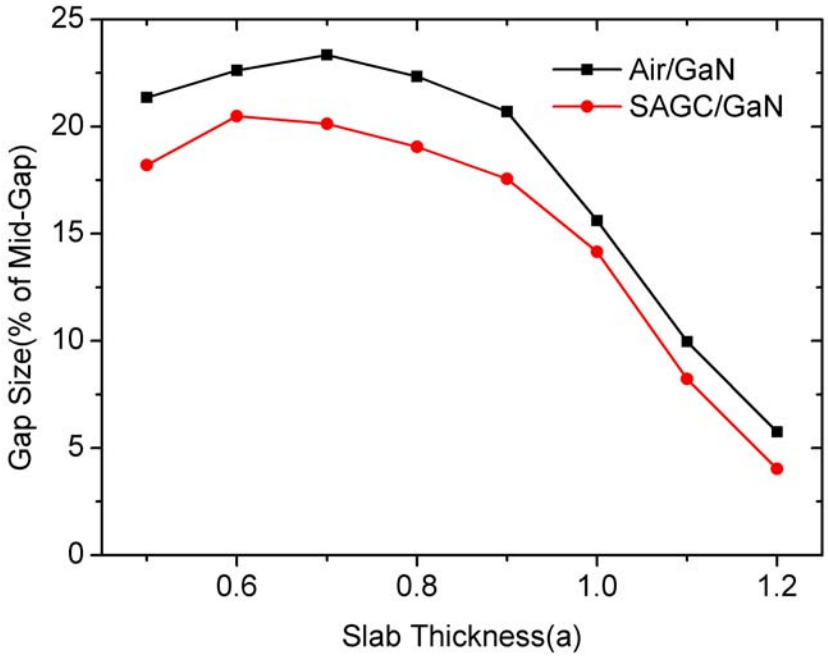

(b)

FIGURE 5.5. For the lowest two bands of photonic crystal slab at hole radius $r = 0.35a$, (a) Band edges and (b) Band gap size change with slab thickness.

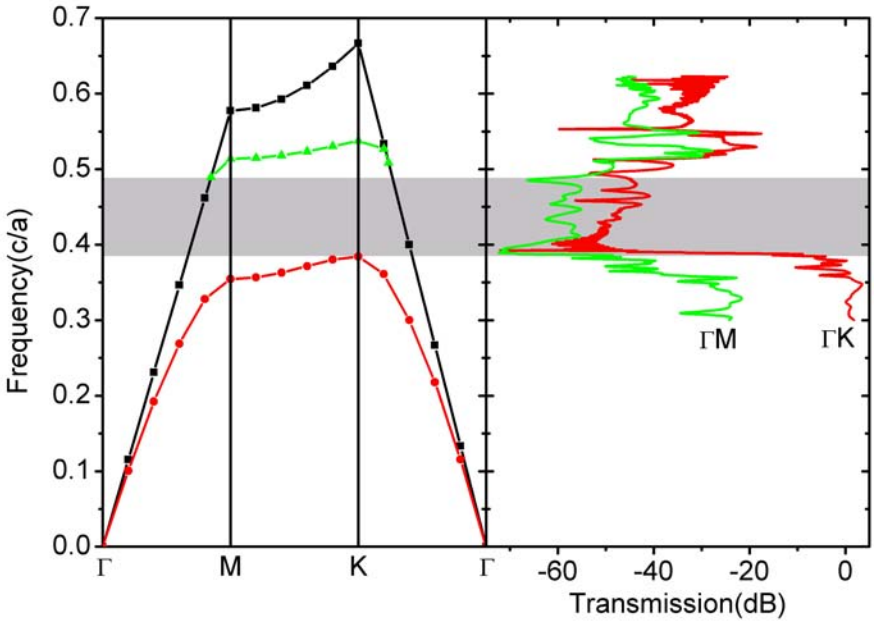

(a)

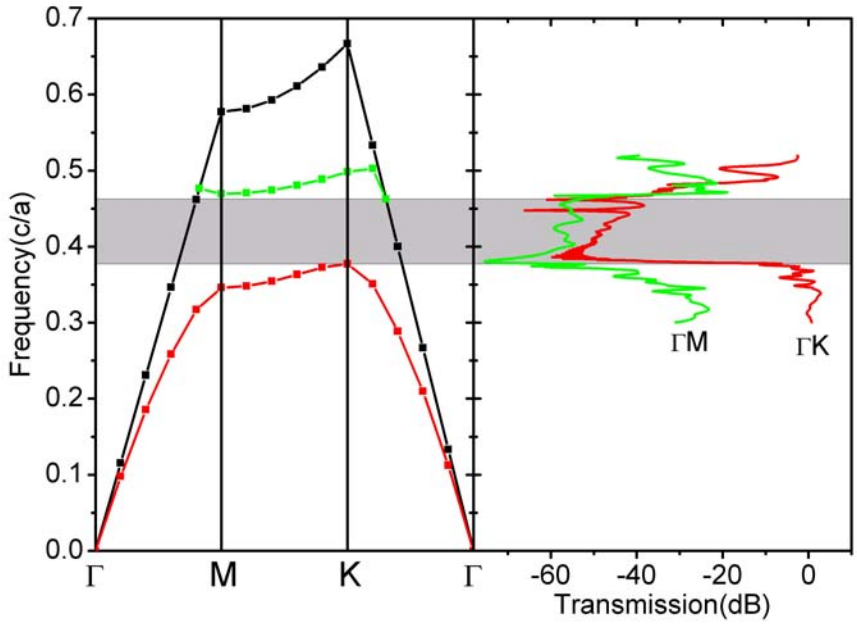

(b)

FIGURE 5.6. Simulation results of (a) air/GaN PC with $r = 0.4a$ and $h = 0.7a$ and (b) SAGC/GaN PC with $r = 0.40a$ and $h = 0.7a$. In each figure, the left part is the band diagram and the right part is the transmission result got by EMPLab^{TM} in ΓK and ΓM direction. The light gray strip is the forbidden band of the structure.

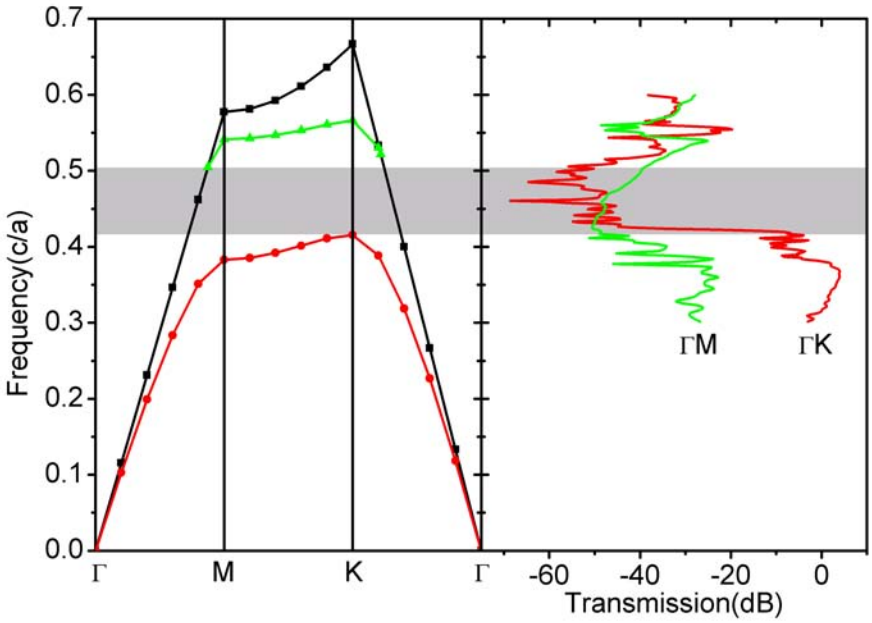

(a)

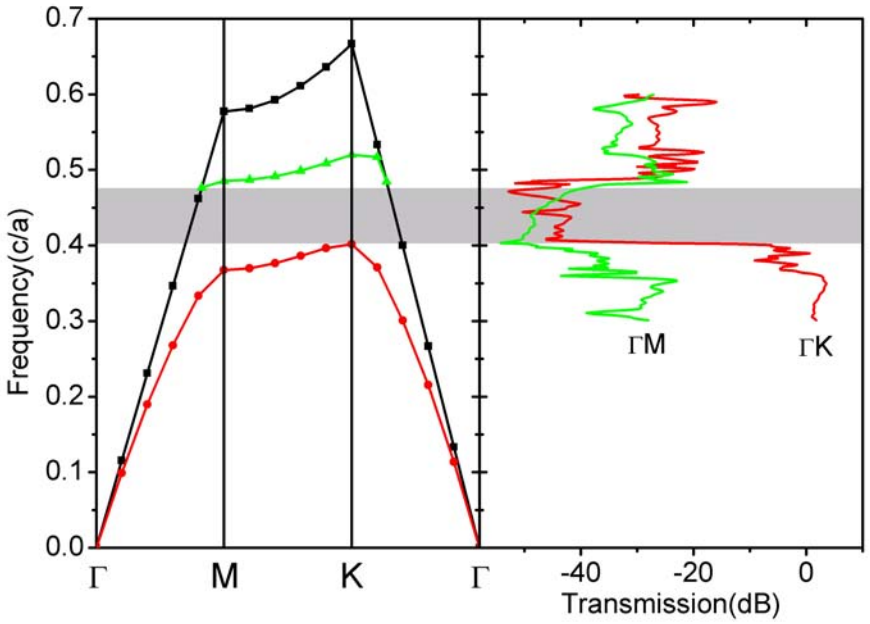

(b)

FIGURE 5.7. Simulation results of (a) air/GaN PC with $r = 0.44a$ and $h = 0.9a$ and (b) SAGC/GaN PC with $r = 0.44a$ and $h = 0.9a$. In each figure, the left part is the band diagram and the right part is the transmission result got by EMPLab^{TM} in ΓK and ΓM direction. The light gray strip is the forbidden band of the structure.

cone, electromagnetic mode can exist in both air and PC-slab. So the light that travels inside PC-slab can leaks into air and the transmission gets lower. The right part of the figures is the transmission spectrum which is got from the simulation results by the software EMPLab^{TM}. The transmission figures are rotated so that it can align with the band diagrams for easy comparing. We simulated two light propagation directions, ΓM and ΓK, as shown in the figures. The light gray strip in the figures shows the bandgap of the structure. The valence band edge in band diagram matches with the drop of transmission. At the conduction band edge, the transmission changes relative slow and has small discrepancy probably due to the leakage of light from PC-slab to air. The transmission spectrum shows that the bandgap shrinks as deoxyguanosine molecules self-assemble inside holes. And the energy of the valence band edge is also decreased, just as shown by MPB.

5.5. Discussion

The hybrid periodical structures based on SAGC and GaN have photonic bandgaps. The size and the position of the bandgap can be tuned by tuning lattice parameters. It is possible to tune the optical coupling between light source with guanosine molecules through the hybrid photonic crystal.

CHAPTER 6

CONCLUSION

In this work, we studied the hybrid organic-inorganic system based on self-assembled deoxyguanosine structure and wide-bandgap semiconductor GaN. Guanosine is one of the four bases of DNA which plays very important role in life. So it is crucial to study the characteristics of guanosine. Deoxyguanosine has the lowest oxidation energy, which favors carrier transport. It also has high dipole moment. Under different environments, deoxyguanosine show resistance, semiconductor or insulator characteristics. Gallium nitride and its alloys are widely used for light emitting devices in green to UV region. Because of noncentrosymmetric wurtzite structure, GaN has strong intrinsic polarization. GaN surface can have positive or negative polarity depending on whether the surface is Ga- or N-terminated.

We studied the self-assembled deoxyguanosine structure in confined space between two electrodes. The current-voltage characteristics can be explained very well with the theory of metal-semiconductor-metal structure. The I-V curves also show strong rectification effect, which can be explained by the intrinsic polarization along the axis of self-assembled ribbon-like structure of deoxyguanosine. Compared with SiO_2 substrate, passivated GaN substrate influences the properties of SAGC. So SAGC has semiconductor properties within the confined space up to 458nm. When the gap distance between two electrodes gets up to 484nm, the structure with deoxyguanosine shows resistance characteristics. The photocurrent measurements show that the bandgap of SAGC is about $3.3 - 3.4eV$ and affected by substrate properties. The MSM structure based on SAGC can be used as photodetector in UV region.

In the last part, we show that the periodic structure based on GaN and SAGC can have photonic bandgaps. The bandgap size and the band edges can be tuned by tuning lattice parameters. Light propagation and emission can be tuned by photonic crystals. So

the hybrid photonic crystal can be potentially used to detect deoxyguanosine molecules. If deoxyguanosine molecules are used as functional linker to other biomolecules which usually absorb or emit light in blue to UV region, the hybrid photonic crystal can also be used to tune the coupling of light source to deoxyguanosine molecules, then to other biomolecules.

As shown in Chap. 3, the MSM structure with SAGC on passivated GaN substrate has very large dynamic resistance. The current fluctuation in the region from near reach-through voltage and up is possibly caused by the large dynamic resistance. It also causes the low current flow through the structure. In the future, we need to find a fabrication method or modified deoxyguanosine synthesis protocol to reduce the dynamic resistance or even the capacitance. Then the time constant can be reduced and the structure can have very fast response. Meanwhile, the sensitivity can also be improved.

In the future, the hybrid photonic crystal based on GaN and SAGC need to be fabricated and studied with experiments to verify the design.

BIBLIOGRAPHY

[1] Gordon E. Moore, Cramming More Components onto Integrated Circuits, Electronics 38 (1965), no. 8, 114–116.

[2] Alongkarn Chutinan and Sajeev John, Light Localization for Broadband Integrated Optics in Three Dimensions, Phys. Rev. B 72 (2005), no. 16, 161316(R).

[3] Paul S. Peercy, The Drive to Miniaturization, Nature 406 (2000), no. 6799, 1023–1026.

[4] Angus I. Kingon, Jon-Paul Maria, and S. K. Streiffer, Alternative Dielectrics to Silicon Dioxide for Memory and Logic Devices, Nature 406 (2000), no. 6799, 1032–1038.

[5] D. B. Mitzi, K. Chondroudis, and C. R. Kagan, Organic-Inorganic Electronics, IBM journal of research and development 45 (2001), no. 1, 29.

[6] David B. Mitzi, *Synthesis, structure, and properties of organic-inorganic perovskites and related materials*, Progress in Inorganic Chemistry (Kenneth D. Karlin, ed.), vol. 58, John Wiley & Sons, Inc, 1999, pp. 1–121.

[7] Akhlesh Lakhtakia and Tom G. Mackay, Meet the Metamaterials, Optics & Photonics News 18 (2007), no. 1, 32 – 39.

[8] Erez Braun, Yoav Eichen, Uri Sivan, and Gdalyahu Ben-Yoseph, DNA-Templated Assembly and Electrode Attachment of a Conducting Silver Wire, Nature 391 (1998), no. 6669, 775–778.

[9] Ali Javey, Hyoungsub Kim, Markus Brink, Qian Wang, Ant Ural, Jing Guo, Paul McIntyre, Paul McEuen, Mark Lundstrom, and Hongjie Dai, High-κ Dielectrics for Advanced Carbon-Nanotube Transistors and Logic Gates, Nat. Mater. 1 (2002), no. 4, 241–246.

[10] Kinneret Keren, Rotern S. Berman, Evgeny Buchstab, Uri Sivan, and Erez Braun, DNA-Templated Carbon Nanotube Field-Effect Transistor, Science 302 (2003), no. 5649, 1380–1382.

[11] Giuseppe Maruccio, Paolo Visconti, Valentina Arima, Stefano D'Amico, Adriana Biasco, Eliana D'Amone, Roberto Cingolani, Ross Rinaldi, Stefano Masiero, Tatiana Giorgi, and Giovanni Gottarelli, Field Effect Transistor Based on a Modified DNA Base, Nano Lett. 3 (2003), no. 4, 479 –483.

[12] Sander J. Tans, Alwin R. M. Verschueren, and Cees Dekker, Room-Temperature Transistor Based on a Single Carbon Nanotube, Nature 393 (1998), no. 6680, 49–52.

[13] P. D. Dapkus and J. D. O'Brien, *Meso- and nanophotonic devices for integrated photonic circuits*, 61st Device Research Conference, IEEE, June 2003, p. 121.

[14] Anatoly V. Zayats and Igor I. Smolyaninov, Near-Field Photonics: Surface Plasmon Polaritons and Localized Surface Plasmons, J. Opt. A: Pure Appl. Opt. 5 (2003), no. 4, S16–S50.

[15] Shigefusa F. Chichibu, Akira Uedono, Takeyoshi Onuma, Benjamin A. Haskell, Arpan Chakraborty, Takahiro Koyama, Paul T. Fini, Stacia Keller, Steven P. Denbaars, James S. Speck, Umesh K. Mishra, Shuji Nakamura, Shigeo Yamaguchi, Satoshi Kamiyama, Hiroshi Amano, Isamu Akasaki, Jung Han, and Takayuki Sota, Origin of Defect-Insensitive Emission Probability in In-Containing (Al,In,Ga)N Alloy Semiconductors, Nat. Mater. 5 (2006), no. 10, 810.

[16] H. X. Jiang and J. Y. Lin, III-Nitride Quantum Devices - Microphotonics, Crit. Rev. Solid State Mater. Sci. 28 (2003), no. 2, 131 –183.

[17] S. N. Mohammad, A. A. Salvador, and H. Morkoç, Emerging Gallium Nitride Based Devices, Proceedings of the IEEE 83 (1995), no. 10, 1306–1355.

[18] M. Razeghi and A. Rogalski, Semiconductor Ultraviolet Detectors, J. Appl. Phys. 79 (1996), no. 10, 7433–7473.

[19] Manijeh Razeghi, Alireza Yasan, Ryan McClintock, Kathryn Mayes, Derek Shiell, Shaban Ramezani Darvish, and Patrick Kung, Review of III-Nitride Optoelectronic Materials for Light Emission and Detection, Phys. Status Solidi C 1 (2004), no. S2, S141 – S148.

[20] Andrzej Jeleński, *Gallium nitride-new material for microwave and optoelectronics*, MIKON '98., 12th International Conference on Microwaves and Radar (Krakow), vol. 4, IEEE, May 1998, pp. 147 – 158.

[21] G. Y. Xu, A. Salvador, W. Kim, Z. Fan, C. Lu, H. Tang, H. Morkoç, G. Smith, M. Estes, B. Goldenberg, W. Yang, and S. Krishnankutty, High Speed, Low Noise Ultraviolet Photodetectors Based on GaN p-i-n and AlGaN(p)-GaN(i)-GaN(n) Structures, Appl. Phys. Lett. 71 (1997), no. 15, 2154–2156.

[22] Eli Yablonovitch, Inhibited Spontaneous Emission in Solid-State Physics and Electronics, Phys. Rev. Lett. 58 (1987), no. 20, 2059 – 2062.

[23] Sajeev John, Strong Localization of Photons in Certain Disordered Dielectric Superlattices, Phys. Rev. Lett. 58 (1987), no. 23, 2486 – 2489.

[24] J. C. Knight, J. Broeng, T. A. Birks, and P. St. J. Russell, Photonic Band Gap Guidance in Optical Fibers, Science 282 (1998), no. 5393, 1476 – 1478.

[25] Edmond Chow, S. Y. Lin, J. R. Wendt, S. G. Johnson, and J. D. Joannopoulos, Quantitative Analysis of Bending Efficiency in Photonic-Crystal Waveguide Bends at $\lambda = 1.55\mu M$ Wavelengths, Optics Letters 26 (2001), no. 5, 286–288.

[26] R. F. Cregan, B. J. Mangan, J. C. Knight, T. A. Birks, P. St. J. Russell, P. J. Roberts, and D. C. Allan, Single-Mode Photonic Band Gap Guidance of Light in Air, Science 285 (1999), no. 5433, 1537 – 1539.

[27] J. C. Knight, T. A. Birks, P. St. J. Russell, and D. M. Atkin, All-Silica Single-Mode Optical Fiber with Photonic Crystal Cladding, Optics Letters 21 (1996), no. 19, 1547–1549.

[28] Charlene M. Smith, Natesan Venkataraman, Michael T. Gallagher, Dirk Mller, James A. West, Nicholas F. Borrelli, Douglas C. Allan, and Karl W. Koch, Low-Loss Hollow-Core Silica/Air Photonic Bandgap Fibre, Nature 424 (2003), no. 6949, 657–659.

[29] Burak Temelkuran, Shandon D. Hart, Gilles Benoit, John D. Joannopoulos, and Yoel Fink, Wavelength-Scalable Hollow Optical Fibres with Large Photonic Bandgaps for CO_2 Laser Transmission, Nature 420 (2002), no. 6916, 650–653.

[30] M. R. Watts, S. G. Johnson, H. A. Haus, and J. D. Joannopoulos, Electromagnetic Cavity with Arbitrary Q and Small Modal Volume without a Complete Photonic Bandgap, Optics Letters 27 (2002), no. 20, 1785–1787.

[31] John D. Joannopoulos, Robert D. Meade, and Joshua N. Winn, *Photonic crystal: Molding the flow of light*, Princeton University Press, July 1995.

[32] C. C. Cheng, V. Arbet-Engels, A. Scherer, and E. Yablonovitch, Nanofabricated Three Dimensional Photonic Crystals Operating at Optical Wavelengths, Phys. Scr. T68 (1996), 17–20.

[33] Steven G. Johnson, Shanhui Fan, Pierre R. Villeneuve, J. D. Joannopoulos, and L. A. Kolodziejski, Guided Modes in Photonic Crystal Slabs, Phys. Rev. B 60 (1999), no. 8, 5751 – 5758.

[34] Shuji Nakamura, Stephen Pearton, and Gerhard Fasol, *The blue laser diode: The complete story*, Springer, 2000.

[35] Shuji Nakamura and Shigefusa F. Chichibu, *Introduction to nitride semiconductor blue lasers and light emitting diodes*, Taylor & Francis, 2000.

[36] O. Ambacher, Growth and Applications of Group III-Nitrides, J. Phys. D: Appl. Phys. 31 (1998), no. 20, 2653–2710.

[37] Daming Huang, Michael A. Reshchikov, and Hadis Morkoç, Growth, Structures, and Optical Properties of III-Nitride Quantum Dots, International Journal of High Speed Electronics and Systems 12 (2002), no. 1, 79–110.

[38] S. J. Rosner, E. C. Carr, M. J. Ludowise, G. Girolami, and H. I. Erikson, Correlation of Cathodoluminescence Inhomogeneity with Microstructural Defects in Epitaxial GaN Grown by Metalorganic Chemical-Vapor Deposition, Appl. Phys. Lett. 70 (1997), no. 4, 420–422.

[39] Arieh Aviram and Mark A. Ratner, Molecular Rectifiers, Chem. Phys. Lett. 29 (1974), no. 2, 277–283.

[40] R. G. Endres, D. L. Cox, and R. R. P. Singh, Colloquium: The Quest for High-Conductance DNA, Rev. Mod. Phys. 76 (2004), no. 1, 195–214.

[41] A. S. Martin, J. R. Sambles, and G. J. Ashwell, Molecular Rectifier, Phys. Rev. Lett. 70 (1993), no. 2, 218 – 221.

[42] E. Helgren, A. Omerzu, G. Grüner, R. Podgornik D. Mihailovic, and H. Grimm, *Electrons on the double helix: Optical experiments on native dna*, eprint, November 2001, arXiv:cond-mat/0111299.

[43] D. D. Eley and D. I. Spivey, Semiconductivity of Organic Substances. Part 9.Nucleic Acid in the Dry State, Transactions of the Faraday Society 58 (1962), 411 – 415.

[44] P. J. de Pablo, F. Moreno-Herrero, J. Colchero, J. Gómez Herrero, P. Herrero, A. M. Baró, Pablo Ordejón, José M. Soler, and Emilio Artacho, Absence of DC-Conductivity in λ-DNA, Phys. Rev. Lett. 85 (2000), no. 23, 4992 – 4995.

[45] A. J. Storm, J. van Noort, S. de Vries, and C. Dekker, Insulating Behavior for DNA Molecules Between Nanoelectrodes at the 100 nm Length Scale, Appl. Phys. Lett. 79 (2001), no. 23, 3881–3883.

[46] Y. Zhang, R. H. Austin, J. Kraeft, E. C. Cox, and N. P. Ong, Insulating Behavior of λ-DNA on the Micron Scale, Phys. Rev. Lett. 89 (2002), no. 19, 198102.

[47] Danny Porath, Alexey Bezryadin, Simon de Vries, and Cees Dekker, Direct Measurement of Electrical Transport through DNA Molecules, Nature 403 (2000), no. 6770, 635–638.

[48] Lintao Cai, Hitoshi Tabata, and Tomoji Kawai, Self-Assembled DNA Networks and Their Electrical Conductivity, Appl. Phys. Lett. 77 (2000), no. 19, 3105–3106.

[49] Hans-Werner Fink and Christian Schönenberger, Electrical Conduction through DNA Molecules, Nature 398 (1999), no. 6726, 407–410.

[50] A. Rakitin, P. Aich, C. Papadopoulos, Yu. Kobzar, A. S. Vedeneev, J. S. Lee, and J. M. Xu, Metallic Conduction through Engineered DNA: DNA Nanoelectronic Building Blocks, Phys. Rev. Lett. 86 (2001), no. 16, 3670 – 3673.

[51] P. Tran, B. Alavi, and G. Gruner, Charge Transport along the λ-DNA Double Helix, Phys. Rev. Lett. 85 (2000), no. 7, 1564 – 1567.

[52] K.-H. Yoo, D. H. Ha, J.-O. Lee, J. W. Park, Jinhee Kim, J. J. Kim, H.-Y. Lee, T. Kawai, and Han Yong Choi, Electrical Conduction through Poly(dA)-Poly(dT) and Poly(dG)-Poly(dC) DNA Molecules, Phys. Rev. Lett. 87 (2001), no. 19, 198102.

[53] A. Yu. Kasumov, M. Kociak, S. Guéron, B. Reulet, V. T. Volkov, D. V. Klinov, and H. Bouchiat, Proximity-Induced Superconductivity in DNA, Science 291 (2001), no. 5502, 280 – 282.

[54] Harden M. McConnell, Intramolecular Charge Transfer in Aromatic Free Radicals, J. Chem. Phys. 35 (1961), no. 2, 508–515.

[55] M. Bixon and Joshua Jortner, Energetic Control and Kinetics of Hole Migration in DNA, J. Phys. Chem. B 104 (2000), no. 16, 3906 –3913.

[56] Joshua Jortner, Mordechai Bixon, Thomas Langenbacher, and Maria E. Michel-Beyerle, Charge Transfer and Transport in DNA, Proc. Natl. Acad. Sci. U. S. A. 95 (1998), no. 22, 12759–12765.

[57] M. Bixon and Joshua Jortner, Hole Trapping, Detrapping, and Hopping in DNA, J. Phys. Chem. A 105 (2001), no. 45, 10322 –10328.

[58] Ferdinand C. Grozema, Yuri A. Berlin, and Laurens D. A. Siebbeles, Mechanism of Charge Migration through DNA: Molecular Wire Behavior, Single-Step Tunneling or Hopping?, J. Am. Chem. Soc. 122 (2000), no. 44, 10903 – 10909.

[59] John M. Warman, Matthijs P. de Haas, and Allan Rupprecht, DNA: A Molecular Wire?, Chem. Phys. Lett. 249 (1996), no. 5-6, 319–322.

[60] Francesco Luigi Gervasio, Paolo Carloni, and Michele Parrinello, Electronic Structure of Wet DNA, Phys. Rev. Lett. 89 (2002), no. 10, 108102.

[61] Moshe Faraggi, Federico Broitman, Jeffrey B. Trent, and Michael H. Klapper, One-Electron Oxidation Reactions of Some Purine and Pyrimidine Bases in Aqueous Solutions. Electrochemical and Pulse Radiolysis Studies, J. Phys. Chem. 100 (1996), no. 35, 14751 –14761.

[62] Pavel Hobza and Jiří Šponer, Structure, Energetics, and Dynamics of the Nucleic Acid Base Pairs: Nonempirical Ab Initio Calculations, Chem. Rev. 99 (1999), no. 11, 3247 –3276.

[63] Ross Rinaldi, Emanuela Branca, Roberto Cingolani, Rosa Di Felice, Arrigo Calzolari, Elisa Molinari, Salvatore Masiero, Gianpiero Spada, Giovanni Gottarelli, and Anna Garbesi, Biomolecular Electronic Devices Based on Self-Organized Deoxyguanosine Nanocrystals, Annals of the New York Academy of Sciences 960 (2002), no. 1, 184192.

[64] Giovanni Gottarelli, Stefano Masiero, Elisabetta Mezzina, Gian Piero Spada, Paolo Mariani, and Maurizio Recanatini, The Self-Assembly of a Lipophilic Deoxyguanosine Derivative and the Formation of a Liquid-Crystalline Phase in Hydrocarbon Solvents, Helv. Chim. Acta 81 (1998), no. 11, 2078–2092.

[65] R. Rinaldi, E. Branca, R. Cingolani, S. Masiero, G. P. Spada, and G. Gottarelli, Photodetectors Fabricated from a Self-Assembly of a Deoxyguanosine Derivative, Appl. Phys. Lett. 78 (2001), no. 22, 3541–3543.

[66] Volker Heine, Theory of Surface States, Phys. Rev. 138 (1965), no. 6A, A1689 – A1696.

[67] E. Louis, F. Yndurain, and F. Flores, Metal-Semiconductor Junction for (110) Surfaces of Zinc-Blende Compounds, Phys. Rev. B 13 (1976), no. 10, 4408 – 4418.

[68] Steven G. Louie and Marvin L. Cohen, Electronic Structure of a Metal-Semiconductor Interface, Phys. Rev. B 13 (1976), no. 6, 2461 – 2469.

[69] Oleg Cojocari and Hans L. Hartnagel, Generalized Model of the Metal/N-GaN Schottky Interface and Improved Performance by Electrochemical Pt Depositionc, J. Vac. Sci. Technol., B 24 (2006), no. 6, 2544–2552.

[70] L. J. Brillson, T. M. Levin, G. H. Jessen, A. P. Young, C. Tu, Y. Naoi, F. A. Ponce, Y. Yang, G. J. Lapeyre, J. D. MacKenzie, and C. R. Abernathy, Defect Formation near GaN Surfaces and Interfaces, Physica B: Condensed Matter 273-274 (1999), 70–74.

[71] Tamotsu Hashizume and Hideki Hasegawa, Effects of Nitrogen Deficiency on Electronic Properties of AlGaN Surfaces Subjected to Thermal and Plasma Processes, Appl. Surf. Sci. 234 (2004), no. 1-4, 387–394.

[72] H. A. Bethe, Theory of the Boundary Layer of Crystal Rectifiers, MIT Radiat. Lab. Rep. 43-12 (1942).

[73] S. M. Sze, *Physics of semiconductor devices*, 2nd ed., John Wiley & Sons, 1981.

[74] C. R. Crowell, The Richardson Constant for Thermionic Emission in Schottky Barrier Diodes, Solid-State Electron. 8 (1965), no. 4, 395–399.

[75] W. Schottky, Halbleitertheorie der Sperrschicht, Naturwissenschaften 26 (1938), 843.

[76] C. R. Crowell and S. M. Sze, Current Transport in Metal-Semiconductor Barriers, Solid-State Electron. 9 (1966), no. 11-12, 1035–1048.

[77] Chung-Whei Kao, C. Lawrence Anderson, and C. R. Crowell, Photoelectron Injection at Metal-Semiconductor Interfaces, Surf. Sci. 95 (1980), no. 1, 321–339.

[78] C. R. Crowell and S. M. Sze, Electron-Optical-Phonon Scattering in the Emitter and Collector Barriers of Semiconductor-Metal-Semiconductor Structures, Solid-State Electron. 8 (1965), no. 12, 979–990.

[79] C. Y. Chang and S. M. Sze, Carrier Transport across Metal-Semiconductor Barriers, Solid-State Electron. 13 (1970), no. 6, 727–740.

[80] C. R. Crowell and S. M. Sze, Quantum-Mechanical Reflection of Electrons at Metal-Semiconductor Barriers: Electron Transport in Semiconductor-Metal-Semiconductor Structures, J. Appl. Phys. 37 (1966), no. 7, 2683–2689.

[81] J. M. Andrews and M. P. Lepselter, Reverse Current-Voltage Characteristics of Metal-Silicide Schottky Diodes, Solid-State Electron. 13 (1970), no. 7, 1011–1023.

[82] C. R. Crowell and M. Beguwala, Recombination Velocity Effects on Current Diffusion and Imref in Schottky Barriers, Solid-State Electron. 14 (1971), no. 11, 1149–1157.

[83] F. A. Padovani and R. Stratton, Field and Thermionic-Field Emission in Schottky Barriers, Solid-State Electron. 9 (1966), no. 7, 695–707.

[84] S. M. Sze, D. J. Coleman, and A. Loya, Current Transport in Metal-Semiconductor-Metal (MSM) Structures, Solid-State Electron. 14 (1971), no. 12, 1209–1218.

[85] Vijayender Bhalla, Ram P. Bajpai, and Lalit M. Bharadwaj, DNA Electronics, EMBO Reports 4 (2003), no. 5, 442.

[86] Paolo Samorí, Silvia Pieraccini, Stefano Masiero, Gian Piero Spada, Giovanni Gottarelli, and Jürgen P. Rabe, Controlling the Self-Assembly of a Deoxiguaninosine on Mica, Colloids and Surfaces B: Biointerfaces 23 (2002), no. 4, 283–288.

[87] Peter Sandvik, Kan Mi, Fatemeh Shahedipour, Ryan McClintock, Alireza Yasan, Patrick Kung, and Manijeh Razeghi, $Al_xGa_{1-x}N$ For Solar-Blind UV Detectors, J. Cryst. Growth 231 (2001), no. 3, 366–370.

[88] R Rinaldi, G Maruccio, A Biasco, V Arima, R Cingolani, T Giorgi, S Masiero, G P Spada, and G Gottarelli, Hybrid Molecular Electronic Devices Based on Modified Deoxyguanosines, Nanotechnology 13 (2002), no. 3, 398–403.

[89] Giovanni Gottarelli, Stefano Masiero, Elisabetta Mezzina, Silvia Pieraccini, Jürgen P. Rabe, Paolo Samorí, and Gian Piero Spada, The Self-Assembly of Lipophilic Guanosine Derivatives in Solution and on Solid Surfaces, Chem.–Eur. J. 6 (2000), no. 17, 3242 – 3248.

[90] C. D. Hodgman and W. R. Veazey, *Handbook of chemistry and physics*, 47th ed., The Chemical Rubber Co., 1966.

[91] Neil W. Ashcroft and N. David Mermin, *Solid state physics*, Harcourt College Physics, 1976.

[92] G. M. Barrow, *Physical chemistry*, 5th ed., McGraw-Hill, 1988.

[93] Hiroshi Sugiyama and Isao Saito, Theoretical Studies of GG-Specific Photocleavage of DNA via Electron Transfer: Significant Lowering of Ionization Potential and 5'-Localization of HOMO of Stacked GG Bases in B-Form DNA, J. Am. Chem. Soc. 118 (1996), no. 30, 7063 – 7068.

[94] Stacey D. Wetmore, Russell J. Boyd, and Leif A. Eriksson, Electron Affinities and Ionization Potentials of Nucleotide Bases, Chem. Phys. Lett. 322 (2000), no. 1-2, 129–135.

[95] Mordechai Bixon and Joshua Jortner, Charge Transport in DNA Via Thermally Induced Hopping, J. Am. Chem. Soc. 123 (2001), no. 50, 12556 – 12567.

[96] F. A. Ponce, D. P. Bour, W. T. Young, M. Saunders, and J. W. Steeds, Determination of Lattice Polarity for Growth of GaN Bulk Single Crystals and Epitaxial Layers, Appl. Phys. Lett. 69 (1996), no. 3, 337–339.

[97] Roberto Cingolani, Ross Rinaldi, Giuseppe Maruccio, and Adriana Biasco, Nanotechnology Approaches to Self-Organized Bio-Molecular Devices, Physica E 13 (2002), no. 2-4, 1229.

[98] E. Monroy, F. Omnès, and F. Calle, Wide-Bandgap Semiconductor Ultraviolet Photodetectors, Semicond. Sci. Technol. 18 (2003), no. 4, R33–R51.

[99] Edmond Chow, S.Y. Lin, S.G. Johnson, P.R. Villeneuve, J.D. Joannopoulos, J.R. Wendt, G.A. Vawter, W. Zubrzycki, H. Hou, and A. Alleman, Three-Dimensional Control of Light in a Two-Dimensional Photonic Crystal Slab, Nature 407 (2000), no. 6807, 983–986.

[100] M. Dinu, R. L. Willett, K. Baldwin, L. N. Pfeiffer, and K. W. West, Waveguide Tapers and Waveguide Bends in AlGaAs-Based Two-Dimensional Photonic Crystals, Appl. Phys. Lett. 83 (2003), no. 22, 4471–4473.

[101] Seunghyun Kim, Gregory P. Nordin, Jingbo Cai, and Jianhua Jiang, Ultracompact High-Efficiency Polarizing Beam Splitter with a Hybrid Photonic Crystal and Conventional Waveguide Structure, Optics Letters 28 (2003), no. 23, 2384–2386.

[102] P.R. Villeneuve, S. Fan, S.G. Johnson, and J.D. Joannopoulos, Three-Dimensional Photon Confinement in Photonic Crystals of Low-Dimensional Periodicity, IEE Proceedings - Optoelectronics 145 (1998), no. 6, 384–390.

[103] M. Arita, S. Ishida, S. Kako, S. Iwamoto, and Y. Arakawa, AlN Air-Bridge Photonic Crystal Nanocavities Demonstrating High Quality Factor, Appl. Phys. Lett. 91 (2007), no. 5, 051106.

[104] Y.-S. Choi, K. Hennessy, R. Sharma, E. Haberer, Y. Gao, S. P. DenBaars, S. Nakamura, E. L. Hu, and C. Meierkk, GaN Blue Photonic Crystal Membrane Nanocavities, Appl. Phys. Lett. 87 (2005), no. 24, 243101.

[105] J. S. Foresi, P. R. Villeneuve, J. Ferrera, E. R. Thoen, G. Steinmeyer, S. Fan, J. D. Joannopoulos, L. C. Kimerling, Henry I. Smith, and E. P. Ippen, Photonic-Bandgap Microcavities in Optical Waveguides, Nature 390 (1997), no. 6656, 143–145.

[106] Chun-Feng Lai, Peichen Yu, Te-Chung Wang, Hao-Chung Kuo, Tien-Chang Lu, Shing-Chung Wang, and Chao-Kuei Lee, Lasing Characteristics of a GaN Photonic Crystal Nanocavity Light Source, Appl. Phys. Lett. 91 (2007), no. 4, 041101.

[107] Cedrik Meier, Kevin Hennessy, Elaine D. Haberer, Rajat Sharma, Yong-Seok Choi, Kelly McGroddy, Stacia Keller, Steven P. DenBaars, Shuji Nakamura, and Evelyn L. Hu, Visible Resonant Modes in GaN-Based Photonic Crystal Membrane Cavities, Appl. Phys. Lett. 88 (2006), no. 3, 031111.

[108] Chia-Hsin Chao, S. L. Chuang, and Tzong-Lin Wu, Theoretical Demonstration of Enhancement of Light Extraction of Flip-Chip GaN Light-Emitting Diodes with Photonic Crystals, Appl. Phys. Lett. 89 (2006), no. 9, 091116.

[109] Dong-Ho Kim, Chi-O Cho, Yeong-Geun Roh, Heonsu Jeon, Yoon Soo Park, Jaehee Cho, Jin Seo Im, Cheolsoo Sone, Yongjo Park, Won Jun Choi, and Q-Han Park, Enhanced Light Extraction from GaN-Based Light-Emitting Diodes with Holographically Generated Two-Dimensional Photonic Crystal Patterns, Appl. Phys. Lett. 87 (2005), no. 20, 203508.

[110] Sang Hoon Kim, Ki-Dong Lee, Ja-Yeon Kim, Min-Ki Kwon, and Seong-Ju Park, Fabrication of Photonic Crystal Structures on Light Emitting Diodes by Nanoimprint Lithography, Nanotechnology 18 (2007), no. 5, 055306c.

[111] T. N. Oder, J. Shakya, J. Y. Lin, and H. X. Jiang, III-Nitride Photonic Crystals, Appl. Phys. Lett. 83 (2003), no. 6, 1231–1233.

[112] A. Neogi, J. Li, P. B. Neogi, A. Sarkar, and H. Morkoç, Self-Assembled Modified Deoxyguanosines Conjugated to GaN Quantum Dots for Biophotonic Applications, Electronics Letters 40 (2004), no. 25, 1605– 1606.

[113] H. Liddar, J. Li, A. Neogi, P. B. Neogi, A. Sarkar, S. Cho, and H. Morkç, Self-Assembled Deoxyguanosine Based Molecular Electronic Device on GaN Substrates, Appl. Phys. Lett. 92 (2008), no. 1, 013309, Accepted.

[114] Sanford A. Asher, Vladimir L. Alexeev, Alexander V. Goponenko, Anjal C. Sharma, Igor K. Lednev, Craig S. Wilcox, and David N. Finegold, Photonic Crystal Carbohydrate Sensors: Low Ionic Strength Sugar Sensing, J. Am. Chem. Soc. 125 (2003), no. 11, 3322 –3329.

[115] Sanford A. Asher, Serban F. Peteu, Chad E. Reese, Ming Lin, and David Finegold, Polymerized Crystalline Colloidal Array Chemical-Sensing Materials for Detection of Lead in Body Fluids, Anal. Bioanal. Chem. 373 (2002), no. 7, 632–638.

[116] Chad E. Reese and Sanford A. Asher, Photonic Crystal Optrode Sensor for Detection of Pb^{2+} in High Ionic Strength Environments, Anal. Chem. 75 (2003), no. 15, 3915 – 3918.

[117] Steven Johnson and John Joannopoulos, Block-Iterative Frequency-Domain Methods for Maxwell's Equations in a Planewave Basis, Opt. Express 8 (2001), no. 3, 173–190.

[118] Kane Yee, Numerical Solution of Inital Boundary Value Problems Involving Maxwell'S Equations in Isotropic Media, IEEE Transactions on Antennas and Propagation 14 (1966), no. 3, 302– 307.

[119] Allen Taflove and Susan C. Hagnes, *Computational electrodynamics: The finite-difference time-domain method*, 2nd ed., Artech House, 2000.

[120] Jean-Pierre Berenger, A Perfectly Matched Layer for the Absorption of Electromagnetic Waves, Journal of Computational Physics 114 (1994), no. 2, 185–200.

[121] Max Born and Emil Wolf, *Principles of optics: Electromagnetic theory of propagation, interference and diffraction of light*, 7th ed., Cambridge University Press, 1999.

[122] G. Yu, G. Wang, H. Ishikawa, M. Umeno, T. Soga, T. Egawa, J. Watanabe, and T. Jimbo, Optical Properties of Wurtzite Structure GaN on Sapphire around Fundamental Absorption Edge (0.78–4.77 eV) by Spectroscopic Ellipsometry and the Optical Transmission Method, Appl. Phys. Lett. 70 (1997), no. 24, 3209–3211.